

THESIS

DEVELOPMENT AND TESTING OF A SOLID CORE FIBER OPTIC DELIVERY
SYSTEM AND ULTRAVIOLET PREIONIZATION FOR LASER IGNITION

Submitted by

Hurley Nicholas Wilvert

Department of Mechanical Engineering

In partial fulfillment of the requirements

For the Degree of Master of Science

Colorado State University

Fort Collins, Colorado

Summer 2012

Master's Committee:

Advisor: Azer Yalin

Anthony Marchese

Jorge Rocca

ABSTRACT

DEVELOPMENT AND TESTING OF A SOLID CORE FIBER OPTIC DELIVERY SYSTEM AND ULTRAVIOLET PREIONIZATION FOR LASER IGNITION

Laser ignition of natural gas engines has shown potential to improve many facets of engine performance including brake thermal efficiency, exhaust emissions, and durability as compared with traditional spark ignition. Laser ignition technology has yet to transition to industry primarily because no system for reliably and safely delivering the laser pulse to the combustion chamber exists. This thesis presents a novel fiber optic delivery approach using solid core multimode step index silica fibers with large cladding diameters (400 μm core, 720 μm cladding). Testing was done on the fibers to determine their response to bending, vibration, high power input, and long duration beam transmission. It was found that in configurations representative of what is required on a real engine, and in the presence of vibration, reliable spark formation could be achieved in pressures as low as 3.4 bar using a specially designed optical spark plug. Comparative tests between the fiber delivered laser ignition system and a traditional J-gap spark plug were performed on a single cylinder Waukesha Cooperative Fuel Research (CFR) engine running on bottled methane. Tests were run at three different Net Mean Effective Pressures (NMEP) of 6, 8, and 12 bar at various air-fuel ratios. Results indicate reliable performance of the fiber and improved engine performance at high NMEP and lean conditions. Thesis research also includes initial studies into the use of dual laser pulses for plasma formation and ignition. In this approach, a first ultraviolet pulse preionizes a

volume of air while a second overlapped pulse adds additional energy. Electron density measurements reveal the ultraviolet beam generates substantial preionization even with no visual breakdown, and Schlieren images are used to study the interaction between the two beams at atmospheric and lower pressures.

TABLE OF CONTENTS

1	Introduction.....	1
1.1	Electrical Spark Ignition.....	3
1.2	Laser Ignition	5
1.2.1	Plasma Formation	7
1.2.2	Ignition.....	10
1.2.3	Potential Benefits	15
1.3	Laser Pulse Delivery	18
1.3.1	Open Path Beam Delivery	18
1.3.2	Single Laser per Engine Cylinder.....	19
1.3.3	Fiber Delivered Diode Pump	21
1.3.4	Fiber Delivered Laser Light.....	21
1.3.5	Hollow Core Fibers.....	22
1.3.6	Solid Core Fibers	24
1.3.7	Photonic Crystal / Photonic Band Gap Fibers	26
1.3.8	Fiber Lasers.....	27
1.4	Problem Statement	28
2	Development of a Solid Core Fiber Delivery System	30
2.1	Fiber Beam Quality Testing.....	30
2.1.1	Fiber Selection	30

2.1.2	M ² Measurement Methods	32
2.1.3	Fiber Test Setup	33
2.1.4	Fiber Beam Quality Results	37
2.2	Fiber Power Testing	38
2.2.1	Long Pulse	38
2.2.2	Stimulated Brillouin Scattering.....	39
2.2.3	Longevity Testing	44
2.3	Vibration Testing.....	47
2.3.1	CW Vibration Tests	47
2.3.2	Pulsed Vibration Tests	50
2.4	Engine Test Preparation	54
2.4.1	Fiber Configuration.....	54
2.4.2	Optical Spark Plug Design.....	54
3	Solid Core Fiber Delivered Laser Ignition Test.....	59
3.1	Experimental Setup	59
3.1.1	Engine	59
3.1.2	Fiber and Laser	61
3.1.3	Test Methodology	63
3.2	Engine Test Results.....	65
3.2.1	Cold Start	65

3.2.2	6 Bar NMEP	66
3.2.3	8 Bar NMEP	70
3.2.4	12 Bar NMEP	74
3.2.5	Lens Damage	78
3.2.6	Discussion	80
4	Laser Plasma Formation Using Preionizing Ultraviolet Pulses	87
4.1	Estimation of Electron Number Density	89
4.1.1	Experimental Setup	89
4.1.2	Results and Discussion	90
4.2	Laser Plasmas Due to Overlapped Pulses	93
4.2.1	Experimental Setup	94
4.2.2	Results and Discussion	96
5	Conclusion	102
	References	109
	Appendix 1 – Vibration Damping with Oil	116
	Appendix 2 – Additional Engine Test Plots	122

LIST OF FIGURES

Figure 1 – Service life of spark plugs and required electrode voltages for two different BMEPs [5].	5
Figure 2 – Experimentally determined breakdown thresholds of argon, nitrogen, and oxygen for laser wavelengths of (a) 1064 nm and (b) 532 nm for various pressures [22].	8
Figure 3 – Minimum pulse and ignition energies for methane at different air-fuel ratios [27]. References in legend are with respect to the cited source in this caption. Points denoted with a “+” symbol are at 3 MPa, all other values are at atmospheric pressure.	11
Figure 4 – Comparison of NO _x emissions vs. air-fuel ratio for laser and electrical spark ignition [31]. Green points represent open chamber spark ignition, blue and red represents prechamber spark ignition.	16
Figure 5 – Output beam profiles of (a) 200/330 μm fiber and (b) 200/745 μm fiber. The thick clad (200/745 μm) fiber ($M^2 = 2.8$) has much better beam quality than the thinner clad (200/330 μm) fiber ($M^2 = 11$). [41]	32
Figure 6 – Test setup for fiber M^2 measurements.	35
Figure 7 – Fiber configurations tested. Fiber was 4 m in length for each case and held in a horizontal plane. (a) – straight. (b) – 14 cm loop. (c) – 8 cm loop. (d) – 70 cm 90 degree bend. (e) – “?” shape. (f) – 20 cm 270 degree bend.	36
Figure 8 – Energy required to form sparks in air at different pressures and pulse durations [59]. Fitted lines represent $p^{-0.5}$ dependence.	39

Figure 9 – Transmission efficiency versus input energy through straight, 4m fiber for (a) 30 ns pulses and (b) 50 ns pulses. The increase in efficiency near 16 mJ input energy is the result of SBS traveling back to the laser cavity, amplifying, and returning through the fiber. This resulted in incorrect transmission measurements.	43
Figure 10 – SBS investigation experiment. Red lines indicate laser beam coming from the laser, while transparent blue lines originated from the fiber.	44
Figure 11 – 50 hour static fiber test. Ordinate axis represents a fraction of the total output power.	46
Figure 12 – 50 hour vibrating fiber test. Ordinate axis represents a fraction of the total output power.	46
Figure 13 – Oil bath and CW vibration test setup.	49
Figure 14 – Beam profiles for different tested conditions. (a) – Fiber resting in trough ($M^2 = 5.4$). (b) – Fiber vibrating without oil ($M^2 = 9.2$). (c) – Fiber vibrating with oil damping ($M^2 = 6.5$).	50
Figure 15 – Configuration (a), 90 degree bend. Fiber highlighted in red. ≈ 50 cm radius of curvature.	52
Figure 16 – Configuration (b), 360 degree loop. Fiber highlighted in red. ≈ 60 cm diameter.	52
Figure 17 – Configuration (c), “?” shape. Fiber highlighted in red. Final bend ≈ 40 cm radius of curvature.	53
Figure 18 – Configuration (d), 3d “?” shape. Fiber highlighted in red. Fiber raises ≈ 40 cm from output tip and the curved section is ≈ 120 cm long.	53

Figure 19 – Beam path through output optics using ABCD approximation. The area within the blue lines represents the beam. The y axis has been exaggerated for clarity. The red dashed line is the beam axis. Optical train is as follows: fiber output at $z = 0$, negative lens at $z = 75$ mm, collimating lens at $z = 105$ mm, focusing lens at $z = 125$ mm, window at $z = 130$ mm.....	56
Figure 20 – Cutaway CAD model of the optical spark plug.....	58
Figure 21 – Assembled optical spark plug.....	58
Figure 22 – Exploded view of optical spark plug.	58
Figure 23 – CFR engine cross section. Both the laser and electric spark plugs were located in the detonation pickup hole, with the spark located 5mm from the top wall of the cylinder. The spark plug shown in this diagram was replaced with the pressure transducer.	61
Figure 24 – CFR engine test setup. Fiber highlighted in red.	63
Figure 25 – Average pressure traces for electrical and laser ignition systems at 6 bar NMEP. For the laser at AF20, the low energy spark is shown. The laser system could reach a minimum of 6.9 bar NMEP for the given 101 kPa intake pressure at AF20, while the electrical system ran at 6 bar. Hence, the peak pressure is higher for the laser at that air-fuel ratio.	67
Figure 26 – COV of NMEP at 6 bar.	68
Figure 27 – Brake specific fuel efficiency at 6 bar NMEP.....	68
Figure 28 – Position of 10%, 50%, and 90% mass burn fractions at 6 bar NMEP. Ordinate represents degrees ATDC.....	69

Figure 29 – Emission of NO _x , CO, and THC at 6 bar NMEP. All values are normalized to 15% O ₂ . The laser point represents the 3.8 mJ spark energy case.	69
Figure 30 - Average pressure traces for electrical and laser ignition systems at 8 bar NMEP. Where there are duplicate data points for the laser system (AF 24 and 28), the point with lower COV is shown. At AF28, this corresponds to 3.8 mJ spark energy.	71
Figure 31 - COV of NMEP at 8 bar.	72
Figure 32 - Brake specific fuel efficiency at 8 bar NMEP.	72
Figure 33 – Position of 10%, 50%, and 90% mass burn fractions at 8 bar NMEP. Ordinate represents degrees ATDC.	73
Figure 34 - Emission of NO _x , CO, and THC at 8 bar NMEP. All values are normalized to 15% O ₂ . Laser point at AF24 represents the test with lower COV.	73
Figure 35 - Average pressure traces for electrical and laser ignition systems at 12 bar NMEP. The AF36 trace is from the data point with 12 bar nominal NMEP.	75
Figure 36 - COV of NMEP at 12 bar.	76
Figure 37 - Brake specific fuel efficiency at 12 bar NMEP.	76
Figure 38 – Position of 10%, 50%, and 90% mass burn fractions at 12 bar NMEP. Ordinate represents degrees ATDC.	77
Figure 39 - Emission of NO _x , CO, and THC at 12 bar NMEP. All values are normalized to 15% O ₂	77
Figure 40 – Damage to focusing lenses in optical spark plug. Left: AR coated Gadium lens, sustained noticeable damage within 45 minutes. Incident beam was 9.2	

mJ, 25 ns, \approx 4.7 mm in diameter. Right: Uncoated SF11 lens, sustained noticeable damage within 2.5 hours. Incident beam was 9.2 mJ, 25 ns, \approx 7.0 mm in diameter.....	79
Figure 41 – Schematic of experimental setup used for measurement of n_e	90
Figure 42 – Plot of normalized laser pulse and oscilloscope signal $u(t)$. Data representative of the first point in Figure 43 ($I \approx 1.65 \times 10^{10}$), $l = 1$ cm, $U = 1$ kV.	92
Figure 43 – Electron density versus laser intensity. Linear fit corresponds to a dependence of $I^{2.3}$	93
Figure 44 – Schematic of experimental setup used to study dual pulse energy addition.	95
Figure 45 – Effect of preionization on the 1064 nm breakdown threshold as seen through the dependence of 1064 nm breakdown intensity versus 266 nm intensity. Results are for air and two pressures are shown. Points labeled “(a,b),” “(c,d),” and “(e,f)” correspond to the Schlieren images shown in Figure 46. See text.....	100
Figure 46 – Schlieren images taken at 600 torr, 1 μ s after 266 nm laser firing. Left column shows both beams overlapped while right column shows preionizing beam alone. Images correspond to data points with similar labels in Figure 45. Both the preionizing and energy addition beams enter from the left. Schlieren beam position remained fixed throughout experiment and scale applies to all images.....	101
Figure 47 – Shaker table with output optics required for spark formation.....	117

Figure 48 – CAD model of laboratory prototype for fiber vibration damping. Full (top), cutaway (middle), and exploded (bottom) views.	118
Figure 49 – Beam profiles for the fiber connectorized at both ends for (a) immersed in oil ($M^2 = 3.0$) and (b) straight with no oil ($M^2 = 4.7$).	121
Figure 50 – NMEP vs. intake air pressure. The air-fuel ratio for NMEP of 6, 8, and 12 bar are 20, 26, and 32, respectively for both ignition systems.	122
Figure 51 – Heat Release vs. Crank Angle for NMEP 6 bar, air-fuel 20. (NMEP of laser system in this case is actually 6.9 bar, while electric system is at 6 bar.) ...	122
Figure 52 – Heat Release vs. Crank Angle for 8 bar NMEP, air-fuel 26.	123
Figure 53 – Heat Release vs. Crank Angle for 12 bar NMEP, air-fuel 32.	123

1 Introduction

As a result of rising fuel costs and strict environmental regulations, the demand for increased efficiency and reduced emissions in natural gas engines continues to grow. Of particular importance is NO_x reduction, which can be achieved by lowering the temperature of combustion [1]. Two commonly used methods of lowering the combustion temperature are exhaust gas recirculation (EGR) and lean burn operation. Both methods involve adding gases to the combustible mixture that do not participate in the combustion reaction, thus absorbing energy and lowering the overall temperature. In order to regain the usable power lost from such a scheme, the brake mean effective pressure (BMEP) must be increased through the use of turbocharging or supercharging [2]. Current high BMEP engines run at pressures of 18 bar, although targets for future engines have been set at greater than 25 bar. An engine running at such high BMEP could be expected to see peak pressures and temperatures on the order of 50 MPa and 4000 K [3], which will present a unique set of design challenges. Of particular importance is the ignition source for these future engines, as conventional electric spark plugs require increased voltage to create breakdown at such high pressures. High voltage across the spark gap accelerates wear on the plugs and severely shortens their lifetime, leading to increased cycle to cycle variations in the engine as well as increased maintenance costs [4]. To keep pace with advancements of other engine technologies, alternative ignition sources need to be considered.

Many alternatives to spark ignition have been explored, including laser spark ignition, laser thermal ignition, homogeneous charge compression ignition (HCCI), plasma ignition, etc. [5,6]. The focus of this work is on laser ignition, which is most commonly accomplished by replacing a conventional electric spark plug with a laser source that has sufficient intensity to cause breakdown of the gas in the cylinder, initiating the combustion process. Use of this method began shortly after the laser was invented in the 1960's, when it was found that laser light could be tightly focused to create a spark in air [7]. Originally, the laser's utility as an ignition source was mainly for controlled experiments in the laboratory setting. It was used *in lieu* of traditional sources such as electrical sparks or chemical detonators because of the ease with which one could measure the ignition energy [8], as well as eliminate variables in combustion modeling [9]. As more combustion experiments benefited from laser spark ignition, the advantages of using such a source for practical applications became apparent. The first demonstration of laser ignition on an internal combustion engine was performed by Dale et al. in 1978 [10]. Since then, many researchers have studied laser ignited gas mixtures [11–17], as well as performed on-engine tests [5,6,18–20]. Despite the relatively abundant research, laser ignition has yet to be implemented on a production engine. Concerns about cost, safety, reliability, and ease of use have thus far kept laser ignition out of the market. By addressing some of these issues, the following work attempts to bring laser ignition one step closer to being a practical replacement for the conventional spark plug. Other work presented in this thesis concerns novel laser plasma formation schemes that may also, ultimately, benefit practical combustion systems. The remainder of this chapter provides a review of laser ignition including plasma formation, ignition,

and laser delivery methods, before concluding by defining the goals of the present research.

1.1 Electrical Spark Ignition

Conventional electric spark plugs work by applying high voltage across a pair of electrodes to cause breakdown of the gas between them. The ensuing arc provides the energy required to start the combustion process. Typical industrial spark plugs for large bore natural gas engines require electrode voltages of ≈ 30 kV, discharge around 180 mJ of energy, and have a spark duration of 400 – 500 μ s [17]. These devices have been the primary ignition source in combustion engines for over 100 years [1], and as such have become inexpensive, easy to install, and widely available. Recently, however, the price of spark plugs for large industrial engines involved in power generation and natural gas compression has increased as these engines move to leaner, higher BMEP operation. The reason for this increase relates to the difficulty in igniting a high density, lean mixture. As density increases, the charge begins to act as an insulator, requiring an increase in the voltage across the electrodes. This increase is difficult to manage; it requires pushing ignition coils passed their current limits [5], and can lead to breakdown outside the combustion chamber from the ignition leads [20]. Future engines will require voltages ≥ 40 kV [6], which will be difficult to attain with existing systems and will further motivate interest in alternative ignition systems.

Even if the difficulties with generating and delivering such high voltages are solved, wear to the electrodes will continue to limit the use of conventional spark plugs. In order to achieve reliable engine operation, the gap between electrodes must remain within a certain tolerance. Exceedingly high voltages cause erosion of the electrodes,

increasing the gap and requiring the engine be shut down for maintenance. Currently, a typical gap must be adjusted every 1000 – 4000 hours, and there is a push in the industry to increase this time to 8000 hours [6]. Increasing the BMEP of the engine further exacerbates the problem; a study by GE Jenbacher found that increasing the BMEP from 17 to 22 bar reduced the service life of a spark plug by 50% [5]. Figure 1 shows results from their study. The effects of spark plug erosion can be clearly seen by the required increase in spark voltage as time progressed. Also of note is the lifetime as a function of BMEP, with increasing load significantly decreasing the spark plug lifetime.

The final problem with spark plugs is their inability to ignite exceedingly lean mixtures close to the flammability limit. Ultra lean flames tend to propagate at a slower speed than near stoichiometric flames, resulting in longer burn durations within the cylinder. Using traditional spark ignition, lean operating conditions can lead to less complete combustion, increased cyclic variations, and occasional misfires [13]. With the addition of quenching effects of the electrodes as well as the spark plug's proximity to the cylinder wall, lean mixtures become exceedingly difficult to ignite. One solution lies in increasing the flame speed, but many methods of accomplishing this have drawbacks of their own. The addition of turbulence can speed the flame, but results in increased heat transfer. Similarly, higher peak temperatures can be used at the expense of NO_x production [13]. Ideally, one desires an alternative ignition source which can maintain a low combustion temperature as well as increase the flame speed to achieve stable engine operation. Many studies have shown that laser ignition may provide such an alternative.

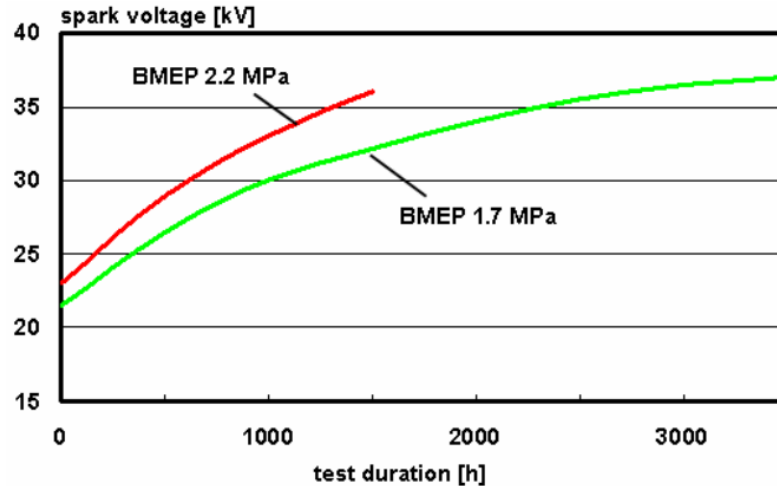


Figure 1 – Service life of spark plugs and required electrode voltages for two different BMEPs [5].

1.2 Laser Ignition

Laser ignition can be separated into four different categories based on how the laser energy is deposited in the mixture [1].

1. *Nonresonant breakdown:* Laser light is tightly focused so that the intensity exceeds the breakdown threshold of the gas. Once breakdown is achieved, a plasma spark is formed which absorbs the laser energy. Energy is transferred to the combustion gases from the spark and starts the reaction [3] (See section 1.2.2). Wavelength of the laser source is not of fundamental importance. Although wavelength plays a role in the physics of breakdown, for visible and near infrared sources the primary requirement is beam intensity. The fiber delivery and engine testing presented in this thesis employ non resonant breakdown as the ignition mechanism.
2. *Resonant breakdown:* This method is similar to nonresonant breakdown in that the end result is a plasma spark. It differs in how that spark is created, making

use of resonant energy levels in atoms or molecules (in the case of combustion, this molecule is often O₂) [21]. In this case, the wavelength of the laser must be tuned to the particular resonance. This lowers the number of photons required for photoionization, and hence the amount of energy required to cause breakdown.

3. *Thermal ignition:* Thermal ignition requires no electrical breakdown. Here the laser is used to heat a volume of fuel/oxidizer by exciting translational, rotational, or vibration modes of the molecules. The energy deposited causes molecules to break apart, and the resulting radicals are used to start the combustion reaction. In order for this process to work, some part of the mixture must be a strong absorber of the laser wavelength used. As such, this method is commonly used to ignite solid fuels such as rocket propellant due to their absorption of infrared wavelengths [3]. The work presented in Chapter 4, using preionization, relates to thermal ignition.
4. *Photochemical ignition:* This method starts ignition by creating radicals, and in general does not heat the gas as do the previous three methods. Strong absorption by one of the species is required, and hence the energy requirements are generally low, typically less than 1 mJ [3]. Photons, typically UV for many combustible fuels, dissociate molecules into radicals which start the chain-branching process, causing ignition.

Out of the four methods presented above, nonresonant breakdown is the most commonly used, due to its less restrictive wavelength requirement and the availability of high power solid state lasers. Laser availability remains one of the largest barriers to the practicality of resonant breakdown and photochemical ignition, as tunable UV lasers tend

to be expensive and much more difficult to use than solid state infrared lasers. Thermal ignition is difficult to achieve locally because absorption by the mixture tends to cause a broad heated region, rather than a sharp kernel as seen in breakdown mechanisms. As such it is used primarily in homogeneous ignition experiments, and its utility as an ignition source for engines has not been well studied.

1.2.1 Plasma Formation

Since the most common methods of laser ignition make use of a plasma spark, the underlying physics of breakdown is of considerable interest. In order to create a spark in any medium, the breakdown intensity must be met or exceeded. Breakdown intensities are dependent on the type of molecules, the laser wavelength and pulse duration, and in gases there is a strong dependence on the pressure. For air at atmospheric pressure, reported breakdown intensities using 1064 nm light range from 100 to 300 GW/cm² [12,14,22]. Differences in reported values can arise from variations in optical setups, the presence of impurities, and focal spot sizes. Experimental determination of the pressure dependence of the breakdown threshold has been characterized with the following equation:

$$I_{th} \propto p^{-n}, \quad (1)$$

where n is dependent on the wavelength and the type of gas. Generally, shorter wavelengths exhibit a higher dependence on pressure than longer wavelengths, the latter requiring less laser energy at lower pressure than the former. This is thought to be caused by diffusion loss out of the focal volume which becomes more significant as the focal volume is decreased [23]. Phuoc [14] reported a value of n of 0.65 for air at $\lambda = 532$ nm, and 0.4 at $\lambda = 1064$ nm. A value of $n = 0.45$ was reported by Chylek [24], and $n = 0.54$

by Bradley [12], both using 532 nm light. Differences in values can be attributed to differences in optical setups, laser pulse widths, and beam profiles. Figure 2 shows experimentally determined curves of breakdown intensities for gases and conditions of interest to laser ignition.

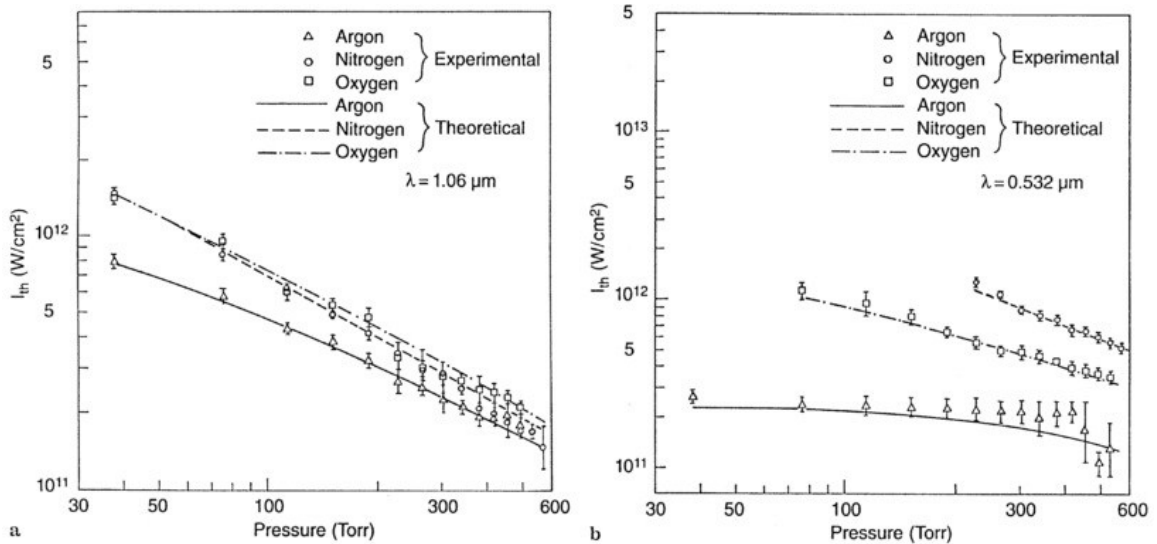


Figure 2 – Experimentally determined breakdown thresholds of argon, nitrogen, and oxygen for laser wavelengths of (a) 1064 nm and (b) 532 nm for various pressures [22].

Much of the literature on nonresonant breakdown processes including the present work performed has been done with wavelengths in the visible to near infrared. Typical combustion gases are highly transparent to this part of the spectrum, and as such will not readily absorb laser energy. These wavelengths will however be strongly absorbed by free electrons (created by ionization of the air or combustion species). The commonly accepted process for electron liberation is known as multi-photon ionization (MPI) i.e., the process in which a gas molecule or atom simultaneously absorbs multiple photons to ionize the molecule and eject an electron. Ionization potentials for common combustion species are much higher than the photon energies of visible and infrared lasers, hence multiple photons are required. For example, the ionization potential for O_2 is 12.07 eV

and for methane is 15.43 eV, while the photon energy of 1064 nm light is only 1.17 eV [14,25]. Thus, over 10 photons of 1064 nm light are needed to ionize molecular oxygen. The likelihood of 10 photons being simultaneously absorbed by the same molecule is very small, and is the primary reason such high intensities are needed to cause breakdown. The presence of impurities in the gas such as aerosol particles, dust, or vapor can lower the breakdown threshold intensity because their ionization potentials are significantly lower (< 1 eV), or they absorb energy at the wavelength used [25]. While generally responsible for creating seed electrons, multi-photon ionization is not typically the dominant breakdown mechanism unless using short wavelengths (< 1 μm) or very low pressures (< 1 kPa) [3].

The dominant breakdown mechanism under conditions of interest to laser ignition is electron avalanche ionization (EAI). This process requires the presence of initial free electrons, which can be created through multi-photon ionization or ionization of impurities in the gas. The presence of ions and free electrons allow the radiation to be absorbed by the inverse bremsstrahlung process, increasing the kinetic energy of the charged particles [3]. Initially, when the degree of ionization is low, electron-neutral inverse bremsstrahlung is dominant, and at higher electron densities, electron-ion inverse bremsstrahlung becomes dominant. Absorption coefficients for each are given by Bradley et al. [12]. Inverse bremsstrahlung favors longer wavelengths (EAI threshold intensity has ω^2 dependence, where ω is the lasers angular frequency [26]) like those typically used for laser ignition (visible, infrared). When the electrons gain sufficient energy, they ionize other gas molecules on impact, creating an avalanche of electrons which leads to full breakdown.

Most non-resonant breakdown makes use of both multi-photon ionization and electron avalanche ionization contribute to the plasma creation. Under typical engine conditions with nanosecond pulses, multi-photon ionization is responsible for the generation of seed electrons, while electron avalanche ionization is responsible for actual breakdown. Under certain conditions, multi-photon ionization can be the sole mechanism responsible for breakdown. The transition point from one process to the other is generally agreed to be when

$$p\tau \approx 10^{-7} \text{Torr} \cdot \text{s} \quad (2)$$

where p is the pressure and τ is the laser pulse duration [26]. Values of $p\tau$ less than the RHS of equation 2 are typically dominated by multi-photon ionization, and values greater are dominated by electron avalanche ionization. Short duration pulses in the pico and femtosecond range will primarily result in multi-photon ionization because the laser flash is too short to cause electron collisions that result in electron avalanche ionization. Multi-photon ionization is also more prevalent at shorter wavelengths (typically ultraviolet), because less photons are required for ionization due to their higher energy.

1.2.2 Ignition

Once breakdown has occurred and the laser pulse has stopped inserting energy into the focal volume, the plasma begins to decay. The energy released in this decay is responsible for developing the flame kernel, which ultimately leads to combustion and the consumption of the fuel air mixture. The onset of combustion involves competing processes by which energy is generated (from the chemical potential of the fuel) through chemical reaction and wasted through radiation, diffusion, and expansion. If the plasma contains insufficient energy or enough of the energy is wasted, heat and radicals will be

conducted away from the surface of the kernel faster than they are generated by chemical reaction, and the kernel will be extinguished after consuming only a small quantity of reactants. If however, the plasma contains enough energy to overcome the loss, heat and radicals will be created faster than they are lost and a self-sustaining flame will be created that consumes all of the available mixture [1]. This threshold is known as the minimum ignition energy, and is dependent on temperature, pressure, air fuel ratio, etc. Values for the minimum ignition energy can be computed using methods described by Tauer [25], Ronney [1], or Sloane [16], resulting in typical values from 0.1 to 0.8 mJ for CH₄-air mixtures at varying air-fuel ratios. Experimental methods can only determine the minimum laser energy required for ignition (minimum pulse energy), as much of the energy deposited in the plasma is lost to the shock wave it creates, and does not contribute to ignition [3]. Typical values for CH₄ are summarized in Figure 3 by Kopecek [27]. Notice that minimum pulse energies are in the 10 – 20 mJ range for lean conditions even though most of the energy is not responsible for ignition.

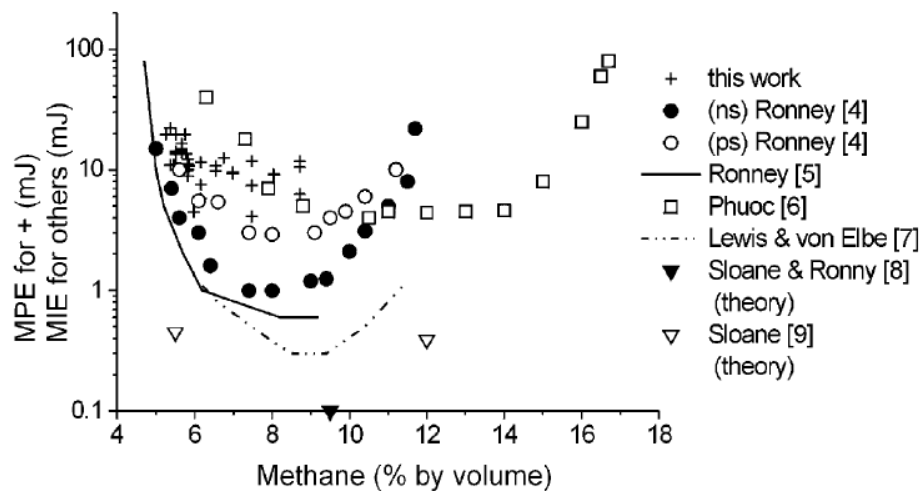


Figure 3 – Minimum pulse and ignition energies for methane at different air-fuel ratios [27]. References in legend are with respect to the cited source in this caption. Points denoted with a “+” symbol are at 3 MPa, all other values are at atmospheric pressure.

As the spark evolves, it continues to absorb laser radiation and grows in size. The physics of this process involves complex gas dynamic effects which has been explained in the literature [3,7,12]. The rapid addition of energy from the laser ultimately results in a blast wave that quickly expands from the plasma. One theory, known as the blast wave ignition model, suggests that the energy from this wave is what causes ignition. The quick expansion does work on the surrounding gas and heats it to a temperature above the threshold ignition temperature. The chemical reaction is then coupled to the shock wave. As the shock wave begins to decay, the now self-sustaining combustion reaction continues to consume the remainder of the mixture. This mechanism, however, is not well supported by experimental data [3]. Due to the dynamic nature of the shock wave and the rate of its expansion, the surface area of the developing flame increases very rapidly, resulting in flame stretch that can extinguish or inhibit the propagation of the flame. Calculations by Syage [28] have shown that more than 10^3 mJ are required to ignite stoichiometric H₂ and air by this mechanism, far more than the observed minimum ignition energy. In addition, there exists a chemical induction time, which is the amount of time the ignition source must remain above the ignition temperature for the reaction to generate enough heat on its own to become self-sustaining. Typical induction times are around 4 ms near stoichiometric conditions, and increase to near 6-8 ms for lean and rich mixtures [3]. Blast wave decay times are on the order of 10 μ s, much shorter than the chemical induction time. It has been concluded that while the shock wave may aid in mixing or creating intermediate reaction species, it cannot be completely responsible for ignition.

The currently accepted ignition model is the hot gas model, in which the blast wave decays, leaving behind a volume of hot gas which heats the ambient mixture above the ignition temperature. The residual energy has been calculated by Phuoc [3] using a blast wave model and by Edmonson [29], who assumed an adiabatic expansion of an ideal gas. The analysis done by Edmonson pertained to an electric spark, and did not take into account the dynamic nature of a laser spark. Both analyses determined a sufficient amount of energy remained after the blast wave dissipated to exceed the minimum ignition energy. It has been shown that for 1064 nm laser pulses of sufficient energy to cause breakdown, over 90% of the laser light is absorbed by the spark [15]. Of this energy, approximately 70% is consumed by the blast wave expansion. Radiative losses, both bremsstrahlung loss and blackbody radiation loss, consume approximately 20% of the spark energy. The thermal energy that remains in the hot gas accounts for only 7-8.6% of the total spark energy [30]. Results of a study quantizing the different loss mechanisms for various spark energies are shown in Table 1.

Table 1 - Energy balance for laser spark in air [3].

Spark energy (mJ), E_{sprk}	15	22	30	35	44	50
Shock energy (mJ) E_{shock}	10.6	15	19.2	21.8	27.1	28.6
Remaining Energy (mJ) E_{ign}	1.05	1.48	2.64	2.97	3.21	4.29
E_{shock}/E_{sprk} (%)	70	68	64	62	61.6	57
Bremsstrahlung loss (mJ)	2.30	3.45	4.65	4.77	5.62	5.99
Blackbody loss (mJ)	1.04	2.06	3.49	5.44	8.05	11.1
Convective loss (mJ)	0.01	0.013	0.016	0.017	0.019	0.02
E_{loss}/E_{sprk} (%)	93	93	91	92	92.7	91.4
E_{ign}/E_{sprk} (%)	7	7	9	8	7.3	8.6

Although the blast wave is not directly responsible for ignition, its presence is responsible for one of the main differences between laser and electric spark ignition. Due

to the violent expansion and gas dynamic effects of a laser plasma as well as the generation of reactive species during breakdown, laser ignited kernels experience an “overdrive” early in their formation, where the flame speed is much higher than the laminar flame speed [12]. The effects of increased early flame speed are most prominent in leaner mixtures, where propagation has been found to happen at speeds up to seven times faster than the laminar flame speed at near atmospheric pressure. As pressure is increased, the flame speed is not quite as overdriven, but still above the laminar flame speed. Near stoichiometric conditions, the effect is not as pronounced, but still propagation speeds of 3 times the laminar flame speed have been measured, and are not strongly dependent on pressure. This overdrive lasts for approximately 1.5 ms, much longer than the duration of the original plasma. Typical electric sparks exhibit the opposite behavior, where early flame kernels propagate below the laminar flame speed, and converge towards it as time progresses. With the increased early flame speed due to the dynamics of the laser spark, the rate of flame propagation can be slightly increased. Near the lean limit however, laser ignited flame kernels can become so overdriven that the high rate of stretch extinguishes the flame. Due to this, laser ignition does not favor extreme lean conditions, but tends to work best under fuel rich conditions where flame speeds are slightly higher than that with traditional spark ignition [15]. Lean operation can be achieved, however, if higher pressures are utilized to slow the flame kernel propagation to a suitable level. Higher energies have also been shown to help, as they feed the early flame kernel for a longer period of time, allowing the reaction time to become self-sustaining.

1.2.3 Potential Benefits

Laser ignition has many potential benefits that make it an attractive replacement for traditional spark ignition. These benefits are listed below.

1. *Allows for extension of lean operation, lowering NO_x emissions.*

As the engine's lean limit is approached, the coefficient of variation (COV) of BMEP increases due to misfires causing instability in the engine. The lean limit is generally determined by the point at which the engine's COV reaches a certain point, above which the engine is considered unstable. Low COVs are extremely important to large bore engines, as a high COV results in increased emissions due to occasional incomplete combustion. As the amount of laser energy that can be transmitted to the engine cylinder increases, the COV decreases accordingly. Under extreme lean burn conditions, traditional spark ignition will begin to misfire causing unacceptable COVs at a higher equivalence ratio than laser ignition. It has been shown in a study by Bihari et al. [18] that while a spark plug displayed unacceptable COV at an equivalence ratio of 0.55, laser ignition was able to maintain an acceptable COV until 0.5, thus extending the lean limit.

Studies have shown that the low combustion temperature resulting from lean burn laser ignition can significantly lower levels of NO_x emissions as well [5,18,31]. This is shown in Figure 4 in a laser ignition study by GE Jenbacher [31]. In this figure, the yellow circle is the only laser ignition data point. The green lines represent spark ignition directly in the combustion cylinder and the red and blue lines represent pre-chamber spark ignition of two different volumes.

While there is only one data point, it is evident that NO_x emissions have been significantly reduced with laser ignition. Laboratory studies have shown the utility of laser ignition in igniting mixtures much leaner than traditional spark plugs. Weinrotter [17] has shown that the lean ignition limit could be extended from an air fuel equivalence ratio (λ) of 1.65 to 2.0 using laser ignition under typical engine pressures of 1.5 MPa.

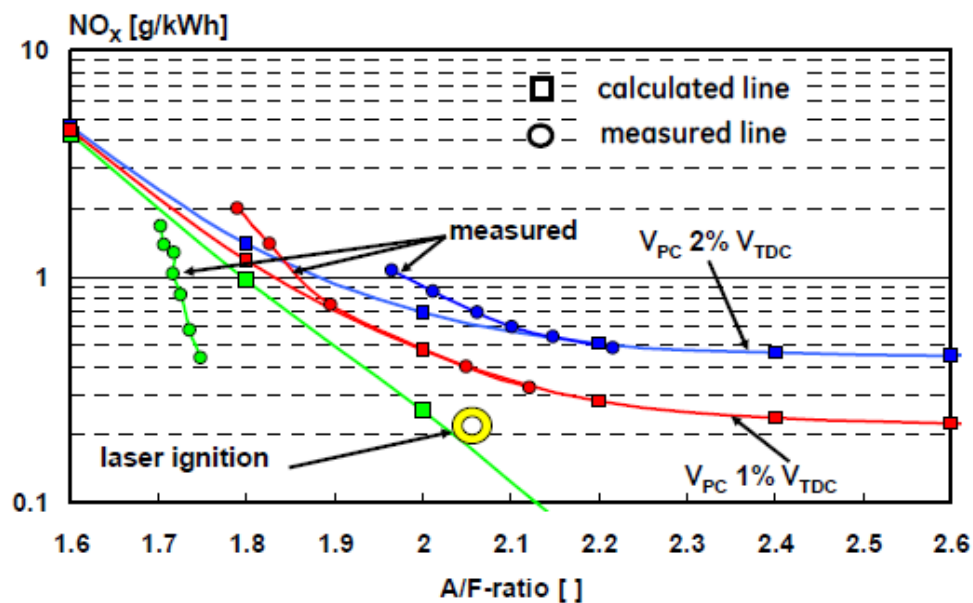


Figure 4 – Comparison of NO_x emissions vs. air-fuel ratio for laser and electrical spark ignition [31]. Green points represent open chamber spark ignition, blue and red represents prechamber spark ignition.

2. *Allows for ignition at higher BMEP operating conditions.*

Increased BMEP often comes as a result of increasing the compression ratio (or amount of forced induction), which increases the thermal efficiency through the thermodynamics of the engine [5]. This is a large benefit on its own, but becomes increasingly important when combined with lean burn to reduce NO_x

emission. Lower ignition temperatures lower the power output of the engine, a deficiency that can be accounted for by increasing the BMEP.

3. *Positioning of spark inside chamber.*

Laser ignition allows for more flexible positioning of the spark inside the combustion chamber, as well as a simplified method for implementing multi-point ignition. Positioning of a laser spark is non-intrusive and is limited only by the ability to focus the beam to a sufficient intensity. Given enough laser power, the spark could be moved further from the cylinder wall simply by increasing the focal length of the focusing lens. Several studies [32,33] using CFD modeling have shown that there are clear differences between spark locations within the combustion chamber, indicating an optimum location exists. In addition, multi-point ignition can easily be implemented by splitting the laser beam before it enters the engine, or by using a diffractive lens [13]. A study by Phuoc [34] has shown that multi-point ignition increases the combustion pressure and significantly shortens the combustion time, making it an attractive approach for lean burn engines.

4. *No quenching from electrodes.*

The absence of electrodes near the ignition source means the early flame kernel cannot be quenched by heat loss to the spark plug. Spark plugs position the kernel essentially between two parallel plates, and due to quenching effects, the flame propagates very slowly in the direction normal to the electrode surface [4]. Since one direction is impeded, the kernel expands almost in a two dimensional plane. This is why early flame speeds from spark plugs tend to be

below the laminar flame speed. The laser spark's position in free space allows it to expand in three dimensions, resulting in a rapidly propagating flame.

5. *Potential for low cost and high reliability.*

As discussed previously, forming sparks by focused laser light becomes easier at higher pressures. This is beneficial from a reliability standpoint due to spark plug erosion. With no electrodes in the chamber, there is no wear on ignition system components, which is known to increase at higher BMEPs. This means the engine does not need to be shut down for maintenance as often and results in decreased down time and maintenance costs.

1.3 Laser Pulse Delivery

One of the main issues preventing laser ignition from transitioning from a lab environment to industry is the method of delivering the laser pulse to the engine cylinders. Problems associated with ruggedizing lasers and required optics for use in typical engine conditions, such as dirt, vapors, heat, and vibration need to be overcome. Issues with cost, ease of maintenance, and personnel safety have also prevented the technology from being put to widespread use. Several solutions to these problems have been proposed, each with their own benefits and drawbacks. The following is a discussion of the different laser delivery methods attempted to date.

1.3.1 Open Path Beam Delivery

The first laser ignition experiment performed on engine by Dale et al. [10] as well as many experiments following [5,18,32,35] made use of an open path beam delivery scheme. This method places a laser near the engine and uses mirrors to steer the beam

into the combustion chamber. The advantage of this scheme is the ease in which it can be set up in the laboratory and the freedom it gives to measure various facets of operation. Also, the laser beam can be set up in such a way that beam quality is preserved and high damage threshold optics will not severely limit the power that can be transmitted. Hence, open path systems are particularly well suited to laboratory experiments, where fine control of variables is desired. In an industrial setting, this scheme is much less practical. Of primary concern is safety, as high power laser pulses moving through open space can be a hazard to personnel working on or near the engine. Engine vibration is also a major issue. Precise alignment of the laser beam with the focusing optics in the engine cylinder is required to form a spark. If the engine vibrates relative to the laser source with sufficient magnitude to cause misalignment, the system may no longer work. This can be alleviated by mounting the laser on the engine, but that subjects the laser to vibration as well as heat which most lasers are not designed to handle. Vibration can also cause steering mirrors to move over time, resulting in misalignment of the beam. Finally, the optics are openly exposed to the engine environment, which is often full of dust, vapors, and particulates. Over time, these contaminants can coat mirrors and lenses, which results in poor beam quality, loss of transmission, and even damage to the optics. Due to these problems, open path beam delivery has been deemed an unacceptable method of implementing laser ignition in industry.

1.3.2 Single Laser per Engine Cylinder

A convenient method to avoid many of the issues plaguing open path setups would be to place a laser directly on each cylinder. This way there are no exposed laser beams presenting a hazard to personnel, and issues with maintaining alignment would be

avoided. Problems associated with energy loss and degraded beam quality would be avoided as well, as the beam only has to pass through a limited number of optics before entering the combustion chamber. The technical challenges involved in creating a compact, durable laser suitable for on-engine conditions are many, but several potential systems have been demonstrated. Kroupa, et al. [36] designed a miniature diode pumped Nd:YAG laser with a Cr:YAG saturable absorber as the Q-switch. It was able to produce 25 mJ, 3 ns pulses at a rate of up to 100 Hz. With an integrated focusing lens which focused the beam to a waist of 50 μm , breakdown in air was easily achievable at focal lengths up to 80 mm. On-engine tests showed the laser was reliable and extended operation further into the lean regime as compared with an electrical spark plug. Inohara et al. designed and patented a similar system [37] which also uses a saturable absorber as a Q-switch and is also diode pumped. The laser emits a train of pulses with temporal spacing between 10 and 300 μs , with a total energy of about 7 mJ. On-engine tests of this laser also showed a slight extension of the lean limit when compared with an electrical spark plug.

While results of these developments are promising, there are still many factors that limit their practicality for widespread use. Both the diodes and the gain medium need to be temperature controlled to prevent wavelength drifting and thermal lensing, which requires a separate cooling unit, or an attachment to the engines cooling system. Reliability issues will need to be addressed as well. While no long term tests have been performed, Kroupa reported a decrease in pulse energy after several million shots, as well as concern that the laser cavity may become misaligned due to constant vibration.

Finally, the cost of multiple lasers must be considered, especially for large multi-cylinder engines where many lasers would be required.

1.3.3 Fiber Delivered Diode Pump

One possible solution to the cost issues associated with placing a laser on each cylinder would be to place a gain medium on each cylinder and send pump light through fiber optics multiplexed from a single source. Kofler, et al. [38] built such a system that could produce 6 mJ pulses with duration below 1.5 ns. While no on-engine test was performed, the authors acknowledged further research was needed to determine the influence of heat and vibration on their design. This method has the advantage of needing only one set of expensive laser diodes that could be placed away from the engine. The light from the diodes could easily be transmitted by fiber optic cable because of its low peak power, eliminating fiber reliability issues. While certainly less expensive than placing a laser on each cylinder, this scheme still requires multiple laser gain crystals. Since each gain medium is in close proximity to the combustion chamber, proper thermal control is essential.

1.3.4 Fiber Delivered Laser Light

Delivering the laser pulses themselves through fiber optic cables allows the laser source to be placed away from the engine, in many cases free from vibration and heat. In this scheme, only one laser source is required, which may be favorable for low cost. The laser pulses are multiplexed into fibers and then to optical spark plugs containing collimation and focusing optics, which form the spark in the combustion chamber. Due to the relative freedom of laser placement, restrictions on size imposed by the single laser

per cylinder and diode pumped delivery methods are not as much of a concern. The main technological challenge, are the limitations imposed by fiber delivery. To begin, accurately and reliably multiplexing light into a bundle of fibers is a technical challenge. Many studies have outlined the importance of proper beam conditions at the fiber input face in order to preserve beam quality [39–43]. Accurately positioning the laser beam on to many different fiber faces, typically less than 1 mm in diameter, at rates up to 240 Hz requires very precise components and painstaking alignment. Attempts at multiplexer designs have been made such as those described by Yalin et al. [44] and Reynolds [45], who steered the beam by mirrors which are mechanically moved by a galvanometer. Other designs incorporate optoelectronics that rapidly switch the polarization of light allowed to transmit through them, but such systems currently have too much loss. Assuming proper alignment can be reliably obtained, transmitting light with enough energy for ignition and sufficient beam quality to create a remains challenging. Many types of fibers have been explored and tested for their suitability to this application. What follows is a description of each fiber type and its history and potential for use with laser ignition.

1.3.5 Hollow Core Fibers

Two types of hollow core fibers have been tested for use in laser ignition; dielectric capillaries and hollow glass fibers with cyclic olefin polymer-coated silver. The dielectric capillary type is a simple hollow glass tube that guides light by reflection at the air-glass interface. Studies by Stakhiv [46] have shown this fiber is capable transmitting 15 mJ without damage, producing a mono mode output, and stable sparking using a 4.5 mm focusing lens. Unfortunately, in terms of a practical delivery system they

are almost useless. The walls of the glass tube only reflect light at near grazing incidence, resulting in high losses which lower the transmission to about 50%. They are also very inflexible, negating one of the primary benefits of fiber delivery.

Cyclic olefin polymer-coated silver hollow fibers, on the other hand, are much more flexible and have much better transmission efficiency. These fibers are made from a much thinner wall glass tube with a polymer and a silver layer inside to guide the light. Yalin et al. [47] reported the first use of these fibers to form sparks in atmospheric air. Using 700 μm core 1 m long fibers, transmissions of 70 – 80% were measured for pulses of 47 mJ. This resulted in a spark formation rate of 97%, after the light exiting the fiber was tightly focused. Beam quality measurements reported M^2 values from 11 – 26, depending on launch conditions, with smaller launch divergence angles giving lower M^2 . The effects of bending were also studied, and showed that tighter bend radii resulted in decreased transmission efficiency and increased M^2 , decreasing the ability to form sparks. Continued research with 1 mm core 2 m long fibers [42] yielded similar results. Due to the added length and increased core diameter, additional mode coupling resulted in slightly increased M^2 for the best launch condition ($M^2 = 15$), but sparking rates remained similar. Slightly better bending performance was observed, but was a result of the increased fiber length allowing for a larger radius of curvature. Finally, the first demonstration of fiber delivered laser ignition was accomplished using hollow core fibers [20]. Results of the study showed 100% reliable ignition in the laser ignited cylinder, which was delivered by a 1 m hollow core fiber in a straight configuration.

Generally, hollow core fibers have the highest damage threshold of all fiber types, due to the lack of solid material in the core. The high threshold allows large amounts of

energy to be transmitted, although care has to be taken to avoid air breakdown at the input when focusing the laser beam onto the fiber face. The engine testing presented in [20] required the fibers input face be in vacuum to avoid breakdown. Hollow core fibers are highly susceptible to transmission loss and beam quality degradation by bending and vibration. These factors limit the practicality of such a system, as vibration is always present on engines and packaging constraints may require the fibers to be bent.

1.3.6 Solid Core Fibers

Solid core fibers have long been used in the telecommunications industry and have been extensively studied. Until recently, they were thought to be incapable of transmitting the high intensity pulses required for laser ignition. The reason for this is a combination of the damage threshold of typical fused silica fibers and the number of modes they will support. Damage thresholds have been reported between 135 and 570 J/cm² for ≈ 10 ns pulses, depending on the wavelength of radiation and the core size of the fiber [48]. Generally, larger cores can carry higher energy pulses because the energy is spread over a larger area, however the authors of [48] suggest the processes involved in manufacturing tend to decrease the irradiance that smaller core fibers can handle. Under conditions typical of a laser ignition system, fibers generally have much lower damage thresholds, < 5 GW/cm² [49]. Mode coupling and degradation of beam quality also contribute to the difficulty of using solid core fibers. In communications, single mode fibers are used because their small cores (≈ 8 μm diameter) support only a single mode, resulting in a near Gaussian spatial output. Such fibers are unsuitable for high power applications because demagnification of the output beam is difficult when it exits the fiber with such a small diameter. Larger core fibers will handle the necessary energy, but

the resulting increase in M^2 does not allow the beam to be focused tightly enough for spark formation. A study on the effects of core diameter on beam quality showed this relationship [41] by focusing a HeNe laser into commercially available step index multimode fibers of various core size, to measure the resulting M^2 . It was found that a core size of 100 μm resulted in an M^2 of 3.8, which increased with core size up to 400 μm with M^2 equal to 7. An interesting result was that increasing the clad diameter reduced the M^2 for a given core size. For instance, increasing the clad diameter from 140 μm to 660 μm for the 100 μm core fiber decreased the M^2 to 1.6.

Recent work at CSU has shown the ability to produce sparks in atmospheric air using 400 μm core, 720 μm clad fibers and nanosecond pulse 1064 nm light. However, the spark required controlled laboratory conditions to create. Due to the decreased breakdown threshold and higher pressures, sparks have easily been created under engine-like conditions with solid core fibers. A study by El-Rabii [49] used fibers with core sizes of 200, 400, and 940 μm to try and initiate ignition. At atmospheric pressure, only sporadic spark formation was observed, attributed to the presence of dust in the focal region. At higher pressures, however, sparking became possible and a 90% spark rate was observed in air at 6 bar. Ignition was possible with 30 mJ pulses when focused onto atomized droplets of fuel.

A couple of engine tests have been performed thus far indicating the potential for solid core delivery. In a study by Mullett et al. [50], 400 and 600 μm core fibers were used to run a single cylinder of a four cylinder engine. While they were able to ignite the cylinder with the laser, there were a significant number of misfires. The 400 μm core fiber at best was able to ignite approximately 13% of 300 consecutive combustion cycles,

while the 600 μm core fiber was able to ignite approximately 44% of the cycles. This is a promising result, although the performance falls well behind the 100% ignition rate shown in hollow core fiber tests. A more successful on-engine test was performed by Biruduganti et al. [6], using a 1 mm core fiber. While the system was not able to successfully initiate breakdown in air, it was able to run a single cylinder engine without misfire. Due to limitations of the experimental setup, only a single air fuel ratio and load point was considered, near the stoichiometric region ($\lambda = 1.11$). Fiber performance in both these tests was limited by their ability to tightly focus the beam to cause breakdown. As will be shown in this thesis, increasing the clad dimension decreases M^2 , allowing for more reliable spark creation in the combustion chamber and improved performance of this system.

1.3.7 Photonic Crystal / Photonic Band Gap Fibers

Recent work with relatively new photonic crystal fibers and hollow core photonic crystal fibers (photonic band gap fibers) has shown some potential for use with laser ignition. These fibers have small cores with a periodic two dimensional structure as the cladding, which allows them to operate in only a single mode. This is a huge advantage over typical fibers, as the output beam can be tightly focused to easily cause breakdown. Early experiments showed only photonic band gap fibers would be of use to laser ignition, as the solid core of a photonic crystal fiber is damaged by high intensities [46]. Later work made use of large mode area photonic crystal fibers that could further increase the damage threshold [42]. This research showed that high transmissions could be achieved under low power (97% at ≈ 0.05 mJ input), and transmission dropped as the input energy was increased. The largest achievable input energy was 1.3 mJ, with an

output energy of only 0.55 mJ. While the high quality beam offered by these fibers is certainly attractive, further study is required to better characterize their power handling capability.

1.3.8 Fiber Lasers

Use of active fibers for laser ignition has shown significant potential in recent years. By using a Yb-doped fused silica core and pump light from laser diodes, laser pulses can be generated and amplified within the fiber itself. Using such fibers would eliminate complexities involved with multiplexing and alignment of input beam with fiber face, but would require an active fiber for each cylinder, significantly negating the cost benefit of fiber delivered systems. In addition, their performance is bound by the same limitations as solid core fibers. Small core diameters are required to produce high quality output beams, but limit the amount of energy that can be safely transmitted. Large core fibers can handle higher energies, but suffer from degraded beam quality. The advantage of amplifying light within the fiber is that long lengths are required to generate sufficient gain, resulting in long pulse durations. By widening the pulse and increasing the energy, the peak power remains unchanged. As damage threshold scales with power, the damage threshold of the fiber is not exceeded, but enough energy is generated to allow for ignition of lean mixtures. The first fiber laser showing potential for laser ignition was created by Cheng et al. [51], which made use of multi stage fiber amplifiers of varying sizes. The final high energy beam was generated in a 200 μm core, double clad fiber 3.5 m in length. Output powers of 82 mJ for 500 ns pulses and 27 mJ for 50 ns pulses were reported. The large core diameter supported many modes resulting in a M^2 of 20, but they found by coiling the fiber, high order modes were lost and the M^2 dropped

to 6.5. These numbers are suitable for plasma generation in engine-like conditions, and may be useful in the future. Current fiber lasers are impractical due to the large amount of equipment used to generate the beam, as well as sections of open path laser travel.

1.4 Problem Statement

While there have been several tests showing the potential of laser ignition for lean burn natural gas engines, the development of such a system for widespread use is still in its infancy. Laser ignition work performed at CSU has been primarily in pursuit of developing fiber delivered laser ignition systems using a single laser. While two studies have been presented in this introduction [6,50] that use solid core fibers for laser delivery, neither provided a comprehensive, successful demonstration and test of the concept. This thesis focuses on three objectives: 1) developing a solid core fiber delivery system for laser ignition, 2) providing a comprehensive engine test of the delivery system including different load conditions and lean operation, as well as a comparison with electric spark ignition, and 3) preliminary studies aimed at using dual laser pulses with preionization to improve the laser plasma as an ignition source. Chapter 2 contains the empirically based development of a fiber delivery system for laser ignition. Tests were performed to determine the durability of the fibers, behavior in the presence of vibration, beam quality and power requirements, as well as the design of an optical spark plug. Chapter 3 presents the results of a single cylinder laser ignition engine test using the system developed in Chapter 2. The test contains data points for several different load conditions and air-fuel ratios for both laser and electrical spark ignition. Chapter 4 investigates the use of a dual pulse preionization and energy addition system for ignition. An ultraviolet laser beam is used to preionize a volume of gas and an overlapped infrared

beam adds energy to the volume in a controlled fashion, resulting in a plasma with unique features, and potentially, a thermal ignition source. Chapter 5 discusses conclusions and areas for further study.

2 Development of a Solid Core Fiber Delivery System

The fundamental requirement of any laser ignition system is to ignite the gas mixture in the combustion chamber. When non-resonant breakdown is the ignition mechanism, two requirements must be met: 1) the delivered laser light must be of sufficient intensity to cause breakdown of the combustion gases, and 2) the beam must contain sufficient energy to ignite the mixture. From a practical standpoint, two additional requirements on the fiber delivery system must be met: 1) the fiber must operate with bends such that the laser can be placed in a reasonable position away from the engine, and 2) the fiber must operate in the presence of any vibration the engine may create. Design of a system to meet these requirements followed an empirical process. Rigorous mathematical descriptions of the optical response of solid core fibers to vibration and bending in an engine environment are not fully developed, and hence physical testing provided the most efficient pathway towards meeting design requirements. This chapter presents the process used to create a solid core fiber delivery system for engine ignition.

2.1 Fiber Beam Quality Testing

2.1.1 Fiber Selection

Fiber selection for the ignition system was guided mainly by previous work performed at CSU. The work by Hurand et al. [41] showed that use of fibers with large cladding diameters significantly lowers output M^2 when compared to a thinner cladding,

all other factors being equal. Figure 5 shows output beam profiles for a 200/330 μm and 200/745 μm core/clad fiber. The fiber with the thinner cladding diameter has a highly multimode output and high M^2 , while the thick clad has a much more single mode-like profile, with lower M^2 . It is thought this decrease in M^2 is the result of the thicker cladding reducing the influence of microbending at the core clad interface. Gloge [52] postulated that random bending is a main cause of mode coupling in multimode fibers. Further analysis [53] modeled a fiber as a thin elastic beam, resting on a surface with Gaussian distributed random irregularity. It was shown that adding a hard jacket to the outside of the fiber will absorb much of the irregularity, leading to less microbending of the fiber itself. Increasing the cladding diameter works on a similar principle. With this in mind, the 400/720 μm fiber used in [41] was selected as a candidate for the fiber delivery system. While the smaller core diameter fibers have better output beam quality, they are less able to handle the high energies required for laser ignition. Previous attempts at laser ignition have shown that 400 μm core fibers (with regular clad) are able to handle sufficient energy [50], but suffer from poor beam quality. The tests presented in this chapter show the thick clad fiber is able to provide output with sufficient energy and beam quality for spark formation.

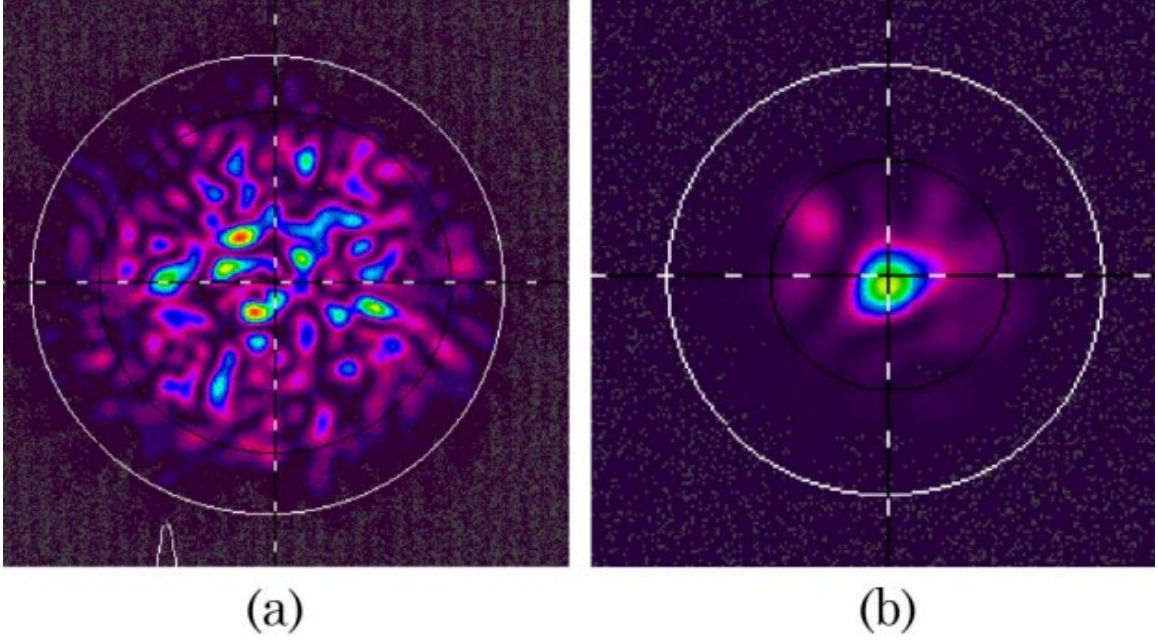


Figure 5 – Output beam profiles of (a) 200/330 μm fiber and (b) 200/745 μm fiber. The thick clad (200/745 μm) fiber ($M^2 = 2.8$) has much better beam quality than the thinner clad (200/330 μm) fiber ($M^2 = 11$). [41]

2.1.2 M^2 Measurement Methods

The ability to tightly focus the laser beam after passage through a fiber is highly dependent on the beam propagation factor, known as M^2 . With embedded Gaussian concept, one can consider the M^2 parameter as the ratio of beam widths between an actual beam and a perfect diffraction limited Gaussian beam [54]. M^2 is defined by the following equation [55];

$$M^2 = \frac{\theta\pi w_0}{\lambda} \quad (3)$$

where θ is the half angle (far-field) beam divergence, w_0 is the beam radius at the beam waist, and λ is the wavelength. A perfect Gaussian beam has $M^2 = 1$, while real beams can only have values greater than one. Therefore, the tightest a real beam can be focused by a lens is equal to the Gaussian beam waist multiplied by its M^2 factor. For the purpose

of tightly focusing beams to create breakdown, it is desirable to have M^2 as close to one as possible. For all tests performed in this chapter, M^2 at the fiber output was measured in one of two ways. For a quick measurement, we approximate equation 3 as:

$$M^2 \approx \frac{aw_z\pi}{z\lambda} \quad (4)$$

where a is the fiber core radius, and w_z is the beam radius at a distance z from the output face of the fiber. This approximation assumes the beam has a waist when it leaves the fiber and expands over a distance z . The advantage of using this approximation is that only one beam diameter measurement is required. For more accurate measurements, the change in beam diameter must be measured at several points along the beam's propagation direction. The fiber output must be collimated and then refocused by a lens, and the beam radius measured at several points in the vicinity of the waist. The resulting plot of radius versus position will be parabolic in shape, and the following equation can be fit to the data:

$$w^2 = w_0^2 + M^4 \times \left(\frac{\lambda}{\pi w_0}\right)^2 (z - z_0)^2 \quad (5)$$

where w is the beam radius at position z , and w_0 is the waist radius located at z_0 . This is known as the curve fit method; a rigorous description of the measurement was written by Siegman [56].

2.1.3 Fiber Test Setup

While previous work has shown the potential of the 400/720 core fiber, additional tests were required to determine performance under engine like configurations. The work performed in [41] examined this fiber in only a two meter length held in a straight configuration with a 633 nm laser. A typical engine setup will require one or more

bends, a longer fiber, and 1064 nm light. Therefore, more applicable tests were needed to ensure sufficient fiber output beam quality. The test setup closely followed that described in [41] shown in Figure 6. A 1064 nm CW diode laser (Lightwave Electronics Model 142, $M^2 = 1.2$) was used as the light source. The beam was steered with two mirrors into a half wave plate and polarizer variable attenuator, expanded in a telescope, and focused down into the fiber. The fiber tip was located at the beam waist and held in place with double sided tape. The target spot size of the beam at the location of the fiber tip was $w/a = 0.65$, where w is the beam radius and a is the fiber core radius. For low launch angle ($\theta \leq 0.01$ rad), output beam quality is largely unchanged for $0.2 \leq w/a \leq 0.8$ [41]. A value towards the upper end of this range is desirable to decrease the irradiance on the fiber tip when using high power lasers. For 400 μm core fibers, the nominal input spot size is 260 μm . At the output end, the beam exiting the fiber was collimated with a lens, steered with two mirrors and then focused with a final lens. The profile of the focused beam was used to measure M^2 by the curve fit method. Beam diameters were measured using a beam profiler (Point Grey Scorpion CCD camera and Spiricon LBA profiling software). The fibers tested were 4 m in length, and held above the table at beam height. Several possible fiber configurations were tested for their transmission efficiency and output beam quality. Tested configurations are shown in Figure 7.

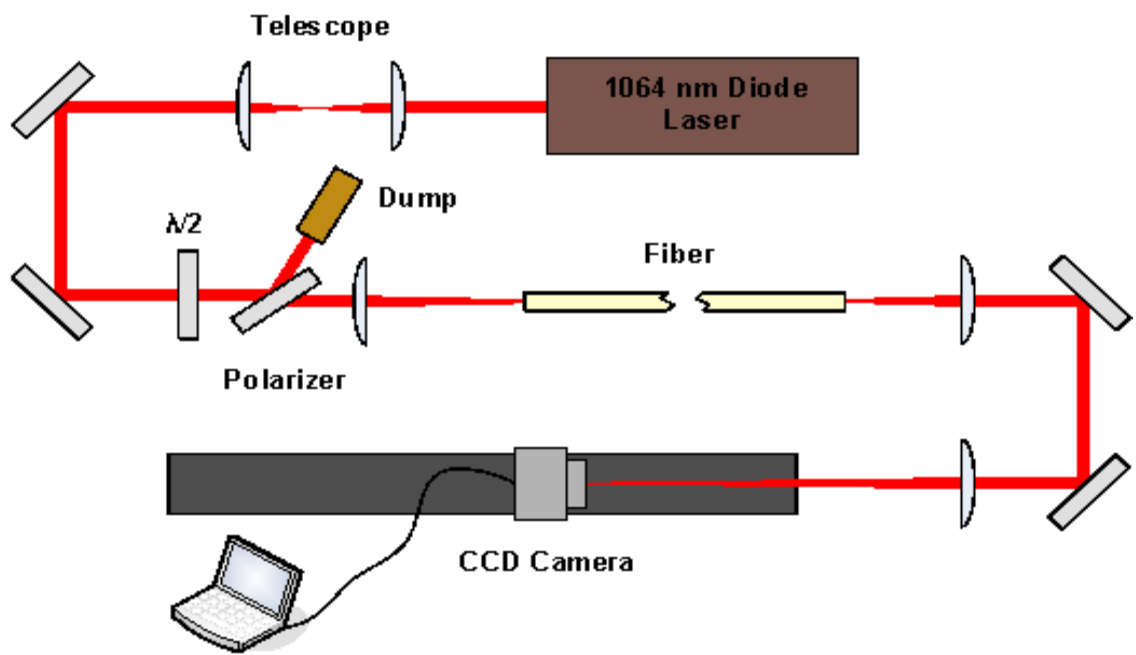


Figure 6 – Test setup for fiber M^2 measurements.

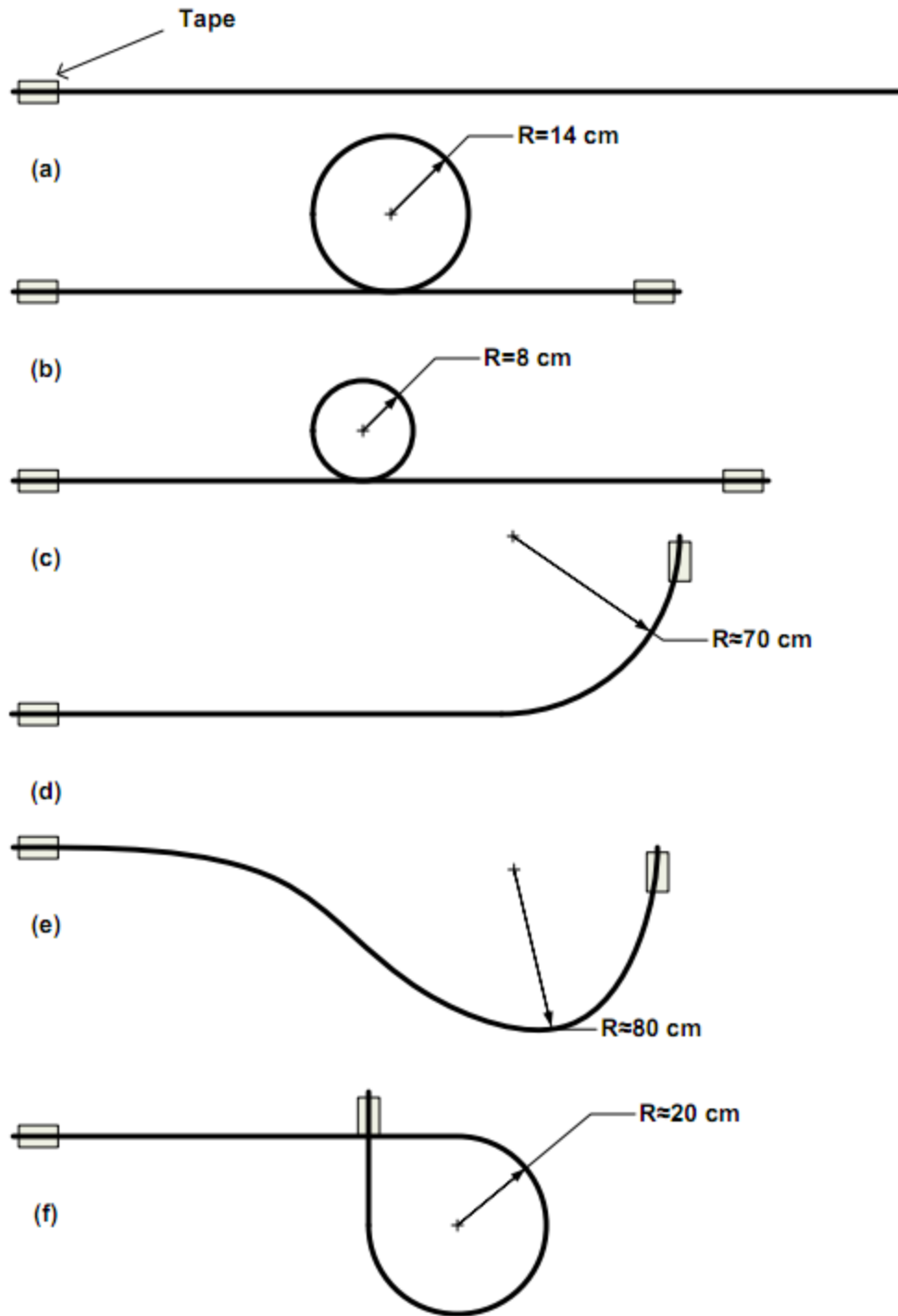


Figure 7 – Fiber configurations tested. Fiber was 4 m in length for each case and held in a horizontal plane. (a) – straight. (b) – 14 cm loop. (c) – 8 cm loop. (d) – 70 cm 90 degree bend. (e) – “S” shape. (f) – 20 cm 270 degree bend.

2.1.4 Fiber Beam Quality Results

M^2 values and transmission efficiencies for measured cases are shown in Table 2. The best fiber output is for a straight configuration, and while the goal of this test was to determine the behavior of this fiber in other configurations, it was included for comparison. The loops show a slight increase in M^2 , with the tighter loop producing slightly better beam quality than the larger loop. Bending in fibers has been well studied [57], and generally tight bends (down to a certain radius) decrease M^2 and decrease transmission. This is due to the radius effectively changing the NA of the fiber near the bend, allowing higher order modes near the critical angle to exit the fiber core. The loss of these high order modes results in a better beam quality, but since they contain part of the beam's energy, transmission will decrease. Configurations (b) and (c) are in good agreement with this theory. The 90 degree bend showed relatively poor performance, and is thought to be due to difficulties holding the fiber in that shape. The fiber had to be mechanically held in the 90 degree bend, resulting in considerable stress. Stress causes small deformations at the core-cladding interface which results in mode coupling and a degradation of beam quality [58]. Therefore, it is beneficial to allow the fiber to relax into its least stressed state, as evidenced by the substantial decrease in M^2 of configuration (e) relative to (d).

The presented results show a significant improvement in beam quality as compared to previous studies investigating the use of step index fibers for laser ignition. The use of 1064 nm radiation, as opposed to 633 nm [41] resulted in a large reduction in M^2 . In addition, it was shown that the fiber can be placed in positions other than straight

without a significant penalty in beam quality. This finding greatly increases their potential for use in a practical laser ignition system.

Table 2 - Output M^2 and transmission for 4 m fibers in different configurations.

Configuration	M^2	Transmission (%)
(a)	2.2	92
(b)	3.1	85
(c)	2.9	82
(d)	7.6	84
(e)	3.4	91
(f)	2.8	Not Measured

2.2 Fiber Power Testing

2.2.1 Long Pulse

Recent work at CSU using the fiber described in Section 2.1.1 has shown it is capable of delivering sufficient intensity to produce sparks in atmospheric air [59]. In those tests, 9.5 ns pulses were delivered from the laser into the fiber with launch conditions similar to those in the low power beam quality tests described above. A 100% spark rate was achieved in atmospheric pressure air with input pulse energy of 3.5 mJ, well below their reported damage threshold of 6-8 mJ. Lean ignition, however, requires 10 – 20 mJ of energy, which is above the damage threshold for this fiber. In order to transmit the required energy, the pulse duration was lengthened such that the peak power would remain approximately constant with increased energy. The longer pulses were generated by delaying the Q-switch firing so that the laser produced a 50 ns duration pulse. The reported damage threshold for this duration is 25 mJ, which would allow sufficient power for lean ignition. While the reported work allows for spark formation in

atmospheric air, the fiber was held in a low stress straight configuration, which according to Section 2.1.4 produces the best M^2 . Allowing for bends along the length of the fiber could easily double the M^2 , resulting in a four-fold increase in the energy required to create a similar intensity at the focal point. Fortunately, the electron avalanche process favors higher pressures. For typical engine conditions (>3 bar), the intensity required to spark decreases, allowing for a slightly degraded beam quality. Results from the CSU study shows this dependence for the two pulse durations considered, are presented in Figure 8.

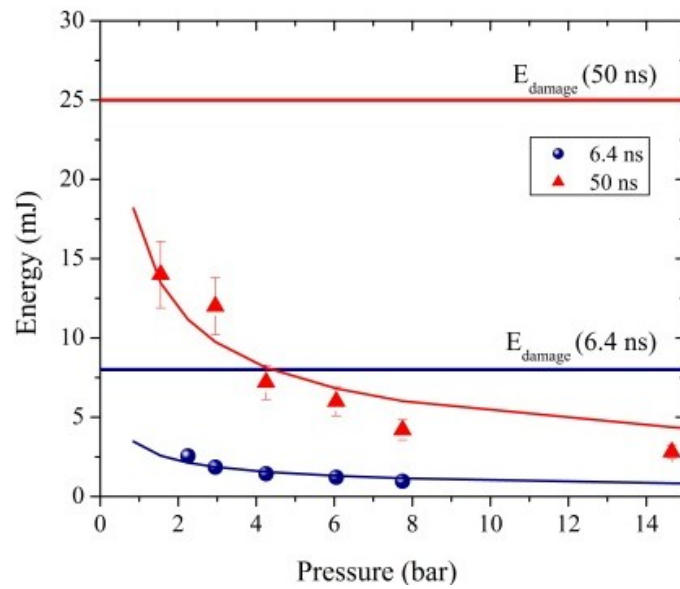


Figure 8 – Energy required to form sparks in air at different pressures and pulse durations [59]. Fitted lines represent $p^{-0.5}$ dependence.

2.2.2 Stimulated Brillouin Scattering

In order to further characterize the fiber performance under high power, transmission tests were conducted using both 30 and 50 ns pulse durations from the same

laser (Continuum model PR II 8000). Results are shown below in Figure 9. Figure 9a shows the transmission for different input energies for a 30 ns pulse width. The results show a slow decline in transmission with increasing input energy, until the fiber finally breaks near 25 mJ, which is attributed to Stimulated Brillouin Scattering (SBS). SBS is caused by a phenomenon known as electrostriction [60], in which the large electric field produced by the laser causes a strain in the glass of the fiber, changing its density. Due to the wave nature of laser light, the oscillating electric field generates an acoustic wave by rapidly changing the density of the medium in which it is traveling. The density change results in a wave of varying refractive index within the fiber core which acts as a Bragg reflector and sends a red shifted stokes wave in the direction opposite the pump light. For silica fibers, this shift is on the order of 1- 20 GHz [61]. Brillouin scattering is a non-linear process, meaning its efficiency is dependent on the pump power. At low powers, the process is spontaneous, but at higher powers becomes stimulated, where the amount of backscattered light can rapidly increase. The onset of a backwards traveling SBS is caused by acoustic noise in the fiber, and as such there is large uncertainty in measured SBS thresholds, e.g., $\pm 20\%$ in the case of [62]. Their results showed the SBS threshold has significant dependence on pulse duration, where shorter pulse durations have a higher threshold. For example, a 300 μm core fiber had a SBS threshold near 45 kW with a ≈ 25 ns pulse pump beam, which lowered to 35 kW when the pulse duration was increased to ≈ 55 ns.

The slow decline in transmission show in Figure 9a can be attributed to SBS. As the pump power is increased, more of the light gets scattered in the fiber and reflected back towards the input face. As far as energy available for ignition is concerned, this

energy is lost. Figure 9b shows results from the same test conducted at 50 ns pulse duration. Up to approximately 16 mJ input energy, the trend is similar to the 30 ns case, but as the energy is increased further, the transmission curve begins to increase. At first glance, this is not consistent with an SBS process. To investigate, an experiment was conducted similar to that of [62], shown in Figure 10. A beam splitter was placed shortly after the lens that focused the beam into the fiber. The small portion of the incoming beam was reflected into a photodiode. In the same way, a portion of any light exiting the fiber in the opposite direction would be reflected into a CCD camera. The angle of the fiber was slightly offset so that the reflection off the fiber's input face was not seen by the CCD camera. The photodiode was placed originally to measure the pulse duration of the input beam. However, this detector picked up an interesting result that serves to explain the shape of the curve in Figure 9b. When the CCD detected either a weak SBS beam or no beam at all, the photodiode displayed the expected Gaussian-shaped laser pulse. However, as the input power was increased, the SBS became more prevalent and in addition to the laser pulse, the photodiode detected a second and occasionally a third pulse, approximately 75 ns after the main laser pulse. The magnitude of the extra pulse was highly erratic, but generally increased as the input power, and consequently the SBS intensity increased. When the input tip of the fiber was blocked, these extra pulses disappeared completely. There was strong correlation between the intensity of the SBS beam and the presence of the extra pulses, and in some cases, the extra pulses were greater in magnitude than the original laser pulse. Due to the location of the photodiode, the pulse magnitude, and disappearance when the fiber tip was blocked, it was concluded

that the extra pulses could not have originated in the fiber, and must have come from the laser.

The SBS beam was able to travel back through the optical path, amplify itself in the laser cavity, and return as a second pulse. This explains the increased transmission for high pulse energy in Figure 9b. Since measuring the input energy required blocking the fiber tip, only the main laser pulse was measured. However, measuring the power at the output of the fiber allowed the SBS beam to amplify itself in the cavity, sending significantly more energy through the fiber than what was originally thought. In agreement with [62], the SBS and consequently the presence of the extra laser pulse declined with decreased pulse duration, as shown in Table 3. While it is interesting to note that extra energy can be sent through the fiber without damage by sending multiple closely spaced pulses, concerns about the health of the laser operating in such conditions necessitated the attenuation of the SBS beam. The only method to accomplish this would be to use a Faraday Isolator, but due to cost and schedule restrictions, obtaining one was not feasible. Therefore, the longest pulse duration allowable for this experiment was limited to 30 ns, such that presence of the extra pulses was minimized. Fortunately, as shown in Figure 9a, this still allowed enough energy for lean ignition.

Table 3 - Onset of SBS and extra laser pulses with pulse duration. Onset of SBS defined by detection on the CCD camera for every firing of the laser. Probability of extra pulse indicates the approximate rate of appearance of the extra pulse.

Pulse Duration (ns)	Onset of SBS (mJ)	Probability of Extra Pulse
37	13.2	100%
35	13.9	~90%
32	15.1	~50%
30	16.6	~1%

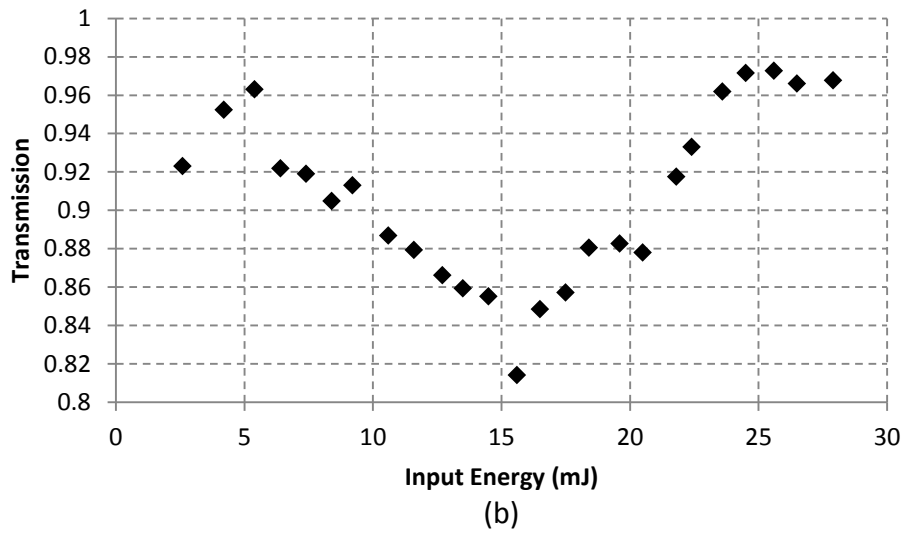
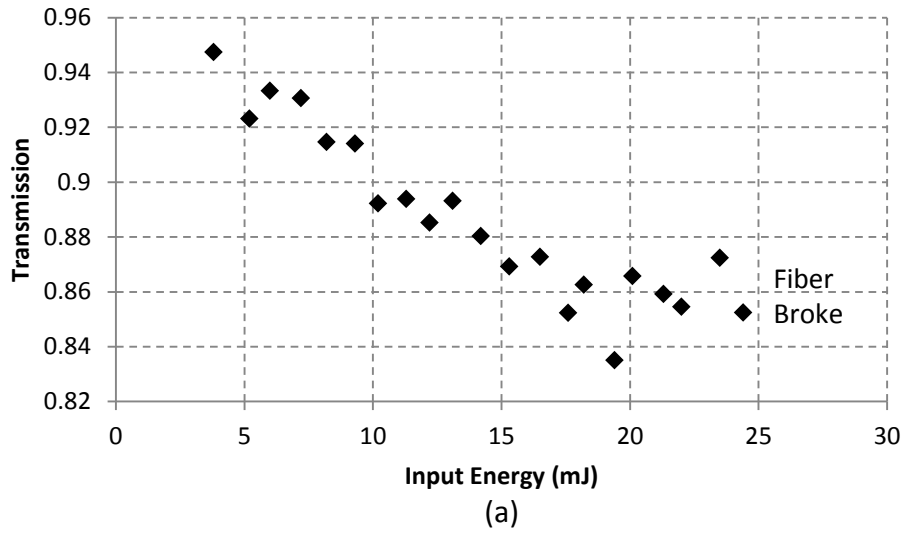


Figure 9 – Transmission efficiency versus input energy through straight, 4m fiber for (a) 30 ns pulses and (b) 50 ns pulses. The increase in efficiency near 16 mJ input energy is the result of SBS traveling back to the laser cavity, amplifying, and returning through the fiber. This resulted in incorrect transmission measurements.

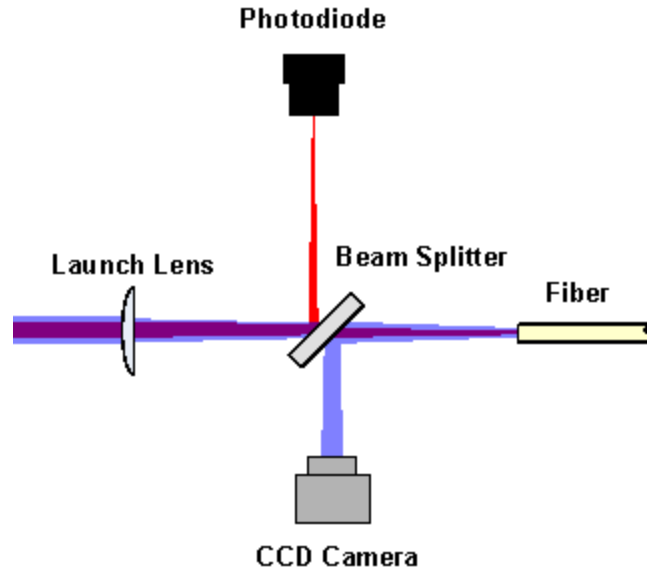


Figure 10 – SBS investigation experiment. Red lines indicate laser beam coming from the laser, while transparent blue lines originated from the fiber.

2.2.3 Longevity Testing

In order for a fiber delivered laser ignition system to be viable, it must be capable of running for thousands of hours continuously. Tests of such length were not feasible in this work, but some short duration testing was needed to make sure the fiber could withstand initial on-engine testing. Two 50 hour tests were conducted to ensure the fiber could continuously transmit the power required for ignition. The first test was with a straight, stationary fiber sitting on the optical bench. For the second test, the same fiber was placed in a 90 degree bend with ≈ 50 cm radius, with the output end held on a shaker table vibrating at 20 Hz with 3 mm total amplitude. This was to simulate more engine-like conditions. Both tests used the same input conditions shown in Figure 6, transmitting 30 ns, 15 mJ pulses from the Continuum laser. The same fiber was used for both tests, accumulating 100 hours total of high power delivery. A small portion of the output power was directed to an energy meter via a beam splitter and was monitored for

the duration of the test. The input power was not continuously monitored, but periodic checks were performed.

The static longevity test results are shown in Figure 11. The beam quality exiting the fiber at the beginning of the test was $M^2 = 3.9$ (NA method), and the transmission was approximately 95 %. During the test the laser shut itself off near hour 6 and had to be restarted, and the energy meter was bumped near hour 18. This offset all data after this point down by approximately 70 μJ as not all of the beam was captured by the sensor. To compensate, the data shown in Figure 11 was increased by 70 μJ after hour 18 to match the time immediately before it. After the test, the output beam quality degraded to $M^2 = 9.4$ and the transmission dropped to approximately 91%. However, small adjustment of the input alignment stage resulting in the fiber tip moving 0.25 mm returned the output quality and transmission to their initial values. These results indicate the fiber showed no decrease in performance throughout the 50 hours, but there was drifting of the alignment between the fiber tip and the input beam. The vibrating test yielded similar results. The initial beam quality and transmission were $M^2 = 5.7$ and approximately 91%, respectively. The input laser power began dropping from the start of the test, dropping to 12 mJ near hour 9, before it was reset to 15 mJ. Near hour 45, the laser again turned itself off and had to be restart. Much like the static test, there was a slight drop off in output power during the last 5 hours. The measured beam quality and transmission at the end of the test was $M^2 = 9.4$ and 85%. Again, a slight adjustment of the input alignment returned the fiber to its original conditions, and results show that the fiber is still able to handle sufficient power in the presence of vibration. The input alignment will need

additional investigation to determine why there is a drift, but the fiber and laser remain in alignment long enough for the short term engine testing presented here.

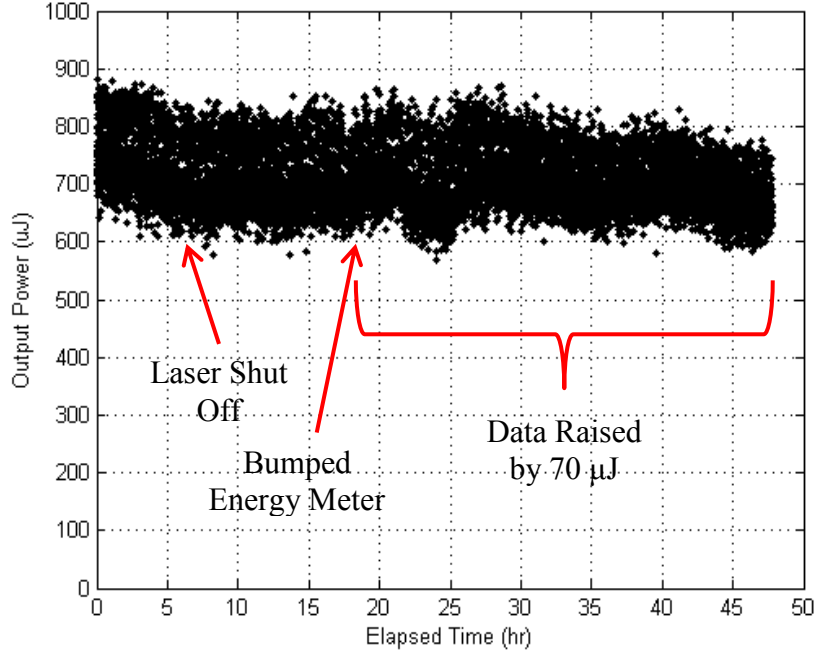


Figure 11 – 50 hour static fiber test. Ordinate axis represents a fraction of the total output power.

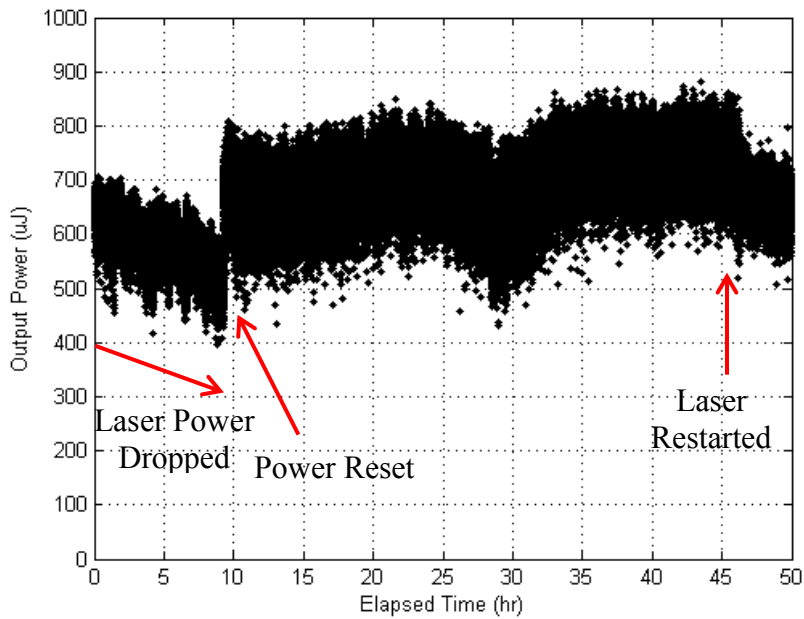


Figure 12 – 50 hour vibrating fiber test. Ordinate axis represents a fraction of the total output power.

2.3 Vibration Testing

While the test in Section 2.2 showed no damage was done to the fiber delivering high power pulses while in the presence of vibration, the beam quality while vibrating has yet to be analyzed. Such a test was performed by Mullet et al. [50], in which a 400 μm fiber with smaller clad/core ratio was subject to engine vibration. The vibration caused an increase in output beam divergence, which was found to be maximized at a certain frequency. The fiber delivery system will have a natural frequency in which displacement caused by vibration is maximized. For the purposes of pulsed laser propagation, a fiber in the presence of engine vibration can be thought of as being static, as it takes ≈ 20 ns for a low order mode to travel a 4 m length of fiber. At typical engine speeds, the physical distance traveled by a fiber mounted on a vibrating engine in 20 ns is negligible. Therefore, one must consider the motion of the fiber and if any configurations along its path of movement cause stress at the core-clad interface. If the fiber is placed in a stressful position, mode coupling will increase the output beam divergence and worsen the beam quality. This section investigates the effects of vibration on the output beam quality for the selected 400/720 μm fiber.

2.3.1 CW Vibration Tests

Initial vibration tests were performed using a CW laser at 1064 nm (Lightwave 142). To simulate an engine environment at various operating conditions, a benchtop shaker table (Crowson ED-3) was employed and controlled by computer. The table was capable of operating between 5 and 2000 Hz and has a maximum amplitude of 6.3 mm. By placing the fiber's output face on the shaker table, engine conditions could be

mimicked for any frequency and amplitude within the shaker's range of motion. Measurement of beam quality was performed by the NA method, using a CCD camera to image the fiber output. While ideally the camera and the fiber output would remain fixed to each other, concerns about the camera's ability to handle vibration prompted it to be fixed to the optical table. The beam therefore moved relative to the camera, which required the exposure time be shortened to prevent blurring. While this was effective, it did not remove all blurring so the M^2 measurements presented are most likely larger than reality. Images were captured at the same rate as the frequency of vibration or slightly offset, in order to image the beam at constant or various positions along its motion.

In order to attach the fiber to the shaker table, a SMA connector was epoxied to the output end. The epoxy has a 1:1 wet/cured volume ratio, in order to minimize any stress that may be added to the fiber by the epoxy hardening. Despite this, it is impossible to eliminate all stress when adding a connector to the fiber. Before any vibration testing was done, the connectorized fiber was held straight (see Figure 7a) and a M^2 curve fit measurement was made. The connector increased the M^2 from 2.2 to 4.4, a significant increase. For these tests, only the straight configuration was considered, and the vibration table was set to shake at 25 Hz with ≈ 3 mm total amplitude, simulating a single cylinder engine at 1500 rpm. This level of vibration had a large effect on beam quality, increasing the M^2 to $\approx 8-10$. Several attempts to hold the fiber fixed in various positions did not result in better performance. Since there is no mechanism to dissipate the fibers mechanical energy, fixing the fiber merely creates points of high stress as it vibrates. Some method of damping was clearly required.

As was shown, holding the fiber fixed using either epoxy or other methods creates stress in the fiber and degrades the beam quality. Therefore, viscous damping was proposed as a method to dissipate the energy of vibration without rigidly attaching to the fiber. To test this, an oil bath was constructed in which to immerse the fiber; the setup is shown in Figure 13. The oil trough required that the fiber sag in the middle in order to be fully submerged, which increased stress near the end points, increasing the static M^2 to ≈ 5.4 . While this is not an ideal position for fiber delivery, it allows observations in the difference between vibrating with and without oil. Beam profiles for the various conditions investigated here are shown in Figure 14. Vibrating the fiber in the trough with no oil resulted in an M^2 of ≈ 9.2 , a 70% increase, while adding the oil dropped the M^2 to ≈ 6.5 , only a 20% increase. The addition of a viscous damping medium appeared to suppress the vibration and resulted in a better output beam quality.



Figure 13 – Oil bath and CW vibration test setup.

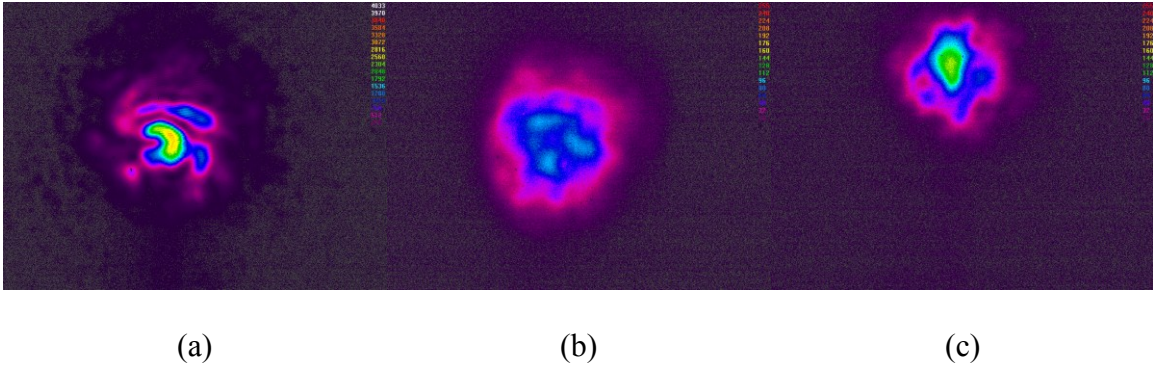


Figure 14 – Beam profiles for different tested conditions. (a) – Fiber resting in trough ($M^2 = 5.4$). (b) – Fiber vibrating without oil ($M^2 = 9.2$). (c) – Fiber vibrating with oil damping ($M^2 = 6.5$).

2.3.2 Pulsed Vibration Tests

Vibration tests with damping oil with high power laser pulses were performed and are presented in Appendix 1. For the purposes of the engine test presented in Chapter 3, it was found that no damping was needed by placing the fiber in certain configurations, found experimentally and presented here. Four configurations were considered, pictures of each are shown in Figures 15-18, with the fibers highlighted in red. While sparking in a straight configuration while vibrating with no form of damping was not possible, putting bends in the fiber significantly reduced the extent of the fiber's motion. Bending allowed much of the energy to be placed in a torsional mode of vibration, resulting in much less motion along the fibers length. In some cases, taping the fiber to the stands on which they sat was required to coax the energy into these torsional modes. This allowed 100% sparking for all configurations studied. Configurations (a)-(c) were within the plane of the table, while configuration (d) was in three dimensions, more closely mimicking what would be required for the engine test of Chapter 3. Vibration for cases

(a)-(c) was at 20 Hz with 3 mm total amplitude, and sparking was in 6.8 bar (100 psi). Case (d) could not use the shaker table due to the position of the output optics.

Required energy for 100% sparking as well as transmission measurements are shown in Table 4. These tests show that reliable ignition within an engine should certainly be possible. Since the vibration amplitude was kept at 3 mm and there was only small amount of motion in directions normal to the fiber axis, alignment of the output beam with the focusing lens was well maintained. However, switching between configurations resulted in gross misalignment of the beam and lens. For example, moving the fiber from a straight configuration to configuration (a) moved the output beam 3 mm from its properly aligned position. This implies an optical spark plug must incorporate some form of adjustment in order to align the beam with the focusing lens, and it must be aligned in the configuration used on the engine. For each configuration presented here, the beam had to be realigned before any sparking could happen.

Table 4 - Input energy for 100% spark and transmission for various configurations. Transmission could not be measured for (d) because of the position of the fiber output.

Configuration	Input Energy (mJ)	Transmission (%)
(a)	5.3	86
(b)	5.9	75
(c)	6.6	83
(d)	5.0	NA

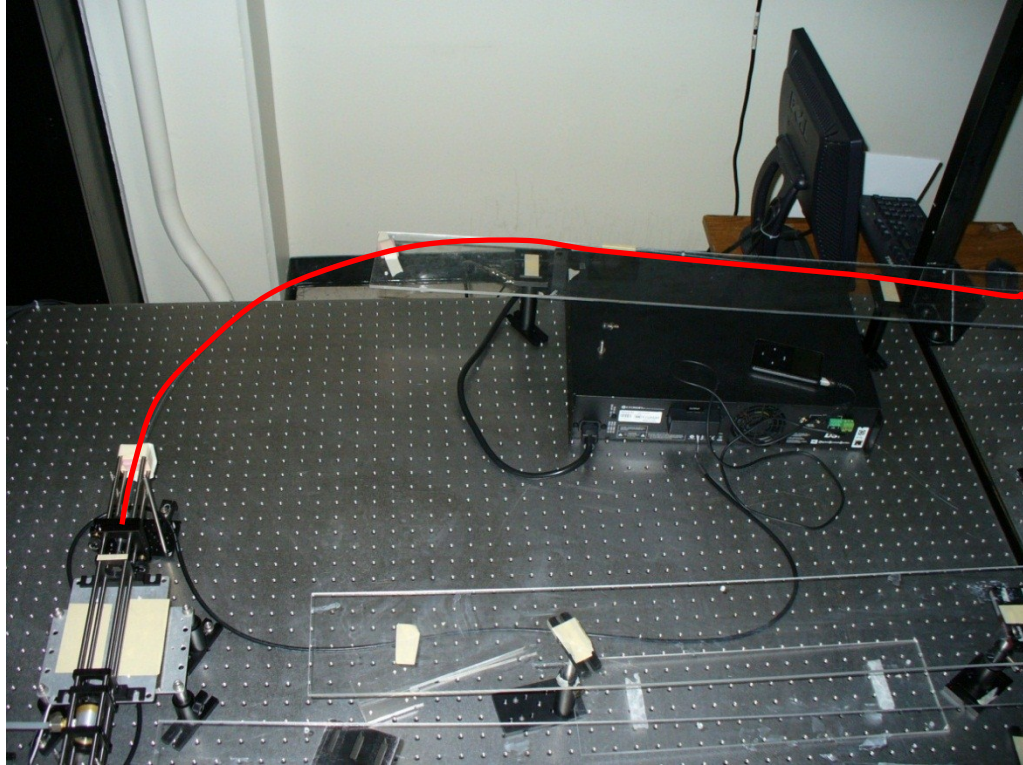


Figure 15 – Configuration (a), 90 degree bend. Fiber highlighted in red. ≈ 50 cm radius of curvature.

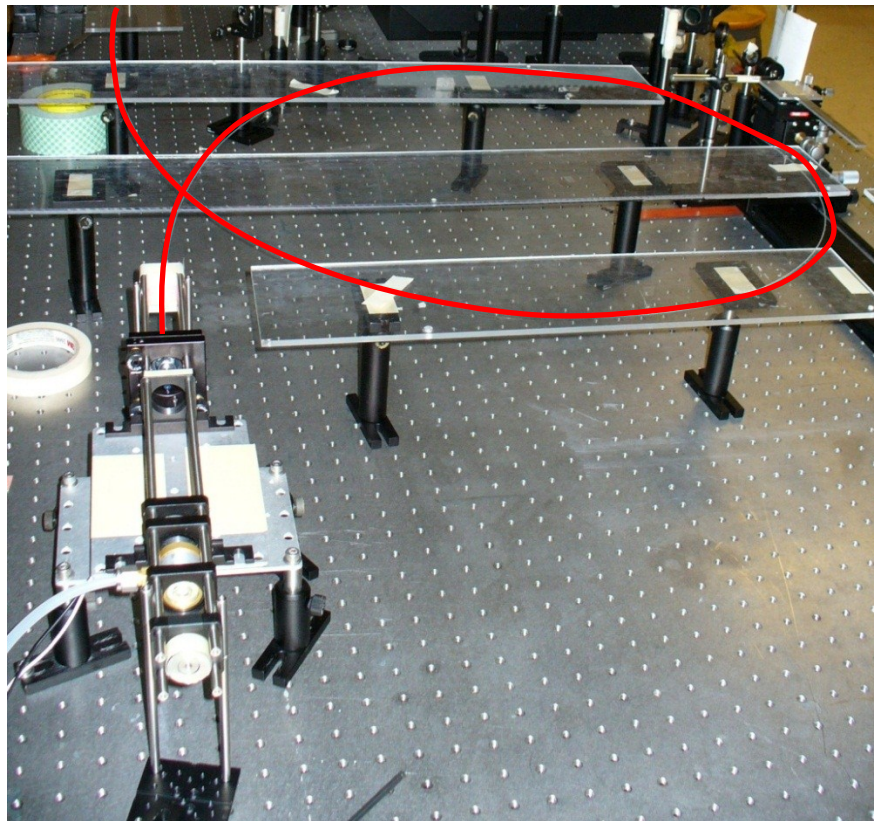


Figure 16 – Configuration (b), 360 degree loop. Fiber highlighted in red. ≈ 60 cm diameter.



Figure 17 – Configuration (c), “3” shape. Fiber highlighted in red. Final bend ≈ 40 cm radius of curvature.

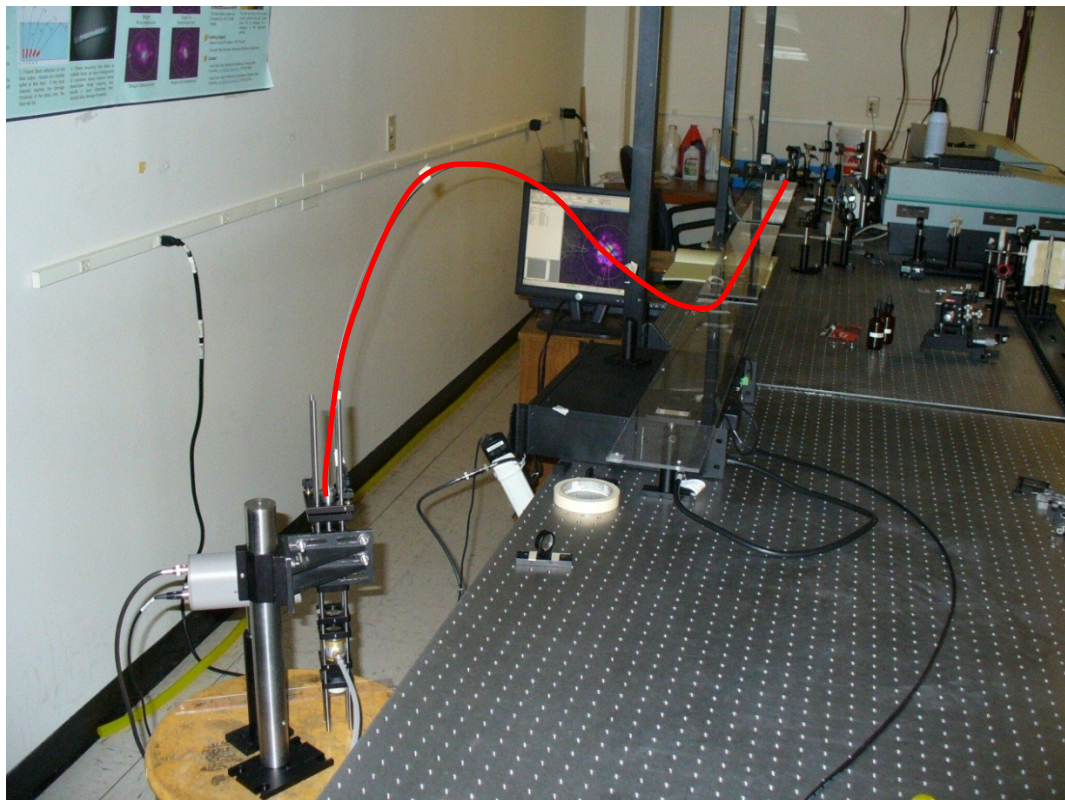


Figure 18 – Configuration (d), 3d “3” shape. Fiber highlighted in red. Fiber raises ≈ 40 cm from output tip and the curved section is ≈ 120 cm long.

2.4 Engine Test Preparation

2.4.1 Fiber Configuration

In preparation for the engine test presented in Chapter 3, an offshoot of configuration (d) (Figure 18) was constructed for testing. The engine required that the fiber output point straight down, and so a frame was constructed to hold the fiber in a gentle bend that would allow proper positioning. The vibration from the engine was expected to be minimal, so no major vibration damping system would be required. In order to ensure that what vibration did come from the engine was not efficiently transferred to the fiber, the frame was held on the optical bench and cantilevered forward, so that no part of the frame came in contact with the engine. A picture of the final setup can be seen in Figure 24 in Chapter 3. The relative placement of the laser and engine required a shorter fiber than previously tested, 2.85 m in length. The measured beam quality by the NA method was $M^2 \approx 5.1$ in this configuration, which is sufficient for spark formation.

2.4.2 Optical Spark Plug Design

The main preparation needed for an engine test was the design and construction of an optical spark plug. For all tests performed thus far, the beam was allowed to expand from the fiber tip into a collimating lens, which would collimate the beam at approximately a 5 mm diameter. This beam was then tightly focused by a 10 mm Gradium lens. The collimating lens had a focal length of 175 mm, making the entire system about 250 mm in length. For a practical system this is longer than desired. Ideally, a laser plug would be close in size to a typical electric spark plug for easier

engine integration. To shorten the total length, a negative lens was added to increase the divergence of the beam exiting the fiber in order to achieve the collimated beam size in a shorter distance. An ABCD matrix formulation was used to approximate what lenses and path lengths would be required, and to visualize the system. The initial beam size and divergence out of the fiber was set from M^2 measurements and the beam was propagated using matrices for the negative lens, collimating lens, focusing lens, and window.

After considering several different configurations, the beam path shown in Figure 19 was chosen. The beam first passed through a diverging lens of focal length $f = -25$ mm, followed by the collimating lens $f = 50$ mm, and was focused down by the Gradium lens, $f = 10$ mm. Immediately after the focusing lens, the beam passed through a 3 mm thick sapphire window which would provide optical access to the combustion chamber. The total distance from fiber tip to spark was ≈ 135 mm, significantly shorter than without the negative lens. The total length could be shortened even further by placing the negative lens closer to the fiber output, but for the purposes of this test, it was desirable to have a slightly larger optical plug. The additional size allowed for ease of usability in a laboratory setting, giving visual access, simplifying assembly, disassembly, and packaging, as well as allowing for more adjustability. Based on the matrix model, lenses were purchased and setup on the optical bench to test the accuracy and determine their exact positions along the beam path for optimal spark formation. Table 5 compares calculated with measured values. The model approximated the distances between lenses with good agreement.

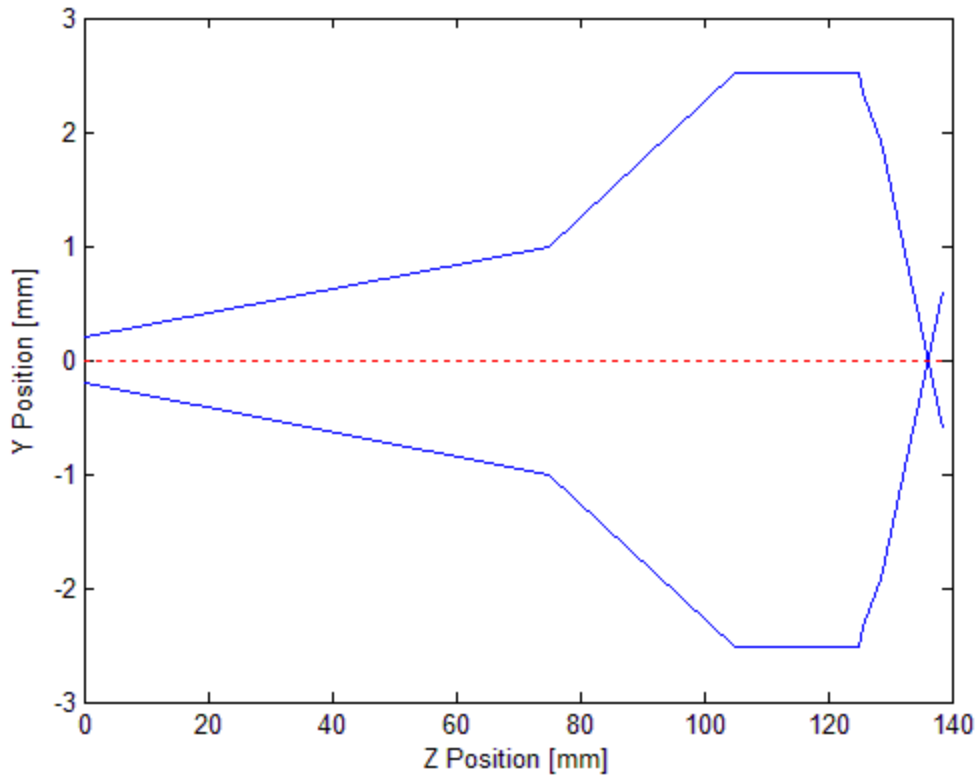


Figure 19 – Beam path through output optics using ABCD approximation. The area within the blue lines represents the beam. The y axis has been exaggerated for clarity. The red dashed line is the beam axis. Optical train is as follows: fiber output at $z = 0$, negative lens at $z = 75$ mm, collimating lens at $z = 105$ mm, focusing lens at $z = 125$ mm, window at $z = 130$ mm.

Table 5 - Comparison of measured values and ABCD approximation pertinent to spark plug design.

Parameter	ABCD Formulation	Measured
Output Beam Quality	4.6	4.6
$L_{\text{fiber-neg lens}}$ (mm)	75	77
$L_{\text{neg lens-col lens}}$ (mm)	30	32
Collimated Diameter (mm)	4.5	4.7

Once optics had been selected, the optical spark plug was designed. A cutaway view of the CAD model is shown in Figure 20. The design intent for this spark plug was for laboratory testing, and as such it was designed with a large amount of adjustability. The negative lens could be moved to any location within the teal section of the plug, the collimating lens could move within the blue section, and the teal and blue sections could

move relative to each other. This allowed for maximum control over the beam size and could accommodate minor variations in beam quality. The entire plug could be quickly disassembled and reassembled using custom tools so changes could be made easily. The fiber was attached using a standard SMA connector to an adjustable plate (orange), allowing the angle of the fiber axis relative to the spark plug axis to be adjusted by set screws. As found previously, the configuration of the fiber affects the angle at which light will exit, and so this adjustability was required. Once properly positioned, the plate could be securely bolted to the plug so it would not drift during use. The blue end of the plug screwed into a 7/8" – 18 port in the cylinder, and was sealed using a copper gasket. Smaller copper gaskets sealed the interior of the plug from the combustion chamber around the 3 mm thick sapphire window. Previous work at CSU has proven the success of this sapphire window / gasket design [19,20,32,63]. Finally, slits were cut in the side of the teal section to provide visual access into the combustion chamber so successful sparking could be confirmed.

The spark plug was approximately 15 cm in length at its nominal position, but could shrink or grow based on desired lens position. Figure 21 gives an idea of the size, while Figure 22 shows the finished plug with all components exploded. Once assembled, the plug was tested using a pressure chamber. Based on manufacturers' specifications, the transmission through the plug was calculated to be 82.5%. Based on a conservative fiber transmission estimate of 84% (see Figure 9a in Section 2.2.2), the total transmission through the fiber delivery system should be $\approx 69\%$. A direct measurement yielded 71%, meaning the plug performed as expected. Therefore, using 30 ns pulses up to ≈ 25 mJ would yield a maximum 17.7 mJ pulse energy in the combustion chamber, within the 10-

20 mJ required for lean ignition. A bench top test in the engine configuration (see Figure 24 in Section 3.1.2) showed the system was capable of 100% sparking in a 6.8 bar (100 psi) environment with 15 mJ input energy. This test proved the system was suitable for on-engine use, which will be presented in the following chapter.

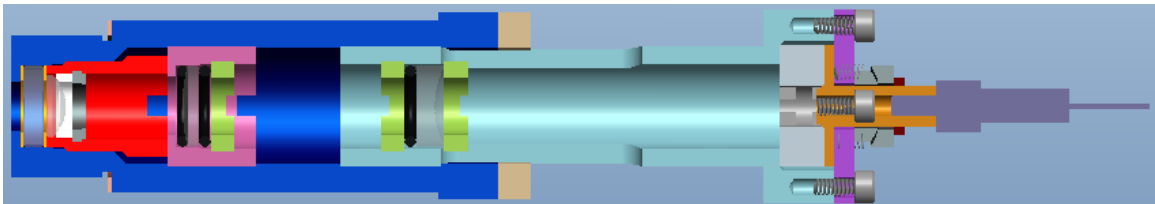


Figure 20 – Cutaway CAD model of the optical spark plug.



Figure 21 – Assembled optical spark plug.

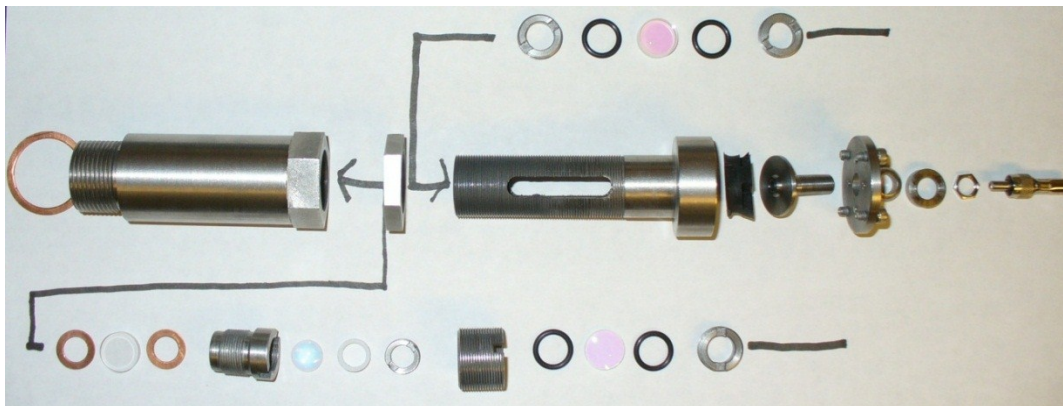


Figure 22 – Exploded view of optical spark plug.

3 Solid Core Fiber Delivered Laser Ignition Test

Despite an abundance of literature on laser ignition, very few tests have been performed using solid core fiber delivery. The tests performed thus far, [6,50] have been either unsuccessful in running the engine without misfire or did not extend to the lean conditions where laser ignition is intended to operate. Also, no studies have been done at various load conditions to see if the fiber delivered system is capable of running the engine during startup, idle, and full load. This chapter presents the results of a comprehensive engine test using the fiber delivery system described in Chapter 2. For comparison, the engine was run with both laser and electrical spark ignition to determine if laser ignition remains beneficial while using the fiber delivery system. While there were some difficulties, the system was able to successfully run the engine without misfire, and with higher efficiency than traditional spark ignition.

3.1 Experimental Setup

3.1.1 Engine

The engine used for this test was a single cylinder Waukesha Cooperative Fuel Research (CFR) engine. It was originally used to test gasoline octane rating, but has been converted to run on gaseous fuel. Figure 23 shows a cross section of the CFR, which has bore and stroke lengths of 82.6 mm and 114.3 mm respectively. Due to its original purpose, the compression ratio can be varied from 4:1 to 18:1, but was left at 14:1 for the duration of this test. The intake could be boosted up to 3 bar absolute pressure with

compressed dry air, which was controlled by a pneumatic valve. While air pressure was delivered by the buildings compressor, a manual gate valve was placed in the exhaust to obtain backpressure that would be present had a turbocharger been providing the boost. The fuel for this test was bottled methane, and was delivered via fuel injector through a coriolis flow meter for mass flow measurement. The air-fuel ratio was measured via an oxygen sensor in the exhaust. Proportional-integral-derivative (PID) control was used to maintain the desired ratio by adjusting the duty cycle of the fuel injector.

The electric motor attached to the engine was used for startup and motoring. When the engine was running, the motor generated electrical power which could be measured and returned to the grid, with 90% efficiency. This system maintained the engine at a nominal 950 rpm for all test conditions. Crank position was measured using an encoder with a resolution of 0.1 degrees, producing 3600 counts per revolution. In-cylinder pressure was measured with a pressure transducer (Kistler 6061b) and charge amplifier, which was recorded using a data acquisition system (Hi-Techniques). Exhaust gases were sent to a 5 gas analyzer (Rosemount) for emissions measurement. Relative concentrations of nitrous oxides (NO_x), carbon monoxide (CO), carbon dioxide (CO_2), oxygen (O_2) and total hydrocarbons (THC) were measured. The signals from all sensors were sent to a custom Labview program that further reduced the data, and allowed control of boost pressure, air fuel ratio, and ignition timing. The program displayed important operating parameters in real time such as pressure versus crank angle curves, fuel flow rate, current air-fuel ratio, mean effective pressures (MEP), etc. Test points were chosen in terms of net mean effective pressure (NMEP), which is determined from the pressure curves and is the difference between the indicated mean effective pressure

(IMEP) and pumping losses. As pumping losses vary with respect to back pressure, NMEP was chosen as a suitable metric for measuring engine performance.

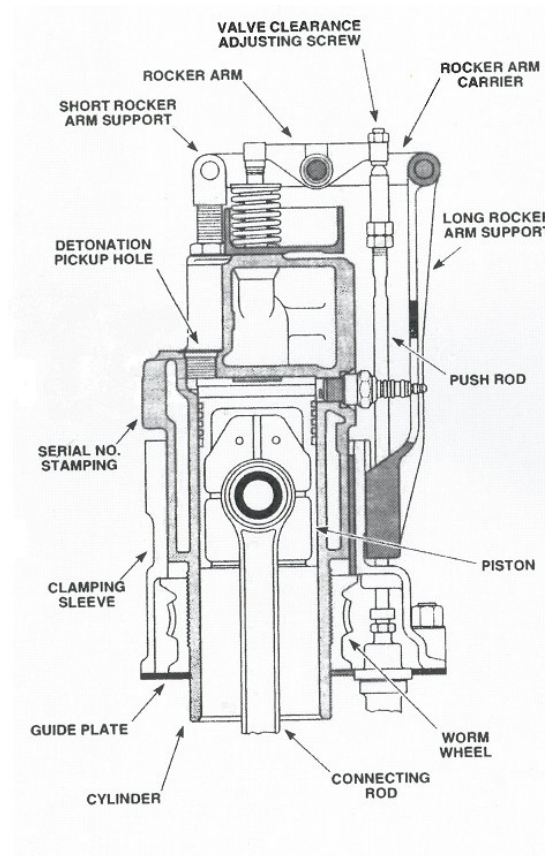


Figure 23 – CFR engine cross section. Both the laser and electric spark plugs were located in the detonation pickup hole, with the spark located 5mm from the top wall of the cylinder. The spark plug shown in this diagram was replaced with the pressure transducer.

3.1.2 Fiber and Laser

The overall test setup is shown in Figure 24. The laser and all optical components were placed on an optics table beside the engine. A frame was constructed and bolted to the table which supported the fiber in the configuration determined previously. Every attempt was made to ensure the fiber was placed in an identical position to that

determined in the lab. One major difference that could not be avoided was the position in which the fiber was aligned. Alignment of the fiber input was done with the fiber in a straight configuration in all previous lab tests. Due to space constraints near the engine, this was not possible so the fiber was aligned in a coiled configuration. While significant testing was not carried out, it is not believed this alignment scheme changed the fiber performance in any way. The optics were setup so that the beam input conditions were the same as all tests shown in Chapter 2, with a half wave plate and polarizer controlling the power entering the fiber.

The laser was the same as previously used for longer pulse durations, a Nd:YAG (Continuum model PR II 8000) operating at 1064 nm. Synchronization between the engine and the laser was handled by an inductive current clamp on the ignition cable. When running on laser ignition, the spark plug was removed and the cable was grounded to the case. The high voltage sent through the cable at the time of ignition was picked up by the current clamp and triggered a pulse delay generator (BNC model 555), which in turn triggered the laser flashlamp and Q-switch. The total time delay between the ignition signal and delivery of laser pulse corresponded to ≈ 2 degrees of crankshaft rotation, so the ignition timing for the laser spark was advanced accordingly. While it was determined in the lab that the pulse duration should be 30 ns (see Section 2.2.2), slight changes in the alignment of the optics decreased the threshold at which the SBS beam caused feedback in the laser. This necessitated the pulse duration be lowered further to approximately 25 ns. It was previously decided that for 30 ns pulse duration, a safe limit of 18 mJ input energy would be imposed until the system was running properly. As damage limits scale approximately as $\sqrt{\tau}$ where τ is the pulse duration [64], the new

limit was lowered to ≈ 16.5 mJ. To ensure the pulse duration stayed constant from day to day and that no SBS feedback was getting amplified in the laser, a photodiode was placed near the polarizer to monitor the rejected light.

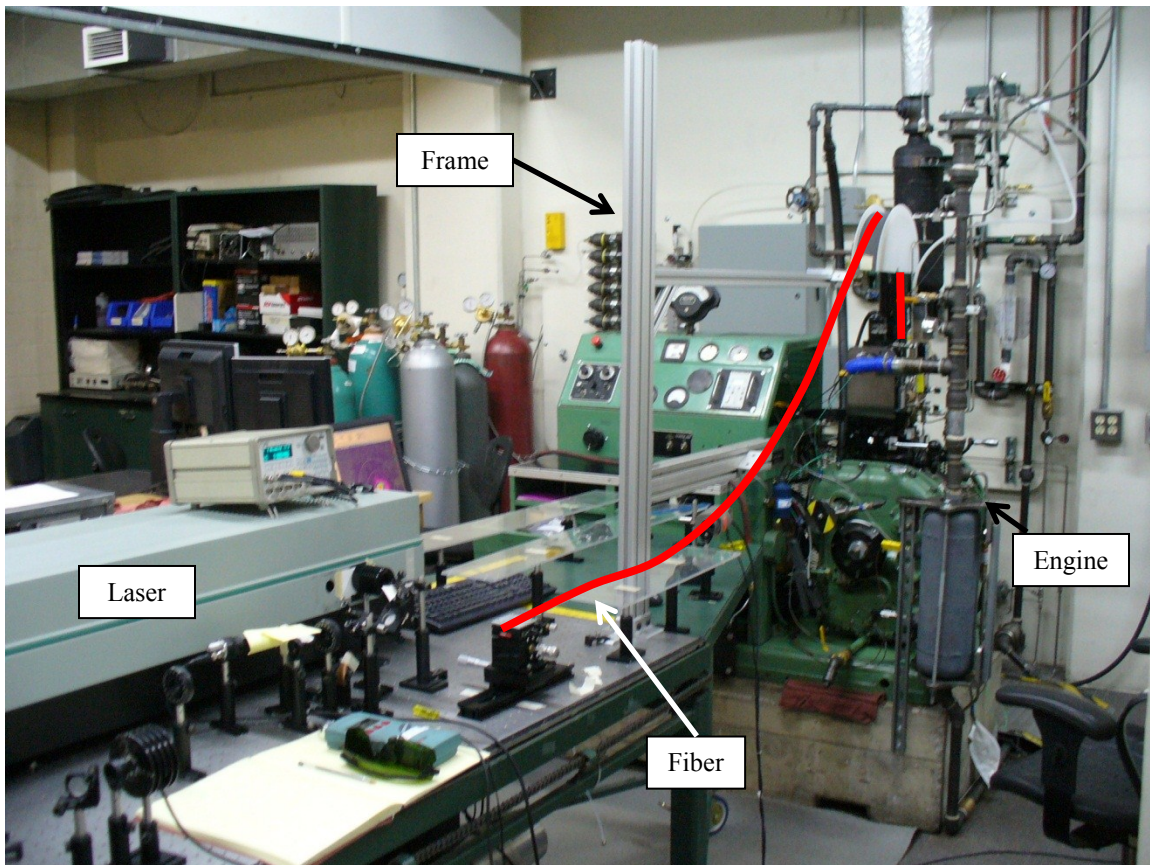


Figure 24 – CFR engine test setup. Fiber highlighted in red.

3.1.3 Test Methodology

The optical spark plug was placed in the detonation pickup hole (Figure 23) on the top of the cylinder instead of the designed spark plug location on the side. This modification was necessary due to limited space near the spark plug port which would have required a very sharp bend in the fiber. The pressure transducer was placed in the

original spark plug port. To ensure a fair comparison, an adapter was made to fit the electric spark plug in the detonation pickup hole. Swapping the optical for the electric plug resulted in a negligible change in clearance volume (0.34% decrease). The laser spark and electric spark were nominally at the same location, 5 mm from the upper wall of the combustion chamber. Tests of both ignition systems were performed at 6, 8, and 12 bar NMEP. While it would have been ideal to test at high NMEP levels in which laser ignition may be more beneficial (>15 bar), such conditions were not safe for the CFR engine. Tests performed at 6 and 8 bar were to ensure the laser ignition system could run at idle and minimal load conditions, where low pressures could possibly result in unreliable spark formation. For each NMEP level, the air fuel ratio was swept from low to high, always in the lean regime. The actual values varied for each level, with higher NMEP allowing leaner operation. The lean limit for each NMEP level was determined by coefficient of variation (COV) of NMEP greater than 10%. Timing was held constant through each test for all air-fuel ratios, and determined by the maximum brake torque (MBT) method. For each load, the air-fuel ratio was held constant and the timing that produced the highest NMEP was chosen as MBT timing. This sweep was performed only for the electric spark plug, and the same timing was used for the laser system. Tests were first performed using the electric spark plug and then the same data points were repeated with the laser system. Since the fiber delivery system was unable to spark in atmospheric air, the combustion chamber was pressurized for spark plug alignment. An adapter was made so house air could be fed in through the standard spark plug port to a pressure of 6.8 bar (100 psi) for alignment. Once aligned, the pressure was lowered until the system could no longer reliably spark. The lowest pressure allowing reliable sparking

was approximately 3.5 bar (50 psig), significantly lower than the minimum motored pressure of 9.6 bar at 23 degrees before top dead center (BTDC) and 6 bar NMEP.

3.2 Engine Test Results

Results are presented in terms of measured data or parameters calculated from measured data. For this test the directly measured values were in-cylinder pressure, crank position, output electrical power, fuel mass flow rate, air fuel ratio, intake manifold pressure, and emissions. From these, NMEP, coefficient of variation (COV) of NMEP, brake specific fuel efficiency, location of 10%, 50%, and 90% mass burn fraction as degrees after top dead center (ATDC), average peak pressure location, and COV of peak pressure location were calculated. All comparisons between ignition systems are made in terms of these parameters. Error bars were determined by the standard deviation of the value over 1000 engine cycles; the error was propagated from measured values for any calculated data. Some points do not include emissions data because the 5 gas analyzer was not available at the time of the test.

3.2.1 Cold Start

Laser ignition was able to reliably cold start and warm the engine at 101 kPa (absolute) manifold pressure. During motoring, a layer of oil buildup was observed on the sapphire window. If the engine was motored for a significant period of time (5-10 minutes) without fuel so that no combustion occurred, the oil buildup would become significant enough to inhibit spark formation. If the engine was given fuel before the oil buildup became too severe, the ensuing combustion would burn the oil and clean the

window. Upon completion of a given test point, inspection of the window showed no buildup or coating, although no test exceeded 3 hours in duration.

3.2.2 6 Bar NMEP

To achieve this load level, the intake manifold pressure was set to 101 kPa and the ignition timing was fixed at 23 degrees BTDC for both ignition systems. MBT ignition timing was not determined for this low load case. Due to the nature of the fiber delivered system, testing at this load level was primarily to ensure sparking could be reliably delivered under engine idle conditions where the cylinder pressure at ignition is at its minimum. Still, the system was able to reliably spark with nominal spark energy of 7 mJ. Due to an unexpected drop in laser power, one of the points had spark energy of only 3.8 mJ, and is marked in the plots. Average pressure traces (1000 cycles) for the tested air-fuel ratios are shown in Figure 25. At an air-fuel ratio of 20, the laser system provided NMEP >6 bar at the given intake pressure. As the intake pressure was very near atmospheric, it could not be lowered further. The two points presented at this air-fuel ratio have NMEPs of 6.85 (low energy) and 6.96 bar, representing an increase of 12% and 14% for the same intake pressure. COV of NMEP is shown in Figure 26. The laser system provided stable engine operation (COV <10%) at an air-fuel ratio of 20 ($\phi = 0.86$), while the electric spark plug was unstable (COV >10%). At maximum, an 86% decrease in COV was observed with the laser system. Increasing the air-fuel ratio to 23 ($\phi = 0.74$) resulted in unstable engine operation with the laser, while the electrical system was so unstable a test point could not be taken. Based on the criteria for stable engine operation, this suggests the lean limit for the laser system of somewhere between 20 and 23 air-fuel ratio, while the limit is <20 for the electrical system. Figure 27 shows the

brake specific fuel efficiency. The laser system provided a maximum increase of 1.8% at air-fuel 20, but the efficiency decreased as the mixture was made leaner. The positions of 10, 50, and 90% mass fraction burn shown in Figure 28 were generally later for laser ignition. The one exception is the 90% burn position for laser energy of 7 mJ, which occurred earlier than for the electric plug. Finally, emissions are presented in Figure 29, with the laser out-performing the electric plug on all counts. The one laser point represents the low spark energy test.

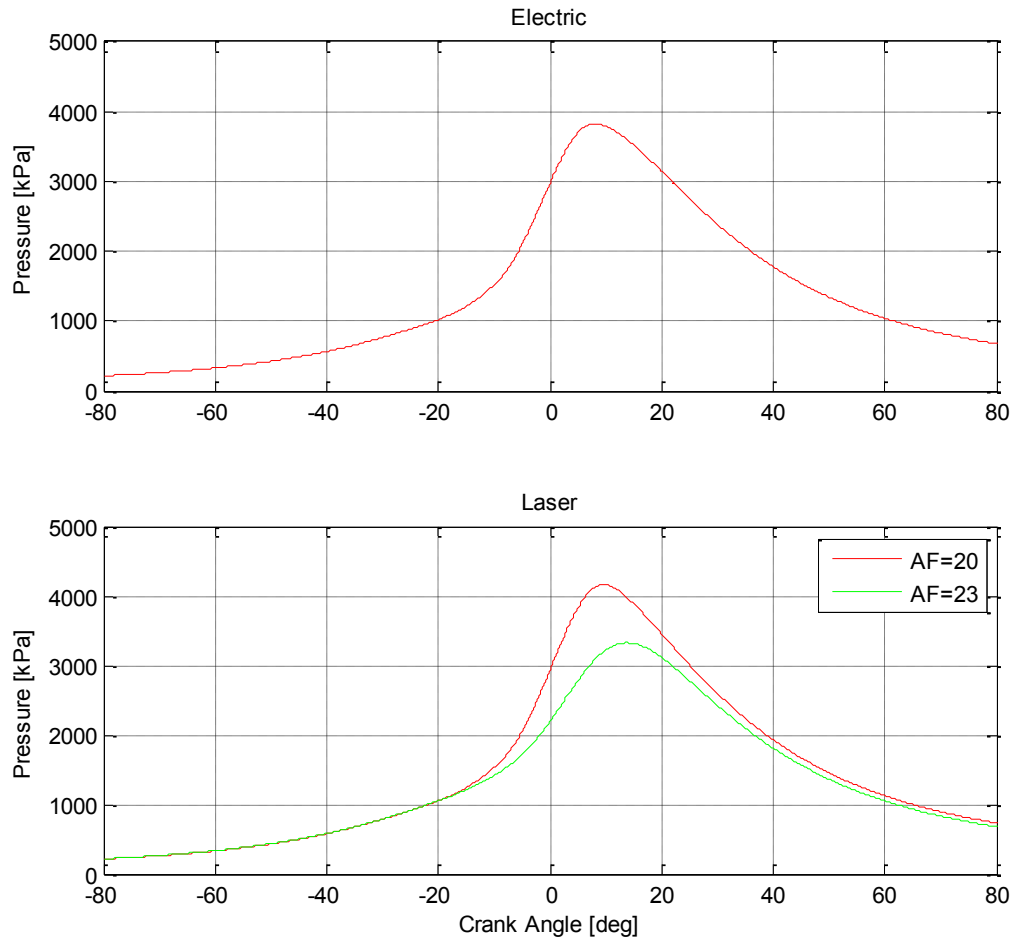


Figure 25 – Average pressure traces for electrical and laser ignition systems at 6 bar NMEP. For the laser at AF20, the low energy spark is shown. The laser system could reach a minimum of 6.9 bar NMEP for the given 101 kPa intake pressure at AF20, while the electrical system ran at 6 bar. Hence, the peak pressure is higher for the laser at that air-fuel ratio.

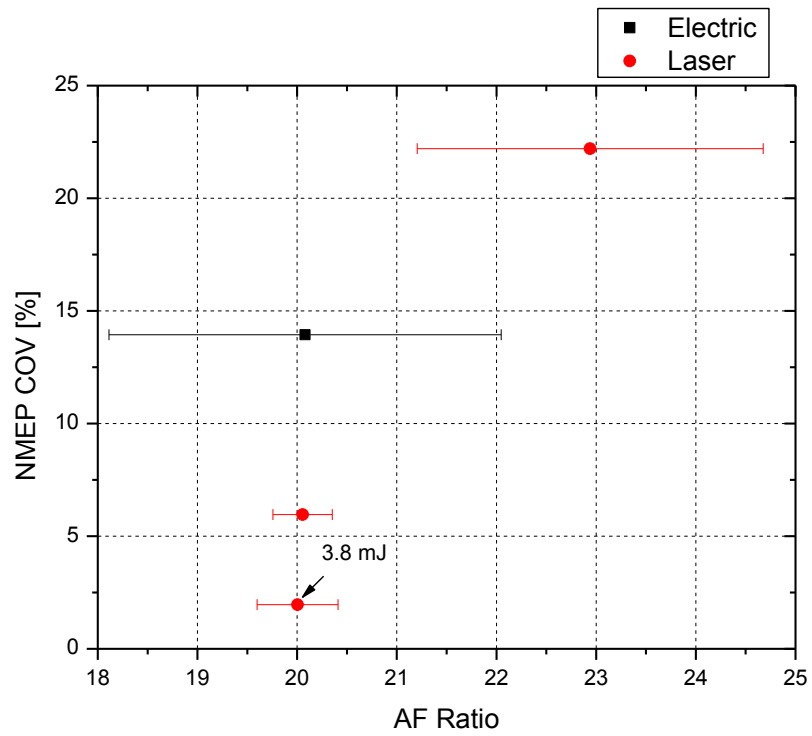


Figure 26 – COV of NMEP at 6 bar.

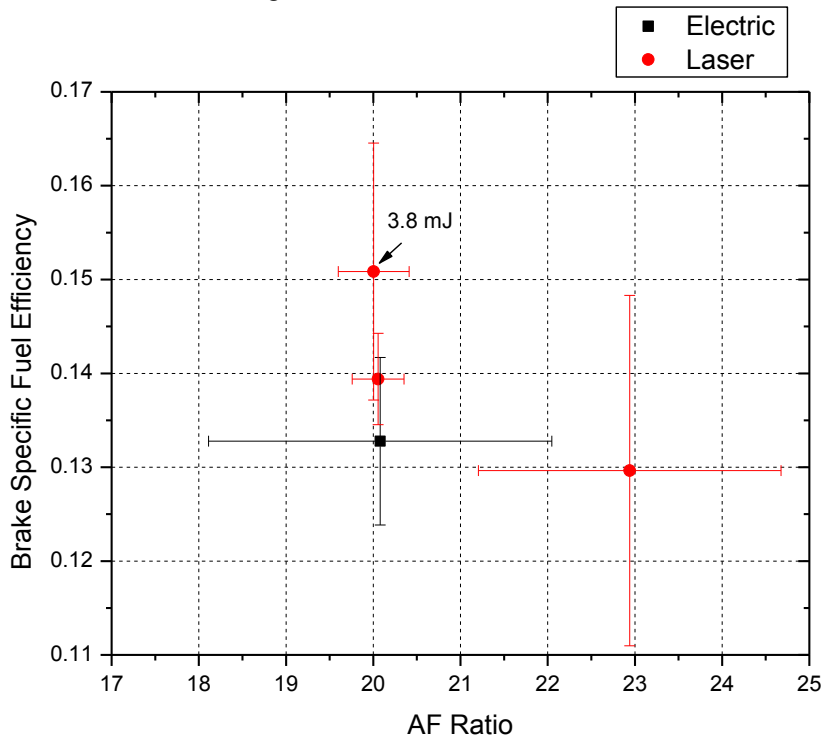


Figure 27 – Brake specific fuel efficiency at 6 bar NMEP.

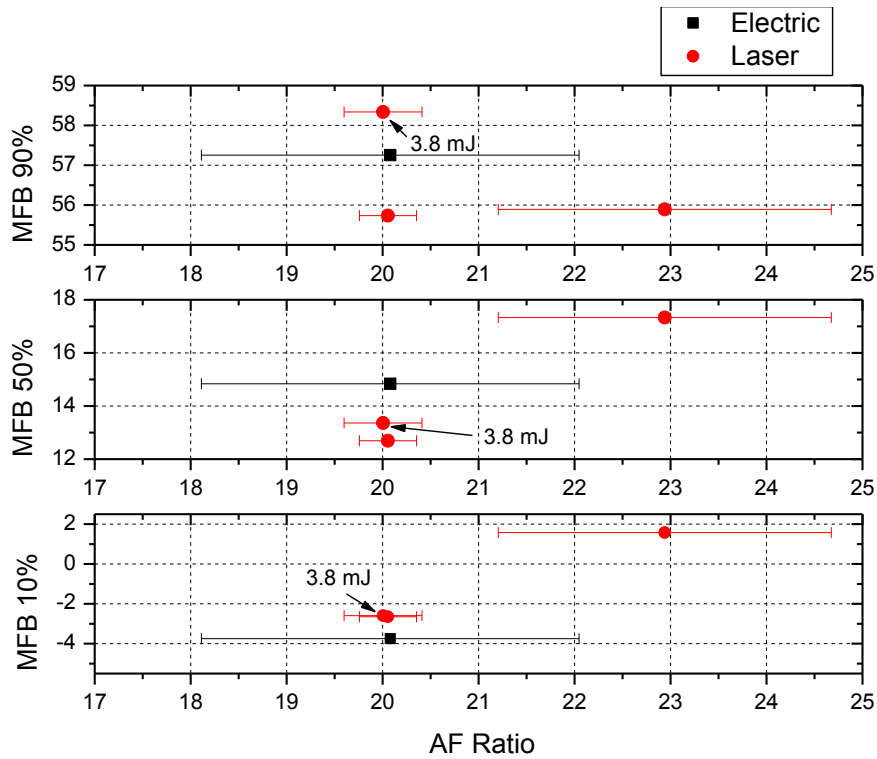


Figure 28 – Position of 10%, 50%, and 90% mass burn fractions at 6 bar NMEP. Ordinate represents degrees ATDC.

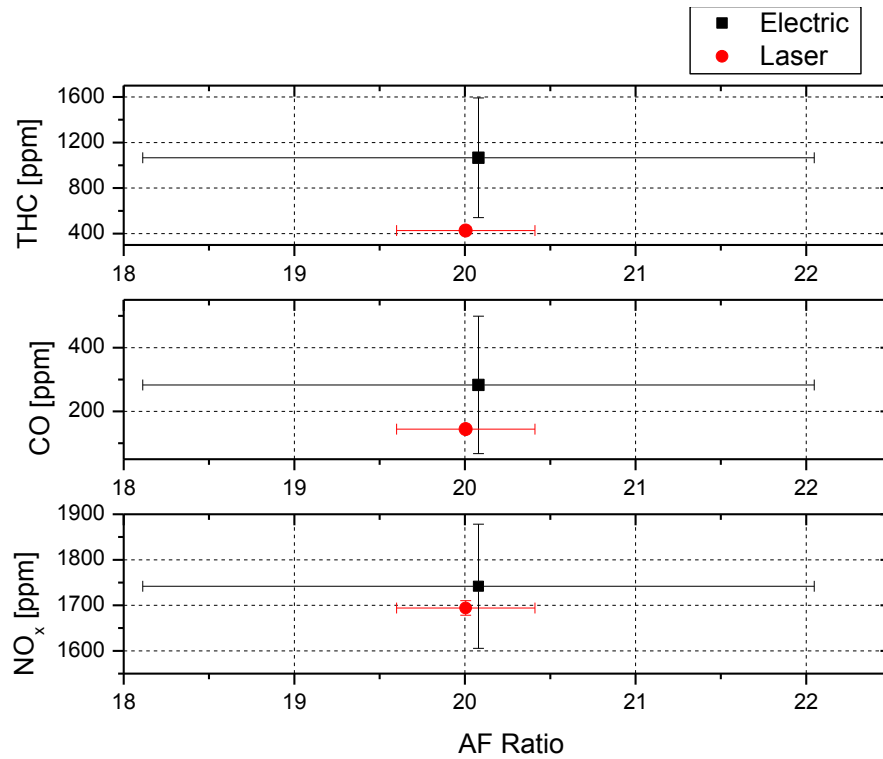


Figure 29 – Emission of NO_x, CO, and THC at 6 bar NMEP. All values are normalized to 15% O₂. The laser point represents the 3.8 mJ spark energy case.

3.2.3 8 Bar NMEP

To achieve this load condition, the intake manifold pressure was set to a value between 126 and 155 kPa, depending on the test point. Generally, the laser ignition system required less boost pressure than the electrical system to achieve the same NMEP. All points were at 8 bar NMEP within experimental error. Ignition timing was set at 20 degrees BTDC for both ignition systems using the MBT method. The laser energy was set at 7 mJ for all cases except one, in which an unexpected drop in laser power produced only 3.8 mJ spark energy. This point is marked in the figures. Pressure traces in Figure 30 indicate the laser system resulted in lower peak pressures that occurred later in the cycle compared to the electrical system. COV of NMEP and brake specific fuel efficiency are shown in Figures 31 and 32. The laser system maintains stable engine operation until an air-fuel ratio of 28 ($\phi = 0.61$), where the COV jumps to 19.3% and 22.5%. Up until this point, both systems show comparable COV. The electrical system maintains stable operation at its leanest tested condition of 30 ($\phi = 0.57$). Based on this data, the lean limit for the laser system is between 26 and 28 air-fuel ratio, while the electrical system is >30 . Below its lean limit, the laser system provides an increase of up to 3.1 percentage points in efficiency, while both systems are comparable at air-fuel ratio 28. Figure 33 shows the mass fraction burn locations. At air-fuel 28, the laser system completes the burn fraction consistently behind the electrical system. Slightly richer at air-fuel 26, the laser system appears to burn faster, and at air-fuel 24 both systems are comparable. Emissions data in Figure 34 are also comparable for most data points, with two notable exceptions. First, NO_x production at air-fuel 26 was significantly reduced by

the laser system. Second, THC emission at air-fuel 28 was higher for the laser, consistent with the large COV at that point.

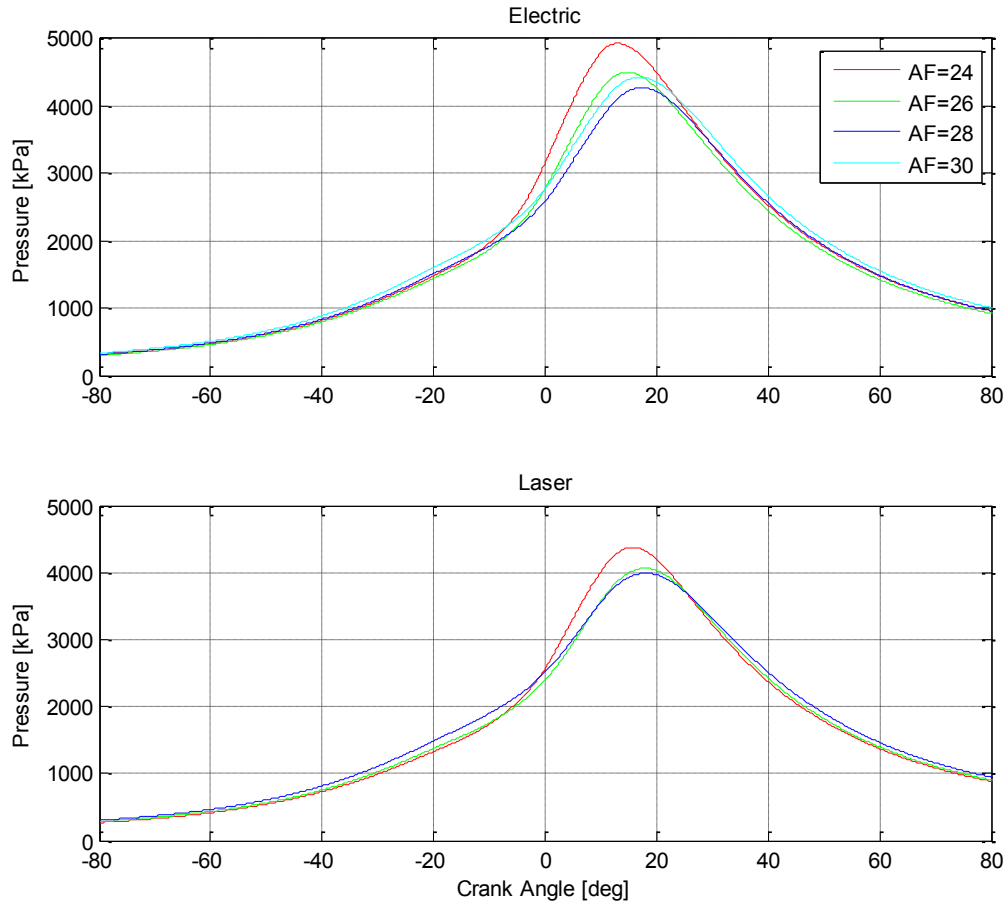


Figure 30 - Average pressure traces for electrical and laser ignition systems at 8 bar NMEP. Where there are duplicate data points for the laser system (AF 24 and 28), the point with lower COV is shown. At AF28, this corresponds to 3.8 mJ spark energy.

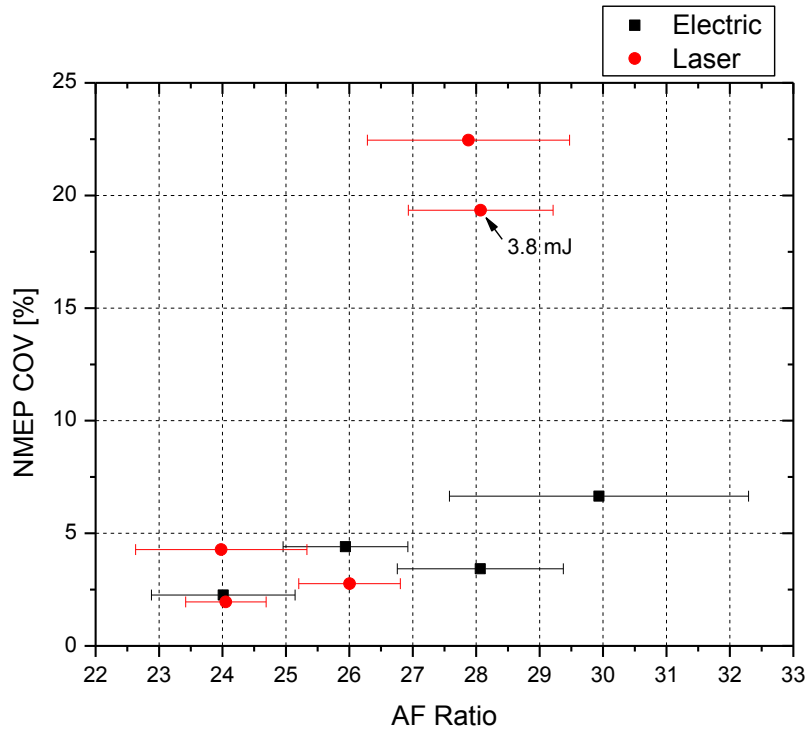


Figure 31 - COV of NMEP at 8 bar.

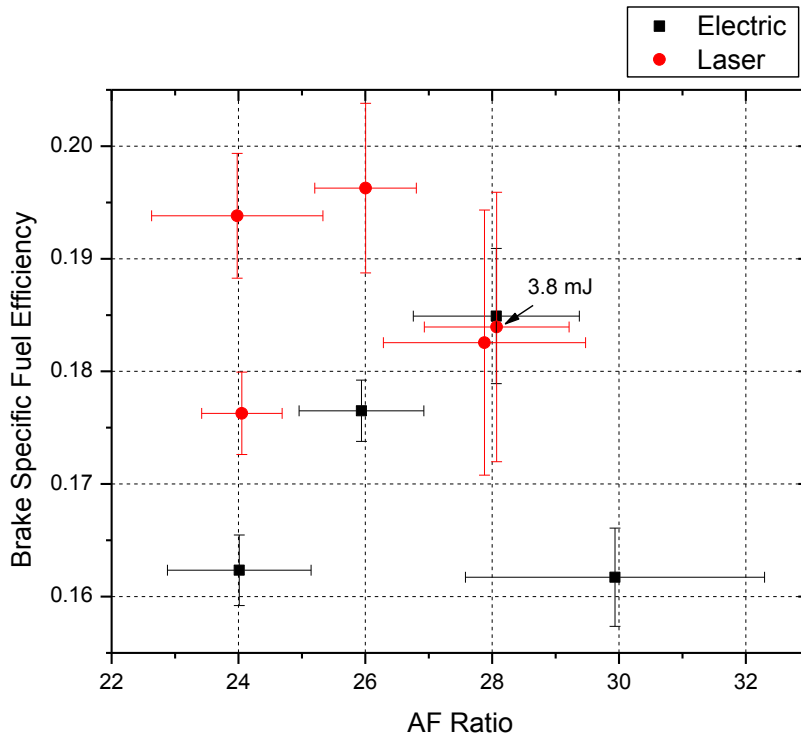


Figure 32 - Brake specific fuel efficiency at 8 bar NMEP.

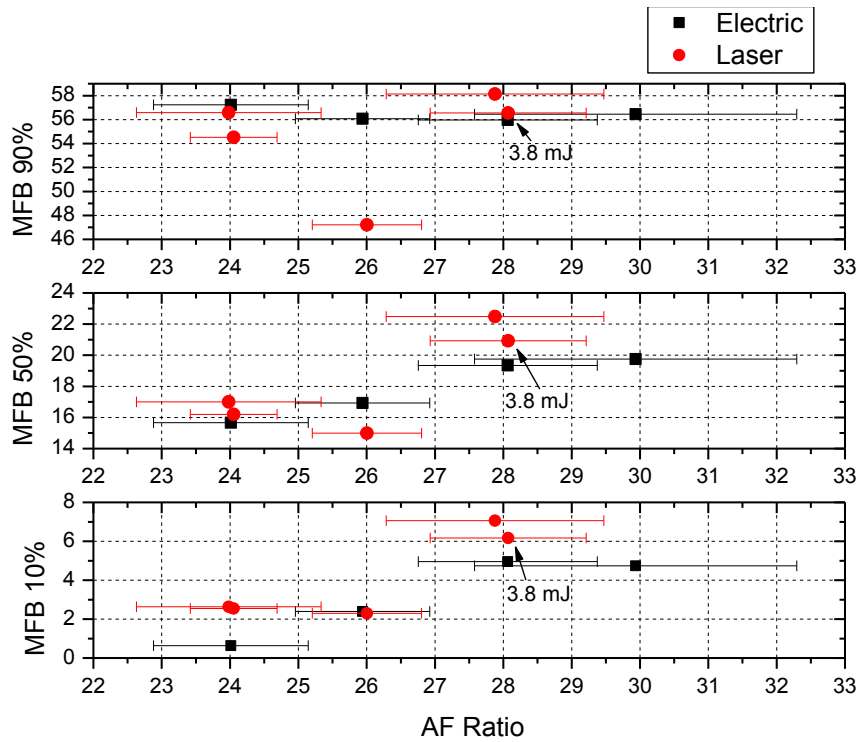


Figure 33 – Position of 10%, 50%, and 90% mass burn fractions at 8 bar NMEP. Ordinate represents degrees ATDC.

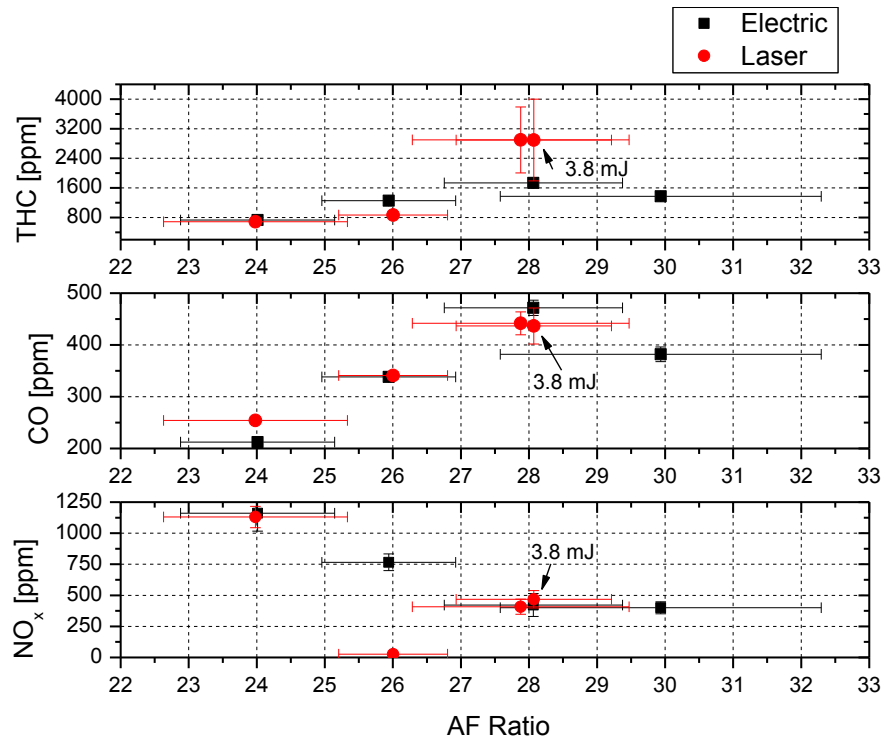


Figure 34 - Emission of NO_x, CO, and THC at 8 bar NMEP. All values are normalized to 15% O₂. Laser point at AF24 represents the test with lower COV.

3.2.4 12 Bar NMEP

To achieve 12 bar NMEP, the boost pressure had to be set between 175 and 220 kPa depending on the load point. Again, intake pressures were generally higher for the electric system for the same NMEP. All values of NMEP are 12 bar within experimental error with the exception of one laser point at an air-fuel ratio of 36, which had a nominal NMEP of 12.9 bar and is marked on the plots. Ignition timing was set at 18 degrees BTDC for all test points. Laser spark energy was nominally 7 mJ, however at air-fuel 26 an unexpected drop in laser power lowered the energy to 5.1 mJ. Also, at lean conditions (air-fuel 34 and 36) the energy was raised to 8.3 mJ. Average pressure traces for each air fuel ratio are shown in Figure 35. Like all previous loads, the laser system generally has lower peak pressure which occurs later in the cycle. COV of NMEP is shown in Figure 36. Values are comparable until air-fuel 28, where the laser is 2.4 percentage points higher. At an air-fuel ratio of 34 ($\phi = 0.50$), the electrical system keeps the engine barely within the stability limit, indicating the lean limit is near 34 for this ignition system. The laser system maintains engine stability beyond an air-fuel ratio of 36 ($\phi = 0.48$), indicating the lean limit for the laser is >36 . Fuel efficiency is shown in Figure 37, and is better with laser ignition for all points where comparison can be made. At most the laser shows an increase of 2.0 percentage points at air-fuel 26. When the mixture is leaned to 36 air-fuel however, the efficiency drops sharply by about 3 percentage points. Mass burn fractions are shown in Figure 38, and again generally occur later for the laser system. The laser trails by about 2 degrees for 10% mass burn and between 1 and 3 degrees for 50%, with the difference growing as the air-fuel ratio is made leaner. 90% burns however show the opposite behavior, with the electrical system generally trailing

the laser by as much as 1.5 degrees. Finally, emissions data are shown in Figure 39. Again, the laser outperforms the electrical system by all measures. Maximum decreases are 34%, 19%, and 39% for NO_x , CO, and THC respectively in the range of 30 – 32 air-fuel ratio.

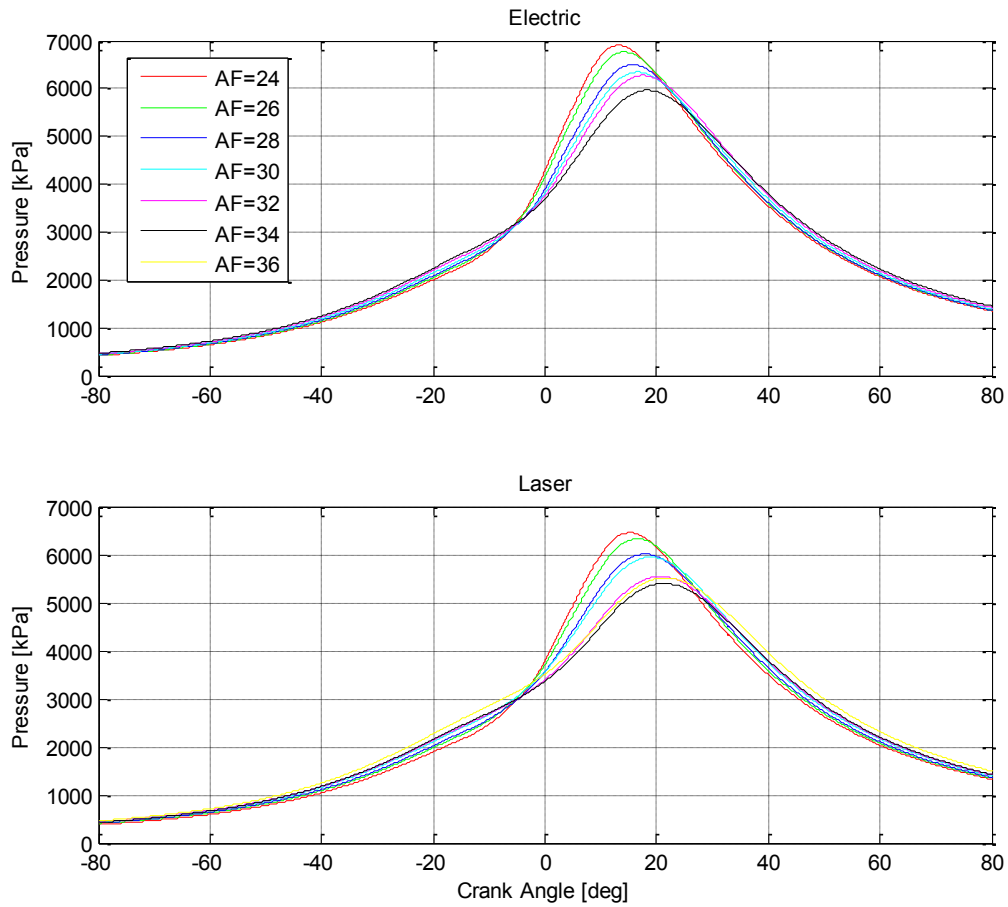


Figure 35 - Average pressure traces for electrical and laser ignition systems at 12 bar NMEP. The AF36 trace is from the data point with 12 bar nominal NMEP.

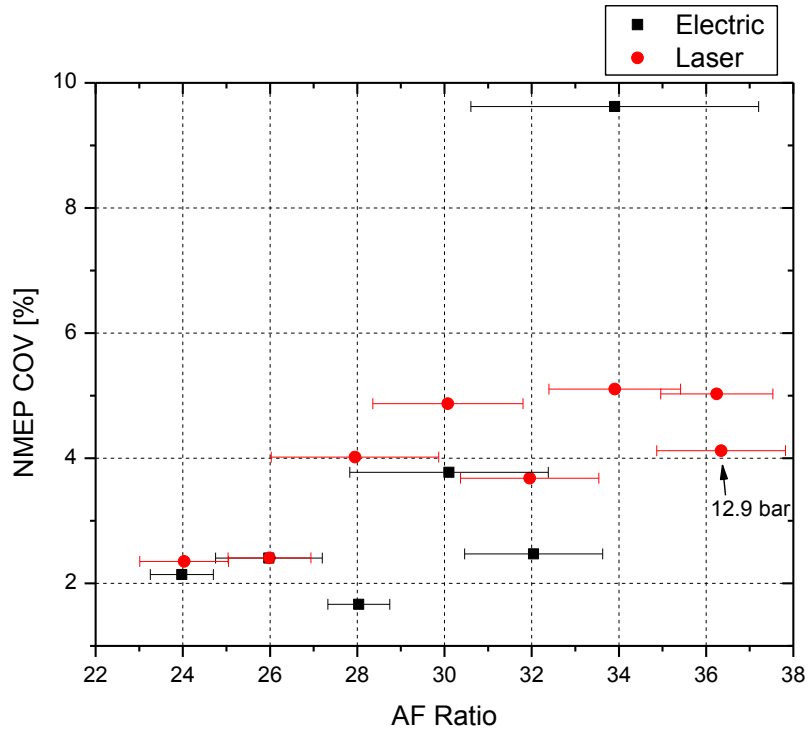


Figure 36 - COV of NMEP at 12 bar.

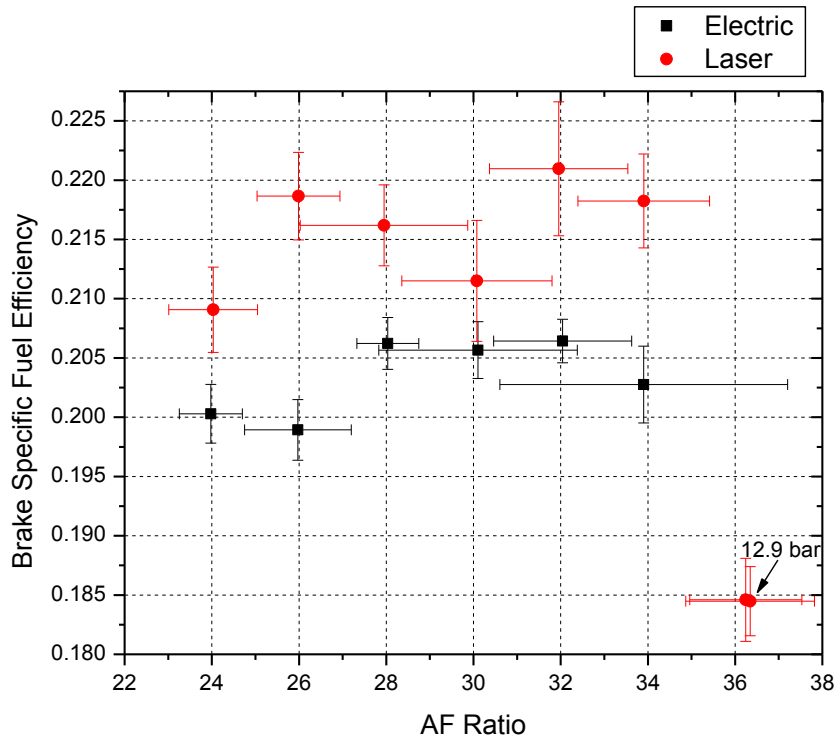


Figure 37 - Brake specific fuel efficiency at 12 bar NMEP.

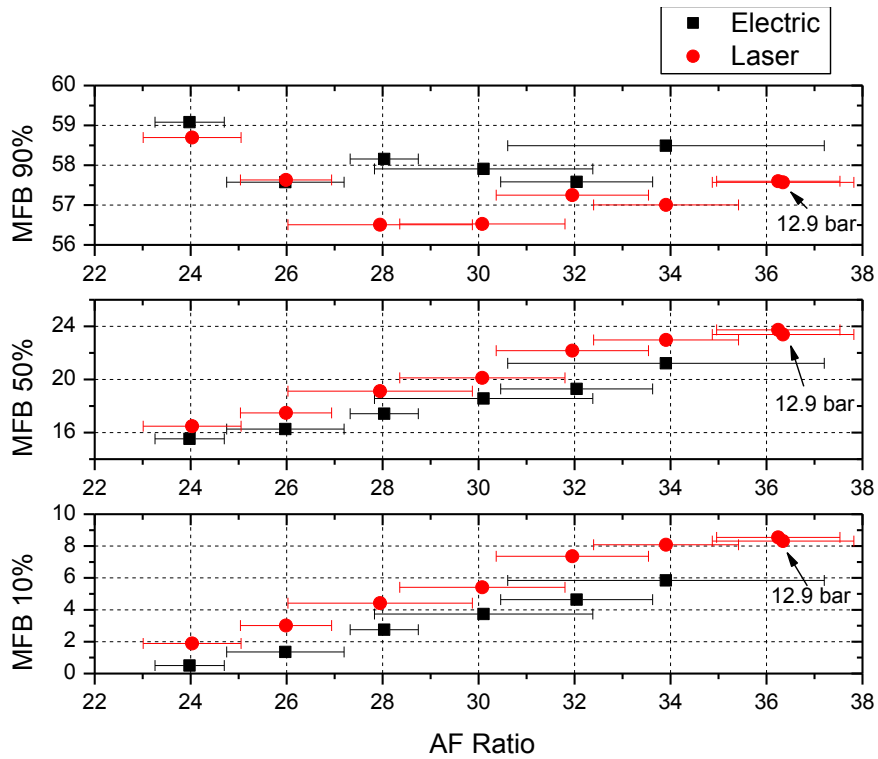


Figure 38 – Position of 10%, 50%, and 90% mass burn fractions at 12 bar NMEP. Ordinate represents degrees ATDC.

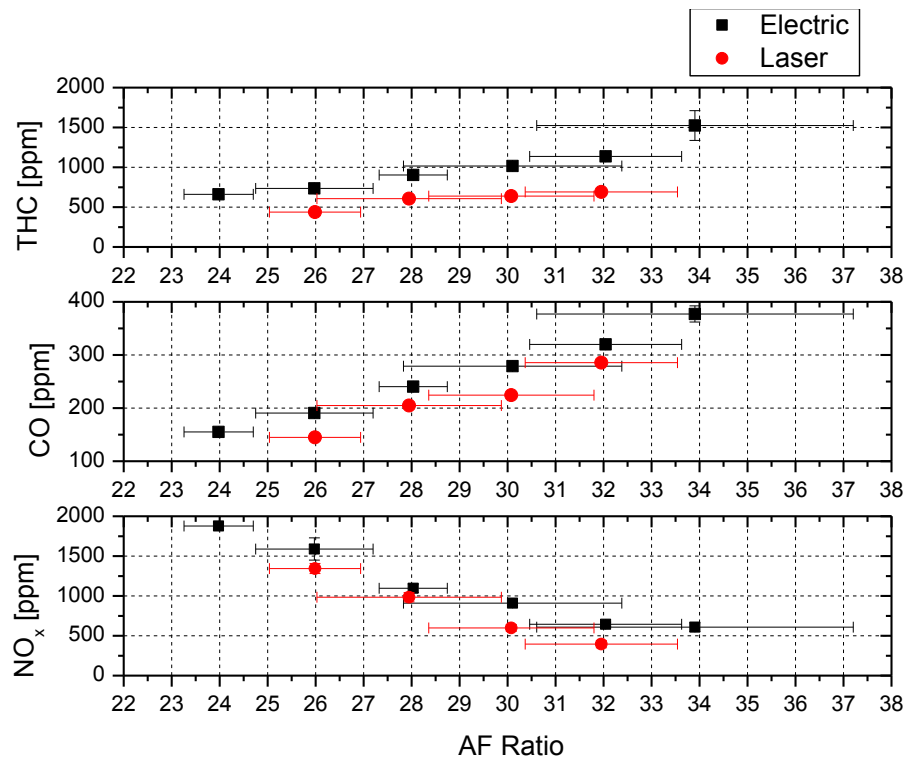


Figure 39 - Emission of NO_x, CO, and THC at 12 bar NMEP. All values are normalized to 15% O₂.

3.2.5 Lens Damage

While much of the fiber delivery system performed well during the test, damage to optical components within the laser plug limited the amount of time the engine could be run continuously. During the course of any given test, engine performance with the laser system would slowly degrade until significant misfires began to occur. The onset of this problem was indicated by a rise in COV of NMEP, followed by misfires, and finally the system ceased to spark reliably. The timescale from beginning a test to loss of spark was approximately 45 minutes. Visual inspection of the optical spark plug revealed the 10 mm Gradium lens had damage to its anti-reflection (AR) coating on the flat side of the lens, and there was damage to the top surface of the sapphire window. There was no noticeable damage to these components during benchtop testing, although they were never tested for longer than 20 minutes continuously prior to use on the engine. In an attempt to remedy this problem, the Gradium lens was replaced with an uncoated, 9mm focal length SF11 lens. In addition, the nominal beam diameter incident on the lens was increased from 4.5 to 7 mm to decrease the peak intensity. These modifications reduced the total beam delivery system transmission from 70% to 64% due to the lack of AR coating on the lens. With the new lens the engine was able to run for 2.5 to 3 hours before the sparking would begin to deteriorate. After this time, visual inspection revealed damage to the glass on the flat side of the lens, as well as the inside surface of the sapphire window. The damaged lenses are shown in Figure 40.



Figure 40 – Damage to focusing lenses in optical spark plug. Left: AR coated Gadium lens, sustained noticeable damage within 45 minutes. Incident beam was 9.2 mJ, 25 ns, \approx 4.7 mm in diameter. Right: Uncoated SF11 lens, sustained noticeable damage within 2.5 hours. Incident beam was 9.2 mJ, 25 ns, \approx 7.0 mm in diameter.

While there are many possible causes for this, there is no one mechanism that can be shown conclusively caused the damage. Damage thresholds are near 4 J/cm^2 at 20 ns, 1064 nm for the SF11 lens [65] and 2 J/cm^2 at 10 ns, 1.06 μm for the Gadium lens [66]. To determine the actual maximum irradiance, a beam profile was captured by CCD of the collimated beam incident on the lens. Based on the transmission of components up to that point in the fiber delivery system, an 11 mJ fiber input resulted in 9.2 mJ on the lens. By integrating over the beam profile and equating to the total energy, the maximum irradiance was approximated without assuming a Gaussian beam shape. The estimated maximum intensity on the lens was 0.23 J/cm^2 , about an order of magnitude below the published damage threshold. Still, 3 Gadium lenses and 3 SF11 lenses were damaged during the testing, as well as 6 sapphire windows. The window damage is believed to be a result of parts of damaged lens falling on its surface, as only the inside surface directly below the lens was ever damaged despite the outside surface seeing higher laser intensity.

Possible causes for the lens damage include a local reduction in damage threshold due to combustion gases leaking around the window, heat effects, and reflection of the beam off the window's inner surface. More investigation is required to determine the actual cause and fix the problem for future tests.

While some data points were affected by the lens damage in an obvious way (unstable engine operation), performance may have been affected in other test points before the damage became severe enough to warrant a shutdown of the engine. As mentioned previously, it took up to 3 hours before the lens had to be replaced, but the evolution of the damage before that time has not been characterized. While data that were severely impacted by this issue are not shown in the previous sections, the extent to which it influenced the presented results is unknown.

3.2.6 Discussion

Despite a few exceptions, the results show the fiber delivered laser ignition system resulted in higher efficiency than the electric spark plug. While much literature on laser ignited engines already exists, very few have used solid core fiber delivery. In general, the laser ignition system required less intake air pressure than electric ignition to achieve the same NMEP (See Figure 50, Appendix 2). In the six bar case, the boost pressure could not be lowered further so the laser increased the engine's NMEP. With the air-fuel ratio held constant, lower intake pressure results in a lower fuel flow rate, increasing the brake specific fuel efficiency. For all test points where comparison can be made with the exception of 8 bar at air-fuel 28, laser ignition resulted in an increase in fuel efficiency. COV was comparable between both systems, with the laser showing slightly lower COV at 6 bar and slightly higher at 12 bar. The lack of a clear trend can

partially be explained by the air-fuel ratio control system. Air-fuel ratio measurement was performed by an O₂ sensor in the exhaust, which closed the loop on the PID controller. The controller gains had not been optimized prior to the test, which resulted in a large underdamped oscillation about the nominal air-fuel ratio (hence the large error bars on the AF Ratio axis). Furthermore, any misfires or incomplete combustion caused erroneous air-fuel measurements, resulting in incorrect feedback to the controller. Large swings in air-fuel ratio changes the dynamics of combustion and further contributes to an increase in COV. As any small cycle to cycle variations can be amplified in this manner, it is difficult to make comparisons between minor differences in COV. Despite this complication, an improvement in COV from the laser system was not expected during this test, as energies much higher than the minimum ignition energy are required to significantly lower the COV [25,31].

Large differences in COV, such as those used to determine the approximate lean limit for stable combustion (>10%) still give a representation of the capabilities of each ignition system. However, based on the error in air-fuel ratio measurement, the data show that the lean limit is similar for both ignition systems at all loads considered. An interesting result is that the laser system was able to reach a similar lean limit with significantly lower energy than the published 10-20 mJ required. This is most likely due to the small focal volumes achievable with the good output beam quality and short focal length lens of this ignition system. It has been shown experimentally [11,27] that decreasing the focal length of the focusing lens reduces the minimum pulse energy required for ignition of a methane-air mixture. It was found that the minimum pulse energy could be reduced to as low as 3 mJ by reducing the focal spot size [27]. A

possible explanation for this can be found in the hot gas ignition model, which assumes that ignition will occur if a sphere of gas above some minimum radius is heated to an elevated temperature for longer than the induction time. The minimum radius is taken as the thickness of a flame in the ambient conditions at the time of ignition, and can be approximated using a simplified laminar flame speed analysis [1,25,67]. With this approximation, the minimum radius (and consequently minimum energy) is dependent on pressure and temperature; an increase in either will result in a decreased radius. So long as the volume of hot gas remaining after the plasma shock wave decays is larger than this minimum radius, ignition will occur. If the volume is made smaller by focusing the laser to a tighter point, (as is the case with this experiment) less energy will be required to heat the gas to a sufficient temperature. A combination of the small focal volume and decreased flame thickness due to the elevated gas temperature and pressure inside the combustion chamber allowed ignition to occur with relatively low spark energy.

As outlined in Chapter 1, one of the potential benefits of laser ignition is the overdriven flame kernel during the early stages of ignition. The results of this test however show no overdrive, and in most cases the laser ignition results in longer 10% mass burn fraction duration than the electric spark plug (see heat release curves in Appendix 2). Most all pressure traces show a lower rate of pressure rise for the laser ignition system at a given air-fuel ratio. 90% mass burn tends to display the opposite behavior, with the laser occurring earlier in most cases. Two factors are likely to have contributed to this. The first involves the state of the gas at ignition. As the laser system required less boost pressure to achieve the same NMEP, the charge density was generally lower for the laser, which translates to decreased pressure and temperature at ignition. As

flame speed is very dependent on initial temperature, it is expected that the denser charge would propagate the flame more quickly. The second possible factor is the low laser energy. The shockwave generated by laser breakdown is largely responsible for the overdrive which speeds the development of the flame kernel [12]. This shockwave has often been modeled as a Taylor blast-wave process to compute the radius and velocity of the shock as a function of time, as well as the peak temperature and pressure. As expected, higher laser pulse energy result in shockwaves with larger propagation velocities, higher peak pressures and temperatures, and longer decay time [15]. The shock is initially strong enough to oxidize all the fuel molecules it encounters, which couples the flame reaction zone to the shockwave. The flame kernel will eventually detach from the shockwave, but the energy from the shock will leave radical species in its wake, helping the trailing kernel expansion. This expansion is proportional to the strength of the shockwave and hence the spark energy [11]. Computational models have shown that an addition of radicals as well as heat energy to the ignition volume will reduce the chemical induction time [16], and experiments verify that increasing the laser pulse energy will speed the flame propagation [27]. Therefore, it is expected that if more energy could have been delivered in this test, the difference in mass burn fraction between electric and laser spark would have been similar to that seen in previous engine tests [6,20,31,44].

Despite the initially low flame speed with the laser ignition system, it tended to show overall shorter burn duration. For a given test point, the difference between 10% and 90% mass fraction burn was 1 – 3 degrees shorter for the laser system. It is possible that the slow then fast burn scheme was beneficial to the engine in terms of efficiency.

At similar ignition timing, laser ignition showed an increase in brake specific fuel efficiency for every test point except 8 bar, air-fuel 28, which was unstable with the laser. To achieve the same load condition, the laser system required less boost pressure for equal air fuel ratio, consuming less fuel and hence increasing the efficiency. Reducing the intake pressure will also reduce the temperature at the point of ignition, which can further contribute to the decreased early flame speed [67]. The laser's slightly later 10% mass burn fraction location resulted in lower peak pressures and thus a lower peak temperature, which reduced the amount of heat lost through conduction out of the combustion chamber. The remaining mass of reactants were consumed at a rate slightly faster than the electrical ignition system as the chamber was expanding, further decreasing the amount of heat lost. Overall shorter burn duration also suggests the laser resulted in more complete combustion of the intake charge. This is supported by the generally lower amount of THC emission with the laser. As more of the fuel energy was available for work, the laser system allowed higher efficiency engine operation.

Evidence of lower temperature combustion with laser ignition is also present in the emissions data, specifically NO_x production. The primary NO_x mechanism in combustion engines is the Zeldovich mechanism, in which O, OH, N_2 , O_2 and N react to form NO. The rate-limiting reaction involves the dissociation of an N_2 molecule with an oxygen atom, and has large activation energy, making it very temperature dependent. It is also assumed that the reaction happens much slower than the combustion chemistry, meaning NO production usually takes place in the burned gases. Once the temperature drops below 1800-2000 K, the reacting rate greatly slows, and the NO_x concentrations freeze [68]. Based on the lower peak pressures (indicating lower peak temperature) and

shorter total burn durations observed with the laser ignition system, it is not surprising that measured NO_x emissions are lower than the electric spark on almost all test points. The one notable exception to this trend is 8 bar air-fuel 28, where burn durations and efficiencies were similar for both ignition systems indicating higher average combustion temperatures, which resulted in similar amounts of NO_x emission. THC emission has also been improved with the laser ignition system on nearly all test points. These emissions are made of carbon-containing molecules that did not fully complete the combustion reaction, which can be caused by a number of factors including quenching and crevices in the combustion chamber. Crevices such as near the spark plug and piston rings are the largest contributor to THC emissions, resulting in approximately 40% of the total emission [68]. This would suggest the geometry of the laser spark plug is a primary contributor to the lasers improved performance, although quenching between the spark plug electrodes could also be a factor. Generally THC emission is increased as the air-fuel mixture is made leaner as a result of incomplete flame propagation [67], and the trends shown in this test agree. Again, the 8 bar air-fuel 28 case is the exception, as the unstable operation resulted in a large number of misfires and hence increased THC emission. Finally, CO emissions are presented, with total concentrations much lower than the other measured pollutants. CO is usually only a concern in rich and near stoichiometric operation, and the lean mixtures considered here do not produce large amounts. Still, the laser shows slightly better performance for 6 and 12 bar cases, with similar performance at 8 bar. CO can be formed in a similar manner to NO_x , where the rapid decrease in temperature during the expansion stroke causes the concentration to freeze in an amount higher than equilibrium [67]. Gases that burn early tend to reach a

higher temperature than gases that burn later, and the CO destroying reaction cannot keep up with the rapid decrease in temperature when the gas expands and leaves the cylinder. Therefore, quicker burning will result in an increase in CO [68]. As the electric spark resulted in an earlier 10% mass burn fraction, slightly more CO was present in the exhaust.

4 Laser Plasma Formation Using Preionizing Ultraviolet Pulses

While conventional non resonant breakdown in gases has been extensively studied, limitations still exist in its utility as an ignition source. The electron avalanche process that governs the behavior of typical laser induced sparks of nanosecond duration at visible and near infrared wavelengths behaves in a stochastic manner, and for all practical purposes is either “on” or “off.” While such behavior may be acceptable in some applications, control over the spatial geometry of the ignition source, its duration, and temperature is sometimes desired. In addition, the blast wave formation typical of EAI consumes a significant portion of the energy deposited by the spark. Phuoc et al. calculated up to 70% of the energy absorbed in a 1064 nm laser spark was used in the propagation of the blast wave, while as little as 7% of the spark energy was actually available for ignition [30]. Further, gas dynamic effects from laser sparks also make ignition near the lean limit difficult due to high rates of flame stretch, which is further aggravated at low pressures [12].

Given the limitations and somewhat uncontrollable nature of conventional laser sparks, there is emerging interest in methods of controlling and tailoring the laser plasma. One candidate method is to use two laser pulses; the first to preionize the gas and the second to add energy in a decoupled and controlled fashion [69,70]. Such approaches could allow tailoring of the laser plasma (size, plasma conditions, temperature) for different applications, for example spatially extended heated gas volumes ($T \sim 1000\text{-}2000$

K) for ignition. In particular, a recent body of work has examined preionization based on plasma filaments formed by femtosecond lasers, and overlap of additional laser pulses [71–73]. Shneider et al. has performed modeling of the decay of femtosecond filaments and shown the possibility of extending the plasma lifetime with overlapped nanosecond pulses that suppress three-body electron attachment and dissociative recombination processes [70]. Such approaches may also allow formation of microwave wave guides in the atmosphere [74], light sources and diagnostics, lightning control [75], and laser triggered spark gaps [21]. In related work with nanosecond pulses, Yalin et al. studied the use of two 1064 nm laser pulses to create laser plasmas [69]. In this case the preionizing laser pulse provided full breakdown on its own, but it was shown that overlapping a second pulse provided a means of adding additional energy to the plasma. Common to these approaches is consideration of the roles of MPI versus EAI. For example, it can be beneficial to use ultraviolet laser light for preionization since a smaller number of absorbed photons are required for ionization [76]. In addition, inverse bremsstrahlung absorption responsible for EAI is less prevalent at shorter wavelengths [25]. Pulse duration also plays an important role, for example for picosecond pulses one can see a clear transition from MPI at low pressure to EAI at higher pressure [77,78], because at low pressures the electrons do not have sufficient time to collide with other molecules thereby hampering the EAI process [26].

In this chapter, the effects of preionization in air using ultraviolet pulses of nanosecond duration, as well as the interaction between the ultraviolet preionizing beam and an overlapped near-infrared energy addition beam at various pressures are studied. Images of the plasma are taken using laser illuminated Schlieren imaging to determine

approximate size and temporal evolution. Section 4.1 describes a method to estimate the electron number density (n_e) created by the preionizing ultraviolet beam at sub-breakdown conditions. Results are presented in terms of the dependence of electron density on ultraviolet laser intensity. Section 4.2 presents experimental studies of overlapping a near-infrared beam with the preionizing ultraviolet beam.

4.1 Estimation of Electron Number Density

In order to assess the effectiveness of the preionizing beam, the electron density within its focal volume was estimated by measuring the electrical conductivity of the plasma. The method is similar to that used by Zvorykin et al. [79], where free electrons are accelerated by an electric field (external applied voltage) and the resulting current is measured.

4.1.1 Experimental Setup

The setup for this experiment is shown in Figure 41. The laser source for the preionization was the fourth harmonic output of a Nd:YAG (Continuum PR II) at 266 nm, with 10 ns pulse duration. Output energy could be varied from <1 mJ to 60 mJ so that the intensity within the focal region could be varied over a large range. The beam was focused with a 500 mm focal length spherical lens producing a waist diameter of $\approx 150 \mu\text{m}$, and a fraction of the input energy was reflected off a window into an energy meter (Ophir). For the conductivity measurements, two ring electrodes were placed such that the beam passed through the rings and the waist location was equidistant between the two electrodes. The gap between rings was varied between 1, 2, and 3 cm. A high voltage DC power supply generated an electric field between the rings, and the

photocurrent passed through a 47 ohm resistor. The voltage drop across the resistor was measured by an oscilloscope with 50 ohm input impedance. Both the laser and oscilloscope were triggered with a pulse delay generator (BNC 555). Following the method outlined in Zvorykin et al. [79] plasma conductivity, σ , could be calculated as:

$$\sigma(t) = \frac{l}{SU} u(t) \left(\frac{1}{R_{osc}} + \frac{1}{R} \right) \quad (6)$$

where t is time, l is the electrode gap spacing, S is the plasma cross section area (taken as the cross sectional area of the beam waist), U is the applied voltage across the electrodes, u is the measured oscilloscope signal, R_{osc} is the oscilloscope input impedance (50 Ω), and R is the load impedance (47 Ω).

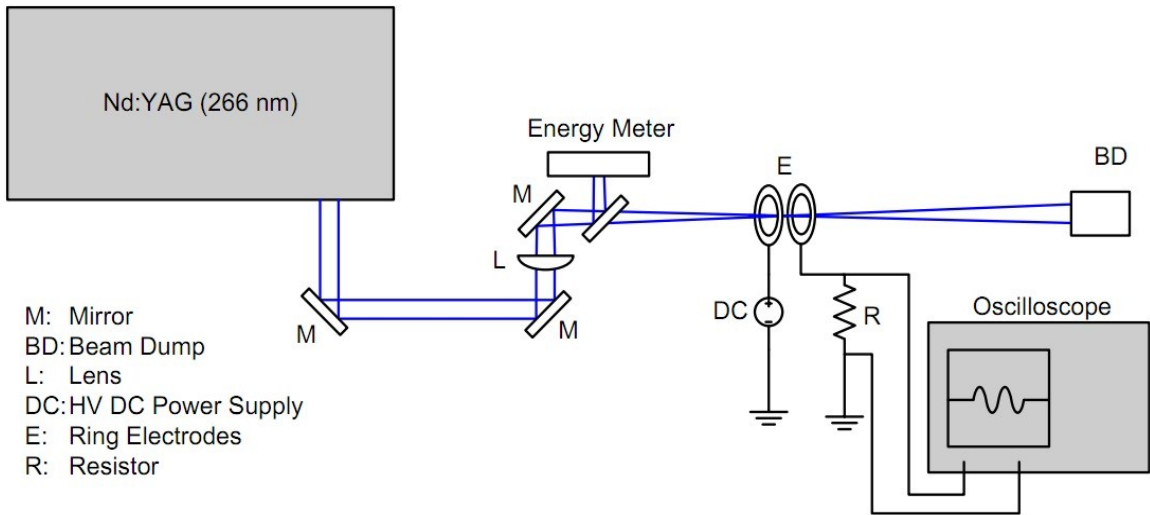


Figure 41 – Schematic of experimental setup used for measurement of n_e .

4.1.2 Results and Discussion

Given the plasma conductivity calculated from Equation 9, the electron density could be estimated as:

$$n_e = \sigma / e\mu_e \quad (7)$$

where e is the electron charge and μ_e is the electron mobility, assumed to be $600 \text{ cm}^2(\text{V}\cdot\text{s})^{-1}$ in air at atmospheric pressure [79]. (The exact value of mobility may vary with plasma conditions and is the limiting factor on the accuracy of the measurement, but the results are still useful in terms of showing general preionization trends.) Calculated electron density values for various laser intensities are shown below in Figure 43. Data were taken up to $I_{266} \approx 1.5 \times 10^{10}$, at which point visible spark formation and breakdown commenced. As shown by Equations 6 and 7, electron density is time dependent and experimental results show its growth and decay follows the shape of the laser pulse. Figure 42 shows a plot of the normalized laser pulse and oscilloscope response, $u(t)$ which corresponds to the first data point in Figure 43 ($I \approx 1.65 \times 10^{10}$). In this case, the gap distance l was equal to 1 cm and the voltage U was 1 kV. For use in equations 6 and 7, the first peak of the oscilloscope signal was extracted, and the remaining oscillation removed. It is believed that the oscillation is due to an impedance mismatch between the load resistor and the oscilloscope. Future iterations of this experiment would benefit from proper impedance matching so the electron number density decay could be more accurately known. For the data shown in Figure 43 calculated from equations 6 and 7, the average value of the peak extracted from $u(t)$ was used. The datapoints include all three electrode spacings, and follow an approximate $I^{2.3}$ dependence. This is similar to the results of Zvorykin et al. [79] who found an I^2 dependence using a 248 nm beam at similar intensity values which they attributed to ionization by a 2+1 resonant enhanced MPI process (i.e. two photons to reach a resonant state of oxygen or nitrogen followed by ready ionization with an additional photon). A similar trend is observed in this measurement and it clearly shows preionization due to the ultraviolet beam, and is also

suggestive of a 2+1 mechanism. Similar measurements of the 1064 beam did not show any preionization, presumably owing to the substantially lower photon energy at longer wavelengths.

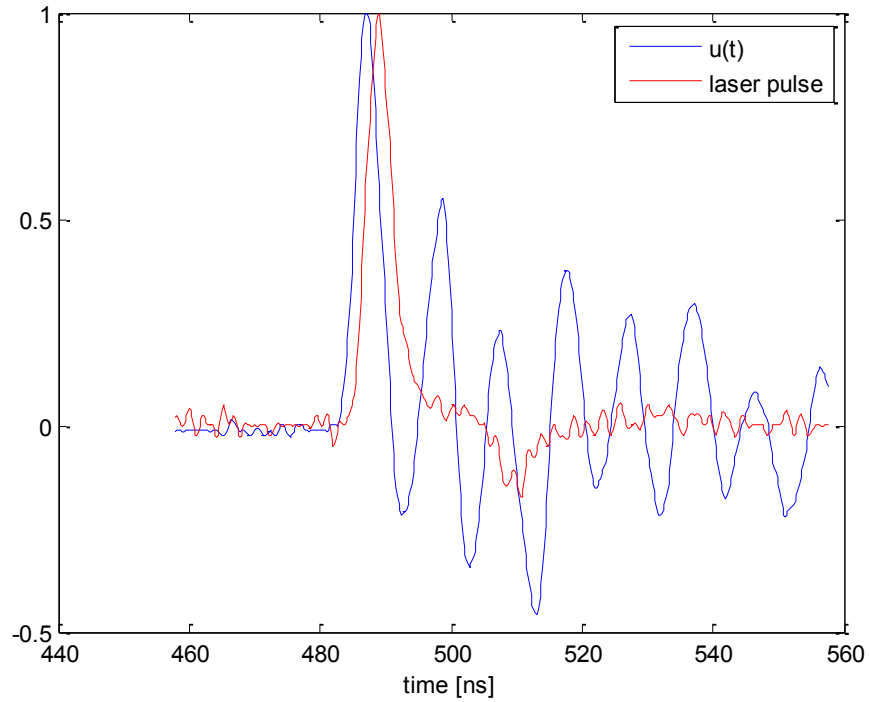


Figure 42 – Plot of normalized laser pulse and oscilloscope signal $u(t)$. Data representative of the first point in Figure 43 ($I \approx 1.65 \times 10^{10}$), $l = 1$ cm, $U = 1$ kV.

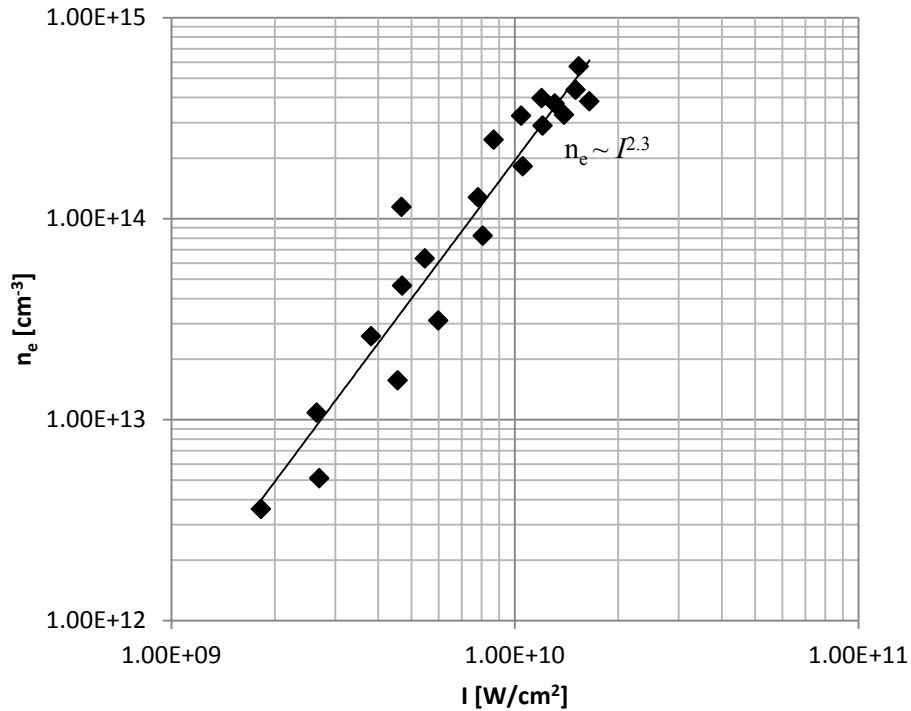


Figure 43 – Electron density versus laser intensity. Linear fit corresponds to a dependence of $I^{2.3}$.

4.2 Laser Plasmas Due to Overlapped Pulses

In comparison to plasma formation with a single beam, the interaction between two beams is much more complex. Here two experimental parameters are varied, namely the beam energy and ambient pressure, to study the dual pulse interaction. Initial studies using a setup similar to that described in Section 4.2.1 have shown that an initial ultraviolet beam can generate preionization, but the overlap of an additional beam tends to either form a full spark (due to EAI) or has no noticeable effect, i.e. there are no cases where the overlapped beam increases the temperature or ionization without full breakdown. This section presents a quantitative examination of the effects of combined beams including imaging the plasma formation using a Schlieren technique.

4.2.1 Experimental Setup

Figure 44 shows the setup for this experiment. For the plasma formation, two Nd:YAG lasers were used with one at the 266 nm fourth harmonic (Continuum PR II) for preionization, and a second at 1064 nm wavelength (Spectra Physics DCR-3) for overlap and possible energy addition. The lasers were triggered and synchronized using a pulse delay generator (BNC 555), such that a delay of zero corresponds to temporal overlap of the pulse peaks. Both the preionizing and energy addition beams were passed through 300 mm focal length spherical lenses before hitting a beam splitter that reflected 266 nm light and transmitted 1064 nm light. The lenses were placed such that the waists of each beam were overlapped along the laser propagation axis, and the beam conditions upstream of each lens allowed for focal spot diameters that were approximately the same. A summary of beam parameters can be found in Table 6. A beam splitter was placed after the beams were combined to reflect a fraction of the energy into an energy meter. For this experiment the beams were collinear and meticulously aligned using a CCD camera and profiler software (Spiricon), to ensure there was overlap throughout the focal region. For the Schlieren imaging a third laser, also at 1064 nm (NewWave Gemini PIV), was used (see below).

In order to examine effects at various pressures, the focal volume of the overlapped beams was contained within a vacuum chamber. The chamber entrance and exit for the preionizing and energy addition beams were sealed with 25.4 mm (one inch) fused silica windows. Larger 50.8 mm (two inch) sapphire windows were used to pass the Schlieren beam through the chamber perpendicular to the two main beams. A valve was placed on each end of the chamber, one up and one downstream in order to control

the internal pressure by allowing ambient room air to flow through the volume. This allowed a constant stream of air across the focal volume to ensure fresh air was used for each test point. The Schlieren system employed the third Nd:YAG laser as a light source, which allows the evolution of the plasma to be viewed at different times with respect to the laser pulse. The beam was attenuated using a halfwave plate and polarizer and spatially filtered with a pinhole before being expanded to overfill the clear aperture of a one inch spherical lens. The resulting beam was collimated and approximately 20 mm in diameter, and was steered through the vacuum chamber with a pair of mirrors. Images of the test area were focused onto a CCD camera and recorded using profiler software.

Table 6 - Summary of beam parameters for energy addition.

Lasers	Wavelength (nm)	Pulse Duration (ns)	Waist Diameter (μm)	Energy (mJ)
Preionizing	266	10	150	0 – 60
Energy Addition	1064	13	150	0 – 220
Schlieren	1064	15	N/A	< 1

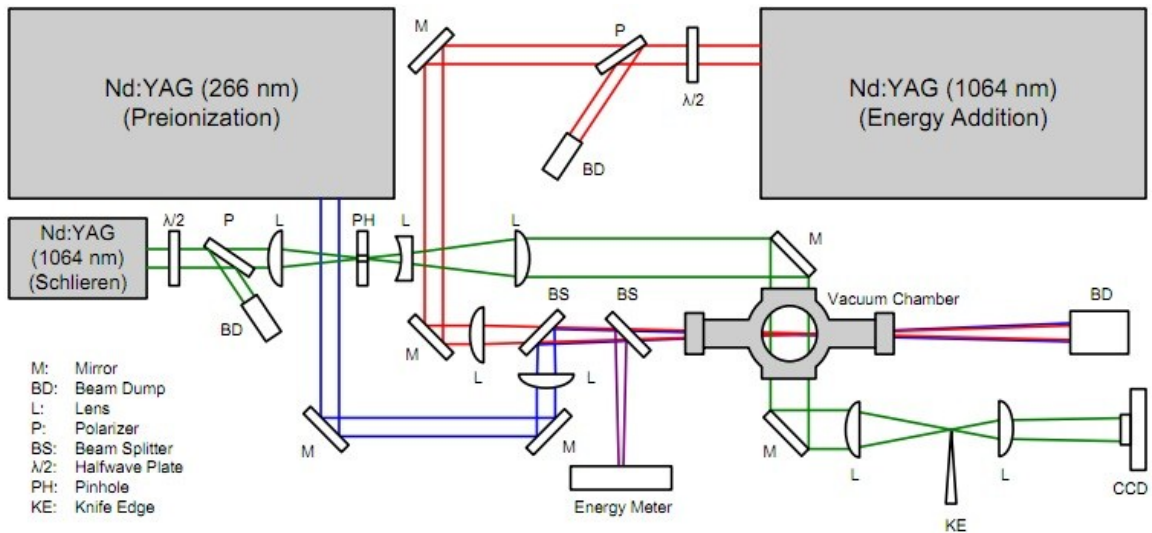


Figure 44 – Schematic of experimental setup used to study dual pulse energy addition.

4.2.2 Results and Discussion

Figure 45 shows the breakdown laser intensity (for full spark formation with 100% probability) of the 1064 nm beam versus the intensity of the 266 nm used for preionization. Preionization levels provided by the ultraviolet beam can be found from Figure 43. The measurements were recorded for a delay time between the two beams of 10 ns which appears to provide the largest influence on the 1064 beam, but the effects of delay were not extensively studied. Figure 45 includes data from only two pressures, but many interesting observations can be made about the shape of the curves. The first data points affixed to the ordinate represent the 1064 nm intensity required for spark formation on its own, with no UV preionization. Notice breakdown is achieved at intensities near 3 GW/cm^2 , an order of magnitude lower than the commonly accepted value of about 200 GW/cm^2 . It is possible that the large waist diameter ($150 \mu\text{m}$) reduced the amount of outward electron diffusion, allowing for breakdown at lower intensity. The very next points, as seen for $I_{266} \lesssim 10^9 \text{ W/cm}^2$, the preionization lowers the breakdown requirement for the 1064 nm beam substantially, even at very low preionization levels. Qualitatively speaking, this is related to the ineffectiveness of the 1064 nm radiation at inducing MPI (low photon energy), combined with its propensity for EAI (ω^{-2} scaling). Schlieren images in the abscissa region from 0 to $5 \times 10^9 \text{ W/cm}^2$ did not reveal any disturbance when viewing only the UV beam. While the presence of preionization was verified at these intensities in section 4.1 and manifests itself in the data shown here, the sensitivity of the Schlieren system was not high enough to view it. As described in section 4.1, the electron number density tended to follow the temporal shape of the laser pulse, which lasted about 10 ns. With a 15 ns Schlieren probe beam it

is impossible to resolve a disturbance that short, even if the refractive index difference it created was sufficient for the spatial resolution of the system. While it is possible smaller amounts of preionization existed at later times ($\sim 1 \mu\text{s}$), the Schlieren system was not able to resolve it.

As the preionization level was further increased, the additional benefits for 1064 nm spark formation decreased (increasing I_{266} did not result in a significant reduction in required I_{1064} for spark formation), up until point (a,b) in Figure 45. No visible or Schlieren disturbance was observed from only the UV beam in this area. At point (a,b), the first evidence of UV preionization was seen in the Schlieren image, but was not visible by eye. The image is shown in Figure 46b, and although very faint (details can be best seen in electronic version), a thin horizontal line can be seen indicating the presence of MPI (marked by white arrow). MPI requires the simultaneous absorption of several photons and consequently high laser intensity, and as such one would expect ionization created in this way to be localized to the focal volume. As the focal volume is approximately cylindrical, Schlieren disturbances with similar shape such as that in Figure 46b are attributed to MPI. It is interesting to note that while the two beams were overlapped and their waist locations were coincident along the beam axis (to precision less than approximately 1 mm), up through point (a,b) the 1064 nm breakdown occurred slightly upstream of the location where UV disturbances occurred. The position of the Schlieren beam remains fixed in all images in Figure 46 so comparison of relative position can be made.

At point (c,d) a noticeable drop in 1064 nm intensity is seen, and is also marked with a noticeable change in the Schlieren images. Figure 46d shows the UV beam alone.

While the image bears some resemblance to the previous point (Figure 46b), a shockwave can be seen leaving the plasma. It is possible that this indicates the intensity has reached the threshold for partial breakdown and gas heating, where the rate of electron generation just barely overcomes the various loss mechanisms. Given the shape of the image (long cylinder, shape of focal volume), the primary breakdown mechanism is likely still MPI. At this point, the 1064 nm breakdown moves slightly downstream to meet the leading edge of the UV plasma. One possible explanation for this phenomenon is that partial breakdown like that seen in Figure 46d causes a large jump in electron density. The additional electrons provide enough seeding for the 1064 beam such that the energy is absorbed without the need to generate its own seed electrons through MPI, significantly lowering the intensity required for breakdown. At lower preionization levels, some seed electrons exist but not enough for absorption of the 1064 nm beam. While much of the preionization generated by the UV beam likely occurs at its beam waist, some electrons are likely generated slightly upstream as well. These electrons combined with additional seed electrons generated through the high intensity 1064 nm beam cause breakdown slightly upstream of where breakdown occurs when no 1064 seeding is required.

At point (e,f) the required 1064 nm energy drops even further. This point also marks a significant change in the behavior of the two overlapped beams. Schlieren images in Figure 46f of the UV beam alone now show a small sphere at the leading edge of the plasma. This indicates the breakdown method has shifted to EAI, although the long tail indicates MPI is still present as well. While MPI can only exist where photons are present (within beam path), EAI is caused by the acceleration of electrons which collide with other molecules to create an avalanche of ionization in all directions. Hence,

EAI is attributed to the sphere shapes seen in Figures 46a, 46c, 46e, and 46f. At this point, the UV breakdown became visible to the eye. When the 1064 nm beam was added, the behavior was not typical of near infrared spark formation. The spark was no longer “on” or “off,” but rather acted more like a “dimmer switch.” Even very small amounts of 1064 nm intensity added to the plasma size. Increasing the intensity further made the plasma bigger, indicating that the 1064 nm energy was being absorbed, allowing the size of the plasma to be tailored in a controlled fashion. Given that visible breakdown occurs with the UV beam alone, increasing its intensity further did not significantly lower the threshold for 1064 nm spark formation as shown in Figure 45. The data points after point (e,f) show the required 1064 nm intensity to make a visible change in the Schlieren image, and remain relatively constant.

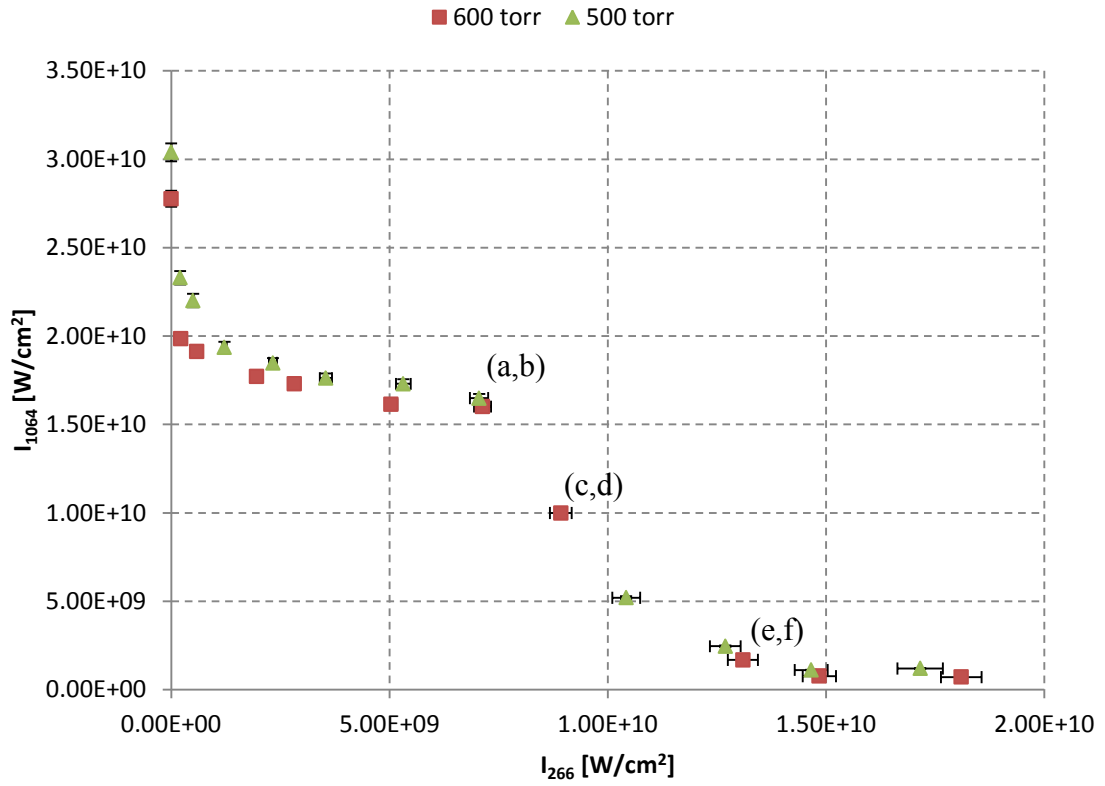


Figure 45 – Effect of preionization on the 1064 nm breakdown threshold as seen through the dependence of 1064 nm breakdown intensity versus 266 nm intensity. Results are for air and two pressures are shown. Points labeled “(a,b),” “(c,d),” and “(e,f)” correspond to the Schlieren images shown in Figure 46. See text.

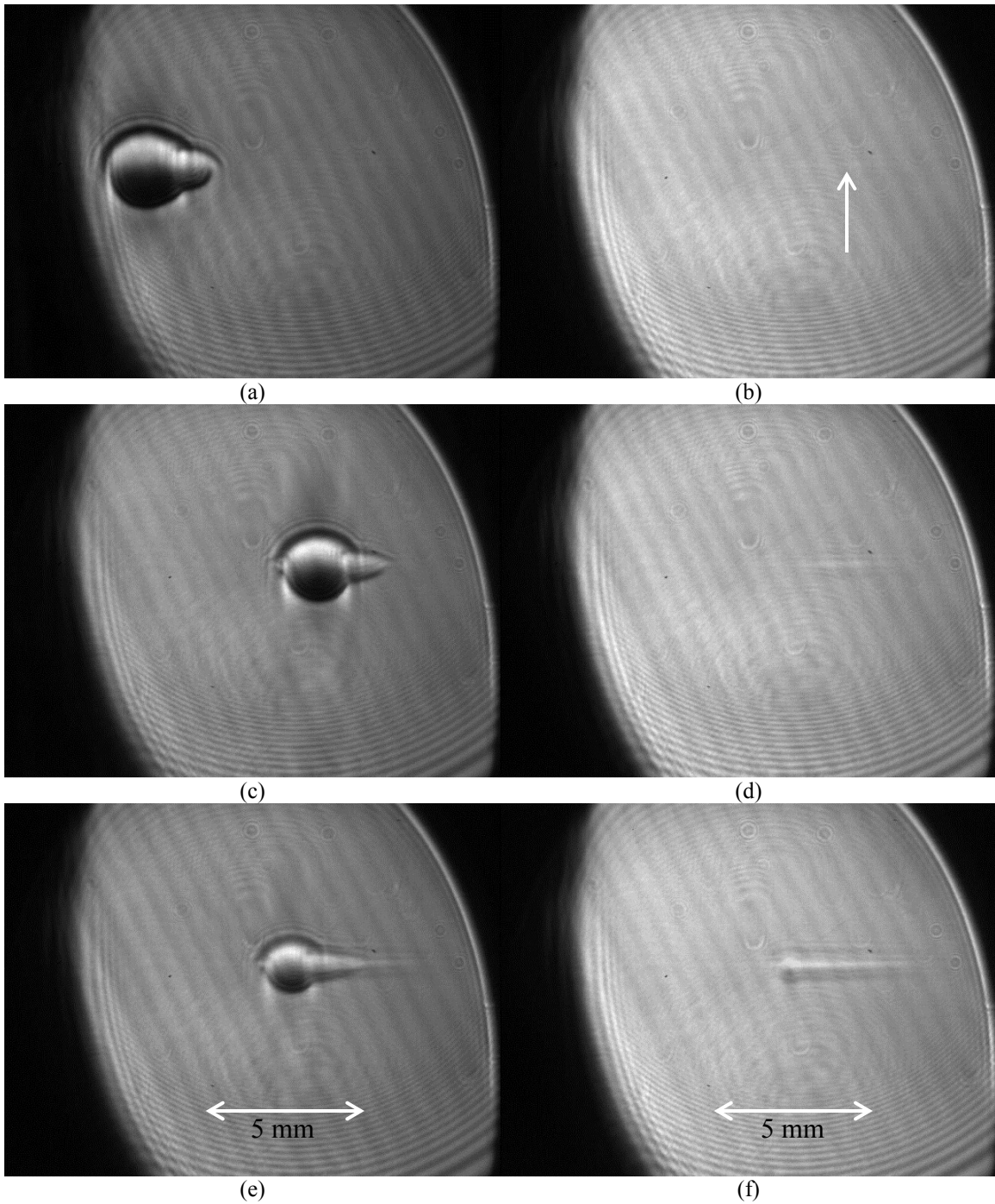


Figure 46 – Schlieren images taken at 600 torr, 1 μ s after 266 nm laser firing. Left column shows both beams overlapped while right column shows preionizing beam alone. Images correspond to data points with similar labels in Figure 45. Both the preionizing and energy addition beams enter from the left. Schlieren beam position remained fixed throughout experiment and scale applies to all images.

5 Conclusion

As natural gas engine technology continues to evolve, lean, high BMEP operation will become the standard. Such conditions strain traditional ignition systems, which at best will require frequent maintenance, and at worst will result in poor engine performance. Laser ignition is a well-studied candidate for the replacement of traditional spark plugs, although implementation in an industrial setting remains elusive. Several open path beam systems have been studied that show the potential benefits of laser ignition, although such systems have been used strictly in laboratory studies. The danger presented by high energy open path laser beams is too great for use in industry, and their long term performance remains to be studied. Hence, several alternative delivery methods have been investigated, including compact cylinder mounted laser systems, cylinder mounted gain media with fiber delivered pump light, and fiber delivery from a remote laser source. Several attempts have been made at creating cylinder mounted laser sources, and for the most part they have been successful in proving such a system is viable. However, more testing is needed to determine their usable service life, as heating, vibration, and contaminants can degrade performance over time. For large engines with many cylinders, cost could be a prohibitive factor. Placing the gain medium on the cylinder and delivering pump light from a single source by fiber optics could help to lower the cost, as diodes tend to be the most expensive component. However, the laser cavity would still be in close proximity to the hot combustion gases and stability and cooling may be problematic. Finally, fiber delivery of the laser light has been

considered, and represents a low cost option, as only a single laser system is required and can be placed away from the combustion chamber. Tests have shown sufficient laser intensity can be delivered using cyclic olefin polymer-coated silver hollow fibers, and reliable engine operation was obtained. Mechanisms for multiplexing light from one source to multiple fibers have been developed, and shown to work reliably running two cylinders with hollow core fiber delivery. Unfortunately, hollow core fibers are highly susceptible to beam quality degradation by vibration as well as bending. Such constraints limit the practicality of fiber delivery, and hence in this work, solid core fibers were considered. Previous work with solid core fibers was met with limited success, and generally the fibers were unable to carry laser pulses with sufficient beam quality and energy for spark formation and ignition. Here it was shown that by using large clad fibers and long duration laser pulses, high quality beams could be delivered to form sparks for ignition, and reliable engine operation could be achieved.

Previous work at CSU has shown high beam quality can be achieved with large core fibers if a thick cladding is used. Building off this finding, a delivery system for engine ignition was designed. To examine effects of bending, 400 μm core, 720 μm clad fibers were arranged in several different configurations and the output beam quality at 1064 nm was measured. While straight fibers produce the best quality, the degradation was not severe when bent in several different positions as compared to hollow core fibers. The beam quality was found to be related to mechanical stress in the fiber, as the best results were found when the fiber was allowed to naturally relax and relieve stress. Further investigation into this relationship would be beneficial for developing this system, perhaps by numerically modeling the effects of bending on beam quality, similar

to the analysis by Gloge [53]. Such a model would help optimize fiber positioning for beam quality and improve understanding of the effects of stress in critical locations such as at the epoxied connectors. Next, the energy handling characteristics of the fiber were studied. It was found that at 30 ns, damage occurred at 25 mJ input energy, and at 50 ns, more than 27 mJ could be sent through. Stimulated Brillouin Scattering (SBS), however, placed a practical constraint on this system, and its effects became more pronounced as the pulse duration was increased. To prevent feedback into the laser in future tests, a Faraday isolator could be employed, but for silica fiber delivery in general, SBS may impose a maximum on the energy that can be delivered. Increasing the pulse duration allows more energy to be transmitted without damage, but also increases the amount of energy reflected by SBS, decreasing the overall transmission. Further study into this area should help find ways to mitigate the effects of SBS, such as widening the spectral line width of the laser source [60], to allow more energy to be transmitted. Next, short duration tests (50 hours) with 15 mJ, 30 ns pulses were performed to ensure continued operation would not damage the fiber. Two separate 50 hour tests showed no damage, although the fiber input and laser beam became misaligned over the course of the test. Future designs would need to first determine what component moved relative to the others, and ensure that its position remains fixed for the period between maintenance intervals on the engine.

While it was shown the fiber can deliver sufficient power and beam quality to form sparks in engine conditions while stationary, any real system must operate in the presence of vibration. Shaker table testing showed vibrating a straight fiber degraded the beam quality to the point where spark formation was no longer possible. Vibration with

bending could be accomplished however by coaxing the fiber to vibrate in torsional rather than lateral modes. This greatly reduced the displacement of the fiber under vibration and hence the mechanical stress. Reliable sparking was achieved in several different configurations with 3 mm, 20 Hz vibration. On an actual engine, where much of the fibers length will be in contact with vibrating surfaces, a hybrid system would most likely have to be employed. Straight lengths of fiber could employ a damping system, while bare sections of fiber could be curved and bent to reach the cylinder. This system would need to be engine specific, as small amounts of vibration (< 1 mm) can be managed with careful fiber placement without the need for damping.

The engine used for testing in this work had very small amounts of vibration, and hence careful placement of the fiber was sufficient to maintain beam quality. A mock engine was setup in the laboratory and a frame was developed to hold the fiber in the position required by the placement of the engine and laser. By placing the fiber on the stationary frame which had no direct contact with the engine, potential effects of vibration were minimized. Reliable sparking was achieved in engine like conditions (pressures as low as 3.4 bar) on the bench top. The final step in test preparation was the design of an optical spark plug which would contain the necessary optics for spark formation as well as provide optical access to the combustion chamber. The plug designed and presented here incorporated a wide range of adjustability, including lens placement and fiber alignment, as well as visual access to the combustion chamber. As the angle at which light exits the fiber was found to be dependent on the fiber's position, this adjustability was necessary to ensure the light properly aligned with the focusing lens. In future iterations, it would be beneficial to study why the light exits at an angle

non-parallel to the fiber axis, and see if this effect can be minimized by some method. Without the need for alignment, the entire plug could be made much smaller, similar to the size of a traditional spark plug. It would also allow for plug and play operation, which would be required on a practical system.

To prove the viability of the solid core fiber ignition system, tests were performed on a single cylinder CFR engine. The fiber delivery system was able to operate the engine without misfire at several load conditions and air-fuel ratios. In addition, comparisons of performance were made with traditional electric spark ignition. Laser ignition was able to maintain similar NMEP using less intake pressure than spark ignition for a given air-fuel ratio, resulting in increased fuel efficiency. The increased efficiency is likely due to slightly reduced peak temperatures and more complete combustion resulting from laser ignition. Improvements in emissions of NO_x , CO, and THC were also observed for almost all load points, indicating cooler and more complete combustion with laser ignition. COV and lean limits were similar for both ignition systems, although direct comparison is made difficult by the under-damped nature of the PID control system. In future tests it would be beneficial to measure the air-fuel ratio before entering the combustion chamber so more precise control could be achieved. Despite having a delivered laser energy below the published 10-20 mJ required for lean ignition, successful engine operation was achieved nonetheless. This is attributed to the small focal volume in which the spark was formed and decreased flame thickness resulting from the high unburned gas temperature. Finally, in contradiction with published observations, the laser ignition system resulted in a slower early flame speed than the electric ignition system. This is likely a combination of the lower charge density required

for similar NMEP with the laser system and the low laser energy. It is expected that increased laser energy and similar intake pressures would yield an increase in the laser ignited early flame speed.

While the fiber operated reliably throughout the test, the optics within the spark plug became damaged and needed replacement within ~ 2.5 hours. Likely causes include gas leakage through the copper gaskets sealing the sapphire windows and heat effects. The intensity incident on the damaged lens was calculated to be well below its damage threshold, so further study would be required to mitigate this issue. If this issue could be solved, it would be of interest to see what would result had the test been performed with the initially planned energy levels (25 mJ, 50 ns).

Finally, initial tests were presented investigating the use of UV preionization and overlapped pulses to create a controllable ignition source. The desired result of such a scheme is to create a spatially extended source that does not cause full breakdown, but rather heats the gas. Initial results showed the addition of 1064 nm light to a UV beam results in no noticeable change in the gas or full breakdown, but nothing in between. Two experiments were conducted, one to estimate the electron number density by measuring the plasma conductivity, and one to examine the effects of UV preionization on 1064 nm breakdown. It was shown that a significant amount of preionization is created by the UV beam even without visible breakdown. This preionization has a significant effect on the 1064 nm intensity required to cause breakdown, substantially lowering the breakdown threshold. Dual pulse schemes such as this one allow considerably more variables to adjust and substantial optimization is still required. Work in the near future should include full UV breakdown conditions in the electron number

density measurement, as well as extending the presented dual pulse experiment to lower pressures (~ 10 torr). It would also be beneficial to combine the electron number density measurement with the low pressure dual pulse experiment to see if the observed drops in 1064 nm intensity correspond to a significant increase in preionization. A thorough optimization of all variables considered should include investigating the effects of time delay between the two beams, focusing conditions, pressure dependence, as well as the wavelengths of both the preionization and energy addition beams. Adding optical elements to split the two wavelengths after passing through the focal volume would also be beneficial to characterize how much energy is absorbed from each beam. Nonetheless, the results presented here show promise for future investigation of preionization controlled laser plasma formation.

REFERENCES

- [1] Ronney P. D., 1994, "Laser versus conventional ignition of flames," *Optical Engineering*, **33**(2), p. 510.
- [2] Gupta S., and Sekar R., 2009, ARES Ignition Roundtable.
- [3] Phuoc T. X., 2006, "Laser-Induced Spark Ignition Fundamental and Applications," *Optics and Lasers in Engineering*, **44**(5), pp. 351-397.
- [4] Ma J., 1998, "Laser Spark Ignition and Combustion Characteristics of Methane-Air Mixtures," *Combustion and Flame*, **112**(4), pp. 492-506.
- [5] Herdin G., Klausner J., Wintner E., Weinrotter M., Graf J., and Iskra K., 2005, "Laser Ignition: A New Concept to Use and Increase the Potentials of Gas Engines," Proceedings of ICEF2005, ASME, Ottawa, Canada.
- [6] Biruduganti M. S., Gupta S., Bihari B., Klett G., and Sekar R., 2004, "Performance Analysis of a Natural Gas Generator Using Laser Ignition," Proceedings of ICEF2004, ASME, Long Beach, CA.
- [7] Ramsden S., and Savic P., 1964, "A radiative detonation model for the development of a laser-induced spark in air," *Nature*, **203**, pp. 1217-1219.
- [8] Bach G., Knystautas R., and Lee J. H., 1969, "Direct initiation of spherical detonations in gaseous explosives," Symposium (International) on Combustion, Elsevier, pp. 853-864.
- [9] Lee J. H., and Knystautas R., 1968, Laser spark ignition of chemically reactive gases, American Institute of Aeronautics and Astronautics.
- [10] Dale J., Smy P., and Clements R., 1978, "Laser Ignited Internal Combustion Engine-an Experimental Study," SAE International, **780329**.
- [11] Beduneau J., 2003, "Measurements of minimum ignition energy in premixed laminar methane/air flow by using laser induced spark," *Combustion and Flame*, **132**(4), pp. 653-665.
- [12] Bradley D., Sheppard C. G. W., Suardjaja I. M., and Woolley R., 2004, "Fundamentals of High-Energy Spark Ignition with Lasers," *Combustion and Flame*, **138**(1-2), pp. 55-77.
- [13] Weinrotter M., Kopecek H., Tesch M., Wintner E., Lackner M., and Winter F., 2005, "Laser ignition of ultra-lean methane/hydrogen/air mixtures at high temperature and pressure," *Experimental Thermal and Fluid Science*, **29**(5), pp. 569-577.

- [14] Phuoc T. X., 2000, "Laser Spark Ignition: Experimental Determination of Laser-Induced Breakdown Thresholds of Combustion Gases," *Optics Communications*, **175**(4-6), pp. 419-423.
- [15] Phuoc T. X., and White F. P., 1999, "Laser-induced spark ignition of CH₄/air mixtures," *Combustion and Flame*, **119**(3), pp. 203-216.
- [16] Sloane T. M., 1990, "Energy requirements for spherical ignitions in methane-air mixtures at different equivalence ratios," *Combustion science and technology*, **73**, pp. 351-365.
- [17] Weinrotter M., Ast G., Kopecek H., and Wintner E., 2005, "An Extensive Comparison of Laser-Induced Plasma Ignition and Conventional Spark Plug Ignition of Lean Methane-Air Mixtures under Engine-Like Conditions," SAE International.
- [18] Bihari B., Gupta S., Sekar R., Gingrich J., and Smith J., 2005, "Development of Advanced Laser Ignition System for Stationary Natural Gas Reciprocating Engines," Proceedings of ICEF2005, ASME, Ottawa, Canada.
- [19] Joshi S., Olsen D. B., Dumitrescu C., Puzinauskas P. V., and Yalin A. P., 2009, "Laser-Induced Breakdown Spectroscopy for In-Cylinder Equivalence Ratio Measurements in Laser-Ignited Natural Gas Engines.," *Applied spectroscopy*, **63**(5), pp. 549-54.
- [20] Yalin A. P., Defoort M., Joshi S., Olsen D. B., and Willson B., 2005, "Laser Ignition of Natural Gas Engines Using Fiber Delivery," Proceedings of ICEF2005, ASME, Ottawa, Canada.
- [21] Adams S. F., Miles J. A., and Laber A. C., 2010, "Resonant Laser Induced Breakdown for Fuel-Air Ignition," AIAA, (January), pp. 1-5.
- [22] Sircar A., Dwivedi R. K., and Thareja R. K., 1996, "Laser Induced Breakdown of Ar, N₂ and O₂ Gases Using 1.064, 0.532, 0.355 and 0.266 μ m Radiation," *Applied Physics B*, **63**(6), pp. 623-627.
- [23] Turcu I. C. E., Gower M. C., and Huntington P., 1997, "Measurement of KrF laser breakdown threshold in gases," *Optics Communications*, **134**(January), pp. 66-68.
- [24] Chylek P., Jarzembski M. a, Srivastava V., and Pinnick R. G., 1990, "Pressure dependence of the laser-induced breakdown thresholds of gases and droplets.," *Applied optics*, **29**(15), pp. 2303-6.
- [25] Tauer J., Kofler H., and Wintner E., 2010, "Laser-Initiated Ignition," *Laser & Photonics Reviews*, **4**(1), pp. 99-122.
- [26] Morgan C., 1975, "Laser-induced breakdown of gases," *Reports on Progress in Physics*, **621**.

- [27] Kopecek H., 2003, "Laser ignition of methane-air mixtures at high pressures," *Experimental Thermal and Fluid Science*, **27**(4), pp. 499-503.
- [28] Syage J. A., Fournier E. W., Rianda R., and Cohen R. B., 1988, "Dynamics of flame propagation using laser-induced spark initiation: Ignition energy measurements," *Journal of Applied Physics*, **64**(3), p. 1499.
- [29] Edmonson R. B., Olsen H. L., and Gayhart E. L., 1954, "Application of Ideal Gas Theory to the Gaseous Expansion from an Electric Spark," *Journal of Applied Physics*, **25**(8), p. 1008.
- [30] Phuoc T. X., and White F. P., 2002, "An optical and spectroscopic study of laser-induced sparks to determine available ignition energy," *Proceedings of the Combustion Institute*, **29**(2), pp. 1621-1628.
- [31] Herdin G., Klausner J., Weinrotter M., Graf J., and Wimmer A., 2006, "GE Jenbacher's Update On Laser Ignited Engines," *Proceedings of ICEF2006*, ASME, Sacramento, CA.
- [32] Ahrens D. L., Yalin A. P., Olsen D. B., and Kim G.-H., 2005, "Development of an Open Path Laser Ignition System for a Large Bore Natural Gas Engine: Part 1 — System Design," *Proceedings of ICES2005*, ASME, Chicago, IL, pp. 489-498.
- [33] Loccisano F., 2011, "Investigation of optical prechamber spark plug and dual laser pulses for ignition," *Masters Thesis*, Colorado State University.
- [34] Phuoc T. X., 2000, "Single-Point Versus Multi-Point Laser Ignition: Experimental Measurements of Combustion Times and Pressures," *Combustion and Flame*, **510**, pp. 508-510.
- [35] Ahrens D. L., Olsen D. B., and Yalin A. P., 2005, "Development of an Open Path Laser Ignition System for a Large Bore Natural Gas Engine: Part 2 — Single Cylinder Demonstration," *Proceedings of ICES2005*, ASME, Ottawa, Canada, pp. 505-513.
- [36] Kroupa G., Franz G., and Winkelhofer E., 2009, "Novel Miniaturized High-Energy Nd-YAG Laser for Spark Ignition in Internal Combustion Engines," *Optical Engineering*, **48**(1).
- [37] Inohara T., Ando A., and Kido N., 2009, "Laser Ignition System."
- [38] Kofler H., Tauer J., Tartar G., Iskra K., Klausner J., Herdin G., and Wintner E., 2007, "An Innovative Solid-State Laser for Engine Ignition," *Laser Physics Letters*, **4**(4), pp. 322-327.
- [39] Zhan Y., Yang Q., Wu H., Lei J., and Liang P., 2009, "Degradation of beam quality and depolarization of the laser beam in a step-index multimode optical

- fiber,” *Optik - International Journal for Light and Electron Optics*, **120**(12), pp. 585-590.
- [40] Grimes G. J., Serafino A. J., and Coyle R. J., 1999, “Propagation effects of long step-index fibers for high-power beam delivery,” *Proceedings of SPIE*, San Jose, CA, p. 24.
- [41] Hurand S., Chauny L.-A., El-Rabii H., Joshi S., and Yalin A. P., 2011, “Mode Coupling and Output Beam Quality of 100-400 μm Core Silica Fibers.,” *Applied optics*, **50**(4), pp. 492-9.
- [42] Joshi S., Yalin A. P., and Galvanauskas A., 2007, “Use of Hollow Core Fibers, Fiber Lasers, and Photonic Crystal Fibers for Spark Delivery and Laser Ignition in Gases.,” *Applied optics*, **46**(19), pp. 4057-64.
- [43] Su D., Boechat a a, and Jones J. D., 1992, “Beam delivery by large-core fibers: effect of launching conditions on near-field output profile.,” *Applied optics*, **31**(27), pp. 5816-21.
- [44] Yalin A. P., Joshi S., DeFoort M., and Willson B., 2008, “Towards Multiplexed Fiber Delivered Laser Ignition for Natural Gas Engines,” *Journal of Engineering for Gas Turbines and Power*, **130**(4), p. 044502.
- [45] Reynolds A., 2011, “Development and Testing of a Multiplexing System for Laser Ignition of Large Bore Natural Gas Engines,” *Masters Thesis*, Colorado State University.
- [46] Stakhiv A., Kopecek H., Zheltikov A. M., and Wintner E., 2004, “Laser Ignition of Engines Via Optical Fibers?,” *Laser physics*, **14**(5), pp. 738–747.
- [47] Yalin A. P., DeFoort M., Willson B., Matsuura Y., and Miyagi M., 2005, “Use of Hollow-Core Fibers to Deliver Nanosecond Nd:YAG Laser Pulses to Form Sparks in Gases.,” *Optics letters*, **30**(16), pp. 2083-5.
- [48] Mann G., Jurke M., Zoheidi M., Eberstein M., and Kruger J., 2010, “Influence of core diameter and coating material on nanosecond laser-induced damage threshold of optical multimode fibers,” *Journal of Optoelectronics and Advanced Materials*, **12**(3), pp. 711-714.
- [49] El-Rabii H., and Gaborel G., 2007, “Laser Ignition of Flammable Mixtures Via a Solid Core Optical Fiber,” *Applied Physics B*, **87**(1), pp. 139-144.
- [50] Mullett J. D., Dearden G., Dodd R., Shenton A. T., Triantos G., and Watkins K. G., 2009, “A Comparative Study of Optical Fibre Types for Application in a Laser-Induced Ignition System,” *Journal of Optics A: Pure and Applied Optics*, **11**(5).

- [51] Cheng M.-Y., Chang Y.-C., Galvanauskas A., Mamidipudi P., Changkakoti R., and Gatchell P., 2005, "High-energy and high-peak-power nanosecond pulse generation with beam quality control in 200-micron core highly multimode Yb-doped fiber amplifiers.," *Optics letters*, **30**(4), pp. 358-60.
- [52] Gloge D., 1972, "Optical Power Flow in Multimode Fibers," *Bell Syst. Tech. J.*, **51**(8), pp. 1767–1783.
- [53] Gloge D., 1975, "Optical-fiber packaging and its influence on fiber straightness and loss," *Bell System Technical Journal*, **54**(2), pp. 245–62.
- [54] Peterman D., 2005, "The Misunderstood M2," *SPIE's oemagazine*, (August), p. 30.
- [55] Paschotta R., 2011, "M2 Factor," *Encyclopedia of Laser Physics and Technology*.
- [56] Siegman A., 1998, "How to (maybe) measure laser beam quality," *Diode Pumped Solid State Lasers: Applications*, (October 1997), pp. 1-18.
- [57] Boechat A. A., Su D., Hall D. R., and Jones J. D., 1991, "Bend loss in large core multimode optical fiber beam delivery systems.," *Applied optics*, **30**(3), pp. 321-7.
- [58] Marcuse D., and Presby H., 1975, "Mode coupling in an optical fiber with core distortion," *Bell Sys. Tech. J.*, **1**(3).
- [59] Joshi S., Franka I., Loccisano F., and Yalin A. P., "Delivery of Nanosecond Nd:YAG Laser Pulses to Form Sparks in Gases with Step-Index Silica Fibers," On Submission to *IEEE Photonics Letters*.
- [60] Kobayakov A., Sauer M., and Chowdhury D., 2009, "Stimulated Brillouin scattering in optical fibers," *Advances in Optics and Photonics*, **2**(1), p. 1.
- [61] Paschotta R., 2011, "Brillouin Scattering," *Encyclopedia of Laser Physics and Technology*.
- [62] Sjöberg M., Quiroga-Teixeiro M. L., Galt S., and Hård S., 2003, "Dependence of stimulated Brillouin scattering in multimode fibers on beam quality, pulse duration, and coherence length," *JOSA B*, **20**(3), pp. 434–442.
- [63] Joshi S., Loccisano F., Yalin A. P., and Montgomery D. T., 2011, "On Comparative Performance Testing of Prechamber and Open Chamber Laser Ignition," *Journal of Engineering for Gas Turbines and Power*, **133**(12), pp. 122801-1-5.
- [64] Smith A. V., and Do B. T., 2008, "Bulk and surface laser damage of silica by picosecond and nanosecond pulses at 1064 nm.," *Applied optics*, **47**(26), pp. 4812-32.

- [65] "SF11 Plano-Convex Lenses," Melles Griot Catalog.
- [66] 2003, "Using GRADIUM® glass lenses in High Power Lasers: Tips and Tricks," Lightpath Technologies, pp. 1-12.
- [67] Turns S. R., 2000, *An Introduction to Combustion: Concepts and Applications*, McGraw-Hill.
- [68] Ferguson C. R., and Kirkpatrick A. T., 2000, *Internal Combustion Engines: Applied Thermosciences*, John Wiley & Sons.
- [69] Yalin A., Loccisano F., Joshi S., Zhang Z., and Shneider M., 2010, "Pre-Ionization Controlled Laser Plasma Formation for Ignition Applications," AIAA-2010-4307, Chicago, IL, pp. 1-18.
- [70] Shneider M. N., Zheltikov A. M., and Miles R. B., 2011, "Tailoring the air plasma with a double laser pulse," *Physics of Plasmas*, **18**(6), p. 063509.
- [71] Tropina A., and Michael J., 2011, "Ignition Delay Time and Laminar Flame Velocity for a Combined Laser – Microwave Ignition," *Plasma Science, IEEE*, **39**(12), pp. 3263-3268.
- [72] Michael J. B., Dogariu a., Shneider M. N., and Miles R. B., 2010, "Subcritical microwave coupling to femtosecond and picosecond laser ionization for localized, multipoint ignition of methane/air mixtures," *Journal of Applied Physics*, **108**(9), p. 093308.
- [73] Michael J. B., 2012, "Localized microwave pulsed plasmas for ignition and flame front enhancement," PHD Dissertation, Princeton University.
- [74] Zvorykin V. D., Levchenko a. O., Molchanov a. G., Smetanin I. V., and Ustinovskii N. N., 2010, "Microwave energy channeling in plasma waveguides created by a high-power UV laser in the atmosphere," *Bulletin of the Lebedev Physics Institute*, **37**(2), pp. 60-64.
- [75] Zvorykin V., and Levchenko A., 2011, "Control of extended high-voltage electric discharges in atmospheric air by UV KrF-laser radiation," *Quantum Electronics*, **41**(3), pp. 227-233.
- [76] Way J., Hummelt J., and Scharer J., 2009, "Experimental measurements of multiphoton enhanced air breakdown by a subthreshold intensity excimer laser," *Journal of Applied Physics*, **106**(8), p. 083303.
- [77] Gamal Y., 1988, "The breakdown of molecular oxygen by brief pulses of laser radiation," *Journal of Physics D: Applied Physics*, **21**(January), pp. 1117-1120.

- [78] Dewhurst R., 1978, "Comparative data on molecular gas breakdown thresholds in high laser-radiation fields," *Journal of Physics D: Applied Physics*, **11**, pp. 191-195.
- [79] Zvorykin V. D., Levchenko a. O., Shutov a. V., Solomina E. V., Ustinovskii N. N., and Smetanin I. V., 2012, "Long-distance directed transfer of microwaves in tubular sliding-mode plasma waveguides produced by KrF laser in atmospheric air," *Physics of Plasmas*, **19**(3), p. 033509.

APPENDIX 1 – VIBRATION DAMPING WITH OIL

In order to test the fibers ability to create sparks in a vibrating environment, high power tests were conducted, starting with the oil bath shown in Figure 13, Section 2.3.1. The output optics were similar to those in Joshi et al. [59], who used a lens to collimate the output beam and a 10 mm focal length Gradium lens to tightly focus it. While Joshi et al. were able to form sparks in air, the M^2 of the connectorized fiber used here is much worse (4.5 compared with 2.5), and will not allow for the focal spot size of 8 μm as reported previously. Scaling the value given the current achievable M^2 results in a spot size of 14.4 μm , which would require 6.4 mJ, 9.5 ns pulses to reach the reported 420 GW/cm^2 breakdown threshold. Even more energy would be required at the input due to transmission losses, and would be above the range where damage to the fiber was reported. Therefore, the test would have to be done at higher pressures. The output optics are shown attached to the shaker table in Figure 47. The fiber connects to an adjustable mount on a cage system that contains the attachment to the shaker table, the collimating lens, and the pressure chamber. The Gradium lens doubled as a window to the pressure chamber, which was pressurized using bottled nitrogen. Alignment was maintained by locking all components to the cage system, which was assumed rigid.

This experiment used the same Continuum laser as previously mentioned to provide high energy pulses about 50 ns in length. Unfortunately, this test was carried out before the effects of SBS (see Section 2.2.2) were studied, and much of the difficulty encountered can be attributed to this. Reliable sparking in the oil bath was never achieved below 13.6 bar (200 psig). Given the beam quality of the fiber resting in the

trough ($M^2 \approx 6$), the smallest focal spot size achievable was $\approx 19 \mu\text{m}$. Scaling the breakdown threshold from 420 GW/cm^2 at atmospheric pressure using Equation (1) and $n = 0.5$ to 6.8 bar (100 psig), the threshold becomes $\approx 105 \text{ GW/cm}^2$. To hit this threshold with the given spot size and 50 ns pulses, approximately 15 mJ would be required. Given the loss associated with the output optics and fiber transmission loss (see Figure 9a Section 2.2.2), this translates to an input energy of about 20 mJ . With the power handling characteristics of these fibers not yet studied at the time of this test, a safe limit of 15 mJ was established, and hence reliable sparking was not achieved. The concept of viscous damping was not disproven, however, and a new system was designed to allow the fiber to rest in a less stressful position.

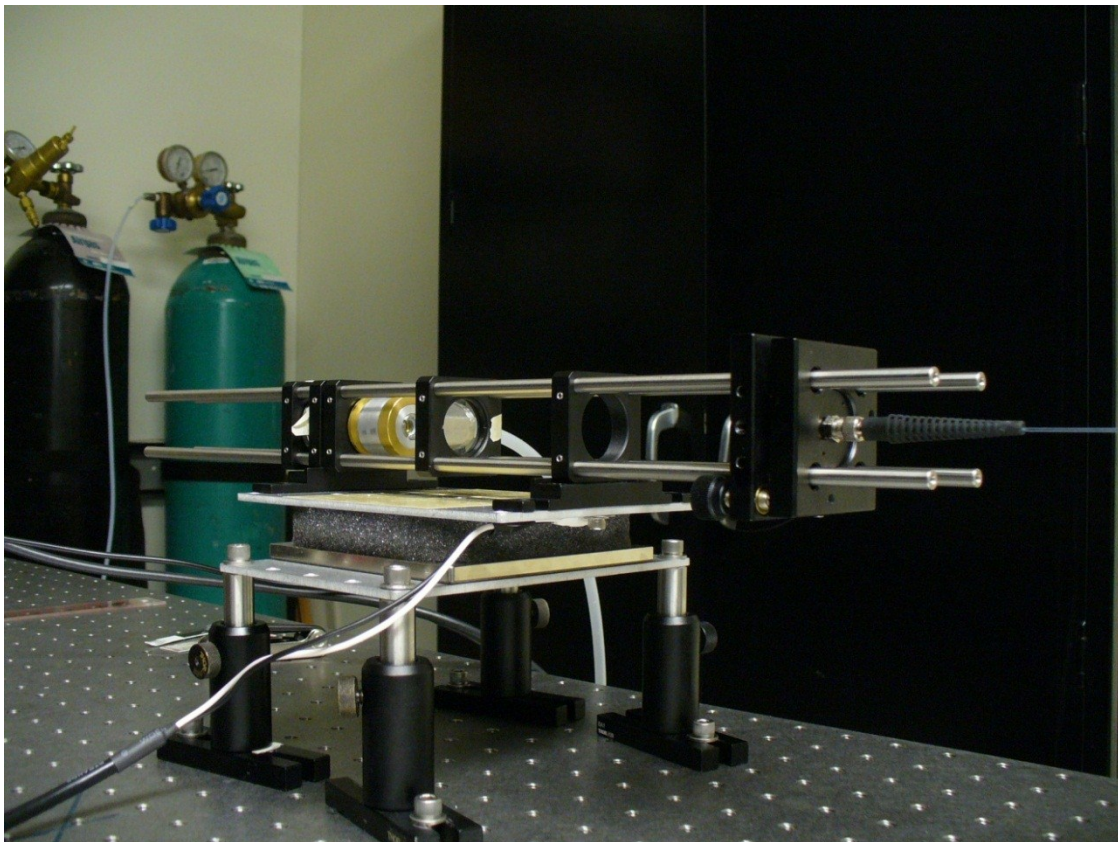


Figure 47 – Shaker table with output optics required for spark formation.

The new design incorporated a tube to hold the damping oil. This has several advantages, including being fully sealed, flexible, and can provide protection from harsh engine environments. It also eliminates the need for the fiber to sag in the middle to be fully immersed in the oil. A CAD model is shown in Figure 48 of one end of the system. The fiber (yellow) is epoxied in a small plastic insert (gray), which is placed in the fiber connector (red). The insert allows easy replacement if the fiber becomes damaged. Once a connector has been attached to both sides, the entire fiber can be slid through the tube (green), and the tube can be filled with oil. The oil is held in the tube with the seal insert (blue), which seals to the fiber connector with an o-ring and the outer tube with a hose clamp. The seal insert is bolted to the fiber connector and allows the end to be mounted to a standard lens mount. The tube OD is 1" which allows ease of use in a laboratory setting.

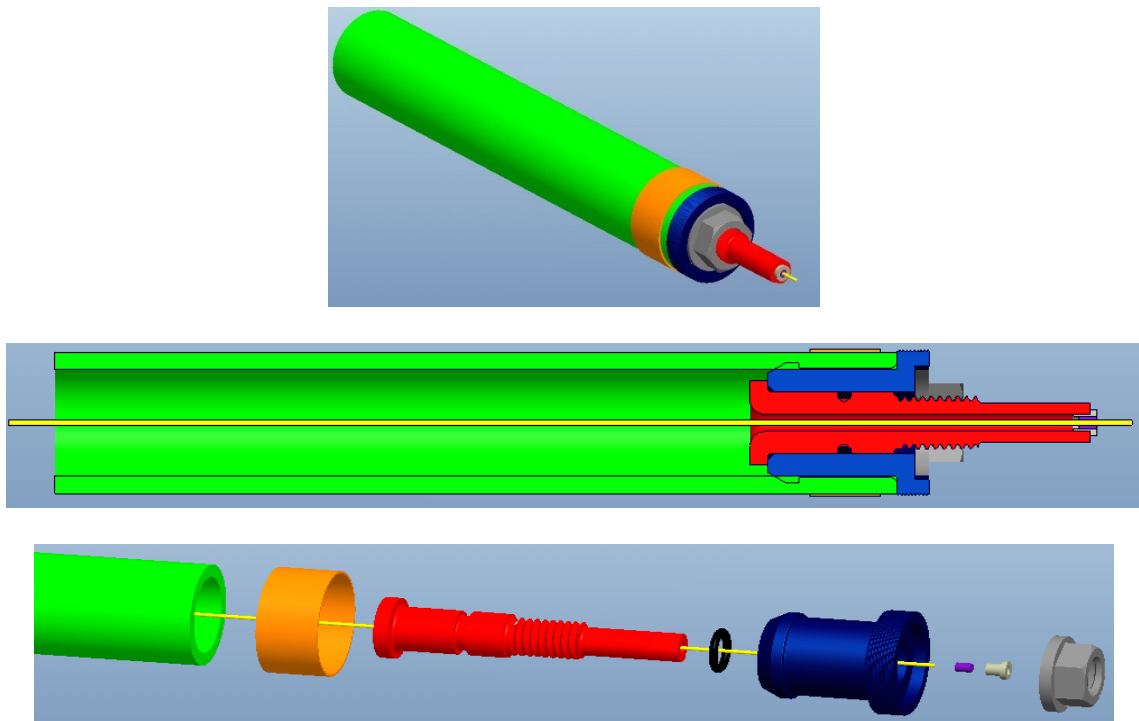


Figure 48 – CAD model of laboratory prototype for fiber vibration damping. Full (top), cutaway (middle), and exploded (bottom) views.

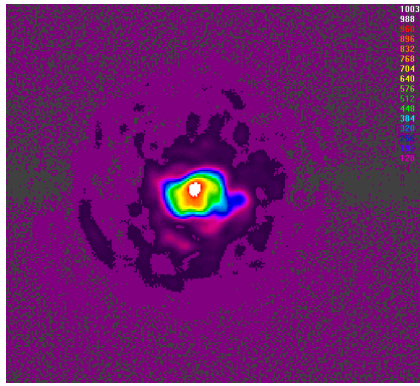
Testing of the system was performed using a different Nd:YAG laser (NewWave, $M^2 = 1.9$) with 15 ns pulse duration. Input conditions were the same as all previous tests. With the laser nominally firing at 10 Hz, the shaker table was set to a frequency of 20 Hz to mimic the timing on a real engine (1200 rpm). Initially, the fiber and tube were held straight; output M^2 (NA method) and energy required for 100% spark rate at 6.8 bar (100 psi) were measured for vibration amplitudes of 1, 3, and 5 mm. Results are summarized in Table 7. The beam quality shows significant improvement in comparison with the oil bath test. Of particular interest is the stationary beam quality. Previously it was shown that the output beam quality increases to $M^2 \approx 4.4$ for a straight fiber with a single connector. In this case, two connectors have been added and still the beam quality improves (see Figure 49). Using only the two custom connectors and placing the fiber flat without the tube or oil results in a more familiar $M^2 \approx 4.7$, indicating the oil immersion is relieving stress in the fiber. While vibrating, the output beam M^2 increases by 50% in the 3 mm case, more than with the oil bath, but the overall value is significantly lower. Note that maximum values are presented, and the beam quality throughout most of the motion is better than shown here. At 5 mm amplitude, the beam quality remained sufficient for sparking in 6.8 bar (100 psi), but 100 % sparking was not observed throughout the entire motion. While reliable sparking was present near the vibration equilibrium position, the sparking cut out near the ends of the shaker table's stroke. By placing a piece of burn paper over the focusing lens, the position of the most intense portion of the beam with respect to the lens could be measured. It was found that at 5 mm amplitude, this position moved relative to the lens by about 4.5 mm. In order to tightly focus, precise alignment on the focus lens is required, and at such high vibration

amplitudes this alignment was lost near the extremes of motion. Additional investigation found the output optics were not moving with respect to the fiber tip, indicating the direction of light exiting the fiber is influenced by the fiber's movement. This implies a limit exists on the amplitude of vibration such a system can handle.

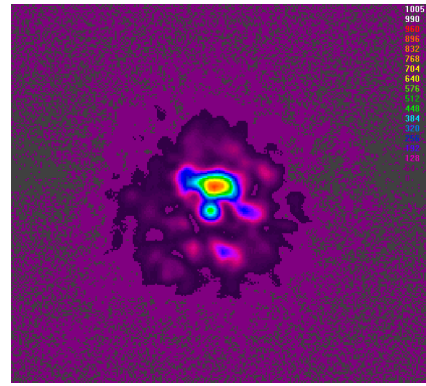
The next step was to bend the fiber and tube to a 90 degree angle and attempt to repeat the test. Unfortunately, this did not yield viable results. Bending the tube, even at small angles (10 degrees) resulted in a dramatic increase in M^2 . At a full 90 degrees, the output M^2 was ≈ 11.4 . Adjusting the relative length of the tube and fiber by moving the seal in and out did not change the beam quality. It is thought that because the tube is much heavier and stiffer than the fiber, the shape of the bend is determined by the tube. As pointed out earlier, the fiber performs best when allowed to find its own position to minimize stress. The tube prevents this from happening. While many important results were found from this study, it cannot be used on a practical system if bending is not allowed. Therefore, other methods were investigated that would allow bending.

Table 7 - Fiber performance at various vibration amplitudes. Max Output M^2 corresponds to the maximum measured value along the entire path of motion. Energy Input is the amount of input energy required for 100% spark rate at the given amplitude. *100% sparking was only obtained when output beam maintained alignment with focus lens. See text.

Amplitude (mm)	Max Output M^2	Energy Input (mJ)
0 (Stationary)	3.0	2.6
1	3.9	3.0
3	4.6	3.2
5	5.2	5.0*



(a)



(b)

Figure 49 – Beam profiles for the fiber connectorized at both ends for (a) immersed in oil ($M^2 = 3.0$) and (b) straight with no oil ($M^2 = 4.7$).

APPENDIX 2 – ADDITIONAL ENGINE TEST PLOTS

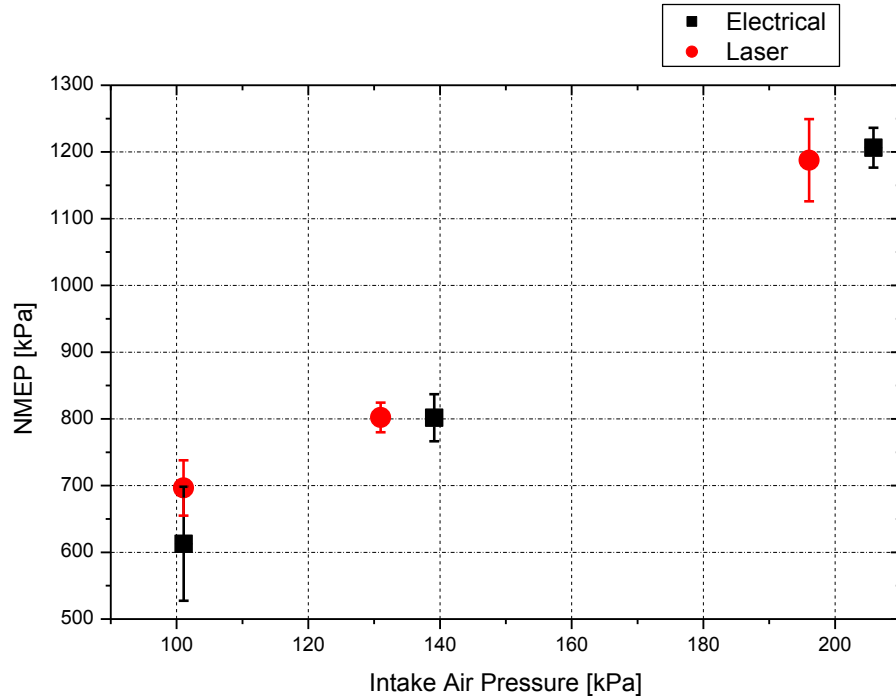


Figure 50 – NMEP vs. intake air pressure. The air-fuel ratio for NMEP of 6, 8, and 12 bar are 20, 26, and 32, respectively for both ignition systems.

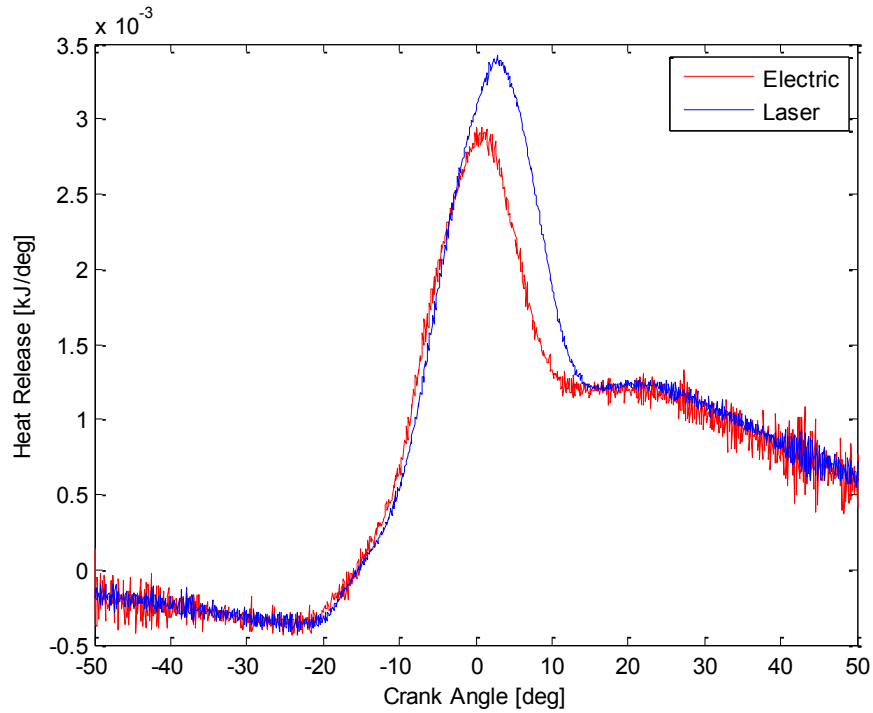


Figure 51 – Heat Release vs. Crank Angle for NMEP 6 bar, air-fuel 20. (NMEP of laser system in this case is actually 6.9 bar, while electric system is at 6 bar.)

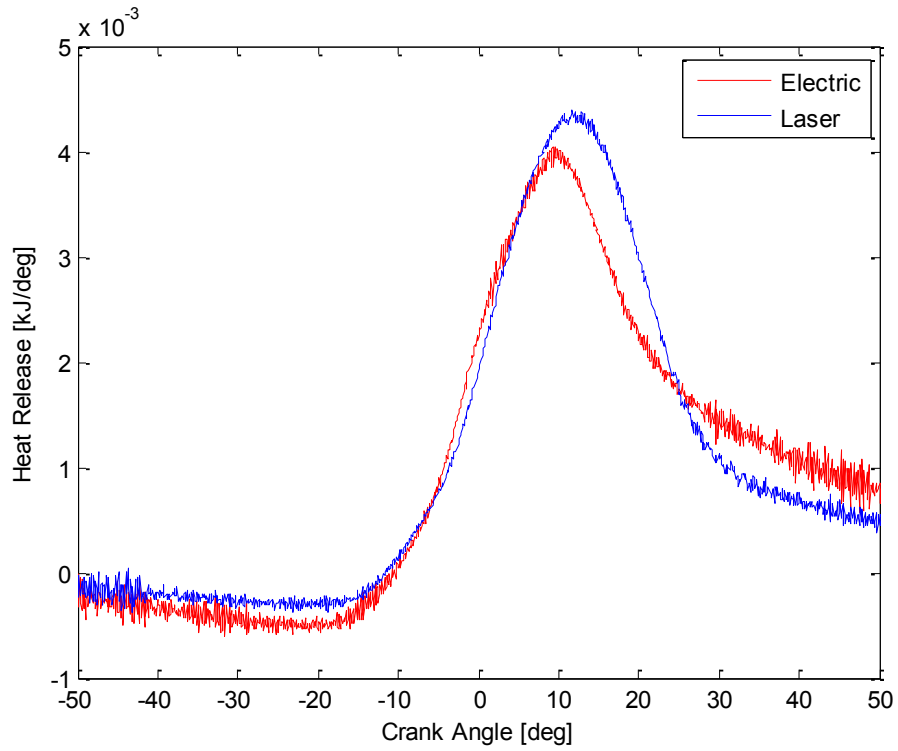


Figure 52 – Heat Release vs. Crank Angle for 8 bar NMEP, air-fuel 26.

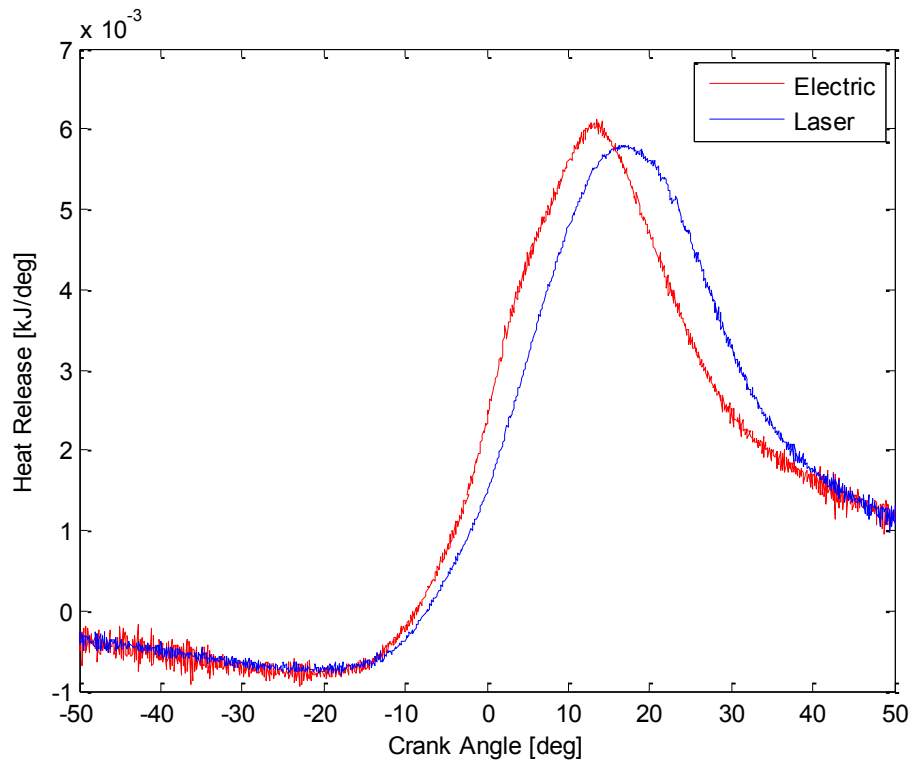


Figure 53 – Heat Release vs. Crank Angle for 12 bar NMEP, air-fuel 32.